Towed-Array Calibration

Malcolm John Goris
BE (Elec) Hons I

A thesis submitted for the degree of
Doctor of Philosophy of
The Australian National University

December 1995

Preface

I am sincerely grateful to all those who provided valuable assistance and support throughout my PhD; in particular, to Dr. Donald McLean and Dr. Iven Mareels for their support, guidance and helpful discussions and to Mr. Ralph Marson, Dr. René Grognard and Prof. Doug Gray for their helpful discussions.

I acknowledge the Australian Commonwealth Government for funding the activities of the Cooperative Research Centre for Robust and Adaptive Systems under the Cooperative Research Centres program. For providing the financial assistance to pursue PhD studies I thank the Australian Commonwealth Government and the Cooperative Research Centre for Robust and Adaptive Systems. I appreciate the CSIRO Division of Radiophysics for their encouragement to take up postgraduate studies.

Above all, I thank my wife Kathleen for her love and encouragement.

Statement of Originality

This thesis describes work carried out between 1992 and 1995 under the guidance of Dr. Donald McLean of the CSIRO Division of Radiophysics and Dr. Iven Mareels of the Australian National University. Except where acknowledged, the work presented in this thesis is my own.

Malcolm J. Goris

December 18, 1995

Publications

Part of the work done for this thesis has been published as listed below.

Journal Papers

[J1] M. J. Goris and D. J. McLean, "Towed Array-Shape Estimation — Least Square Error Method", *submitted to IEEE J. Ocean. Eng.*, 1995

[J2] M. J. Goris, D. J. McLean and I. Y. Mareels, "Array-Shape Estimation Using Signal Information", *submitted to IEEE Trans. Information Theory*, 1995

[J3] M. J. Goris, D. J. McLean and I. Y. Mareels, "Sharpness as a Method of Towed Array-Shape Estimation", *submitted to IEEE Trans. Signal Processing*, 1995

[J4] M. J. Goris and D. A. Gray, "Reducing the Computational Load of a Kalman Filter when there are more Measurements than States", *submitted to Int. J. Systems Science*, 1995

Conference Papers

[C1] M. J. Goris and D. J. McLean, "Calibrating a Towed Array Using Redundant Information from an Impinging Broadband Signal", *Int. Conf. on Sig. Proc. and Applic. Tech.*, 1995

[C2] D. A. Gray and M. J. Goris, "A Kalman Filter Based Data Fusion Approach for Estimating the Shape of a Towed Sonar Array", *Int. Conf. on Neural Networks and Sig. Proc.*, 1995

Technical Reports

[T1] M. J. Goris and D. J. McLean, "Towed Array-Shape Estimation — A Comparison of Methods", 1995

[T2] M. J. Goris and D. A. Gray, "Estimating the Shape of a Towed Array by Kalman Filtering Both Acoustic and Compass Data", 1995

Abstract

Array processing techniques, such as beamforming, require accurate knowledge of the positions of the array's sensors. If the array's shape is not known accurately enough the array processor will be unable to estimate the signal parameters it was designed to. Towed arrays have omnidirectional sensors called hydrophones that are built into a thin flexible cylinder. The cylinder, drawn behind a towing vessel, is often assumed to have a linear shape. This assumption may not be true due to maneuvering of the tow vessel, ocean currents and hydrodynamic effects. To maintain the processor's performance under these conditions the array must be calibrated by regularly estimating its shape.

In this thesis I investigate methods of towed-array calibration. The investigation includes a theoretical derivation of the necessary conditions for array calibration using signals, development of algorithms and a comparison of algorithms from the literature.

I show the conditions necessary to determine the array and signal parameters using information only from impinging signals. This is a fundamental question of invertibility and applies to any type of array. I relate these results to the more specific problem of towed arrays which have additional geometric constraints on their shape.

I describe three new algorithms for estimating the shape of towed arrays. Two of the algorithms use signal information only. The third algorithm uses a state-space representation of the array that combines signal and heading-sensor information, and uses a model of the dynamics of towed, flexible cylinders.

I compare the accuracies of a selection of array calibrators from the literature. I explain assumptions, both explicit and implicit, made for each algorithm and, through computer simulations, determine how robust the algorithms are to variations in signal-source distribution and signal-to-noise ratio. The results of the simulations are used to investigate the sensitivities of the algorithms to the underlying assumptions. I analyse one of the algorithms, which is called sharpness, in greater detail and resolve conflicting reports on its effectiveness. Based on the analysis I give an improved, more robust sharpness function for towed arrays.

Contents

List of Figures

List of Tables

Glossary

List of Symbols and Functions

$\langle \ldots \rangle$	time average
$\mathbf{A}$	matrix of phase changes, a_{mn}
$\mathbf{a}_n$	vector of phase changes, a_{mn}, for the n^{th} signal; steering vector
a_{mn}	phase change of the n^{th} signal at the m^{th} hydrophone
BW	bandwidth
c_s	speed of sound in water
d_m	distance from the m^{th} hydrophone to the first in the line of sight to the calibrating signal
d_{mn}	distance from the m^{th} hydrophone to the first in the line of sight to the n^{th} signal
δ_n	direction cosine vector of the n^{th} signal
$\delta_{\phi,\theta}$	direction cosine vector for the look direction ϕ, θ
f_0	centre frequency of a signal
H	Hermitian transpose
λ	wavelength
M	number of hydrophones
N	number of impinging signals
P_b	beamformer power
ϕ_n	azimuth direction of arrival of the n^{th} signal
$\mathbf{R}$	array-covariance matrix
$\mathbf{R}_n$	noise-covariance matrix
$\mathbf{R}_s$	signal-covariance matrix
ρ	distance between hydrophones
r_{jk}	correlation between the j^{th} and k^{th} sensors
$r(\chi)$	spatial correlation function
$s_n(t)$	n^{th} analytic signal as a function of time
$\mathbf{s}(t)$	vector of all impinging signals as a function of time
t	time
T	matrix transpose
θ_n	elevation direction of arrival of the n^{th} signal
t_{mn}	time of arrival of the n^{th} signal at the m^{th} hydrophone relative to the first
$v_m(t)$	analytic noise at the m^{th} hydrophone as a function of time

$\mathbf{v}(t)$	vector of all noise as a function of time
χ_m	position of the m^{th} hydrophone
x_m	position of the m^{th} hydrophone in the x-direction
y_m	position of the m^{th} hydrophone in the y-direction
z_m	position of the m^{th} hydrophone in the z-direction
$z_m(t)$	analytic signal at the m^{th} hydrophone as a function of time
$\mathbf{z}(t)$	vector of all hydrophone signals as a function of time

List of Acronyms

2D	two dimensional
3D	three dimensional
DOA	direction of arrival
LSE	least-squares error
ML	maximum likelihood
MSE	mean-square error
PDSS	phase difference self survey
RMS	root mean square
SNR	signal-to-noise ratio
TDOA	time delay of arrival
TPI	tow-point induced (motion)

Chapter 1 Introduction

Towed arrays have omnidirectional, underwater, acoustic sensors called **hydrophones** that are built into a thin, flexible cylinder. The cylinder is drawn behind a towing vessel, such as a ship or submarine. Towed arrays are used in seismology for mineral exploration and in passive sonar surveillance where it is desirable to detect another vessel without revealing the tow-vessel's own location. Array processors combine the signals from the hydrophones to estimate signal parameters such as **direction of arrival** (DOA), power, spectrum and range to the source. For a correctly calibrated array, the signal-to-noise ratio (SNR) improvement of the array over one of its sensors is proportional to the number of sensors in the array and the resolution and range-estimation accuracy improves with the length of the array. And so, because of the need for increased resolution and SNR, users demand longer arrays with more hydrophones. Towed arrays are now of the order of one kilometre in length.

Towed arrays are often assumed to be linear when the tow vessel travels in a straight line. However, this assumption may not always be true due to ocean currents and hydrodynamic effects. A linear array is able to resolve the DOA angle relative to itself but an ambiguity exists as to where on the cone defined by that angle the signal source really is. If the signal source is assumed to lie on a plane the ambiguity becomes whether the signal source is on the left or the right side. This ambiguity is resolved by turning the tow vessel and noting in which direction the signal source has moved. During the turn the array will have a bend in it. At typical tow speeds of around 5 knots up to six minutes (for a one kilometre array) can elapse before the array regains its nominal, linear shape.

Array processing techniques require accurate knowledge of the positions of the array sensors [Car79, Has84, Nie91]. Without sufficiently accurate sensor-position knowledge an array processor will be unable to estimate the signal parameters it was designed to. The sensitivity of an array processor to incorrect knowledge of the sensor locations depends on the complexity of the processor. For example, high resolution, eigenvector-based direction-of-arrival estimators [JD82, Pil89], range estimators [Hin79, Has84], and adaptive noise cancellers [Ows84b] are very sensitive to imperfect sensor-location knowledge.

Ocean currents, hydrodynamic effects and tow-vessel maneuvering cause the assumption of array linearity to be invalid and will reduce the performance of array processing even to the point where no information about the impinging signals can be obtained. To retain the full

performance of the array processor and to allow processing to continue during a maneuver the locations of the hydrophones need to be estimated each time the array is to be processed. This is commonly called **array calibration** or **array straightening**. The term "array calibration" generally implies knowing the array's shape, gain characteristics of the hydrophones and amplifiers and properties of the propagating medium. In this thesis it is assumed that the gain characteristics of the sensors are known and that the propagating medium is uniform and lossless. And so, to calibrate a towed array we need estimate only its shape. Care needs to be taken when reading the literature on array calibration. For certain arrays it is implicit in the problem definition that the array shape is known accurately and calibration means knowing only the channel gains. Radio astronomy arrays are one example; the sensors are directional (unlike hydrophones which are omni-directional) and atmospheric disturbances cause unknown channel-related gains that are assumed to be independent of the signal-source distribution. This definition of calibration is not applicable to towed arrays.

One approach to towed-array calibration is to instrument the array with a number of heading and depth sensors. For mechanical and economical reasons the numbers of heading and depth sensors are often small which are not enough to infer the location of every hydrophone directly. Instead, the heading and depth sensors are used to estimate the coefficients of a low-order polynomial approximation of the array shape [Ows81, Ows84a]. The advantages of heading and depth sensors are that they provide shape information independently of external factors and they are accurate. Their accuracy is on the order of 1° and they have a slowly varying bias also on the order of 1° [Ows81]. The disadvantage of heading sensors is that they are expensive.

A second approach to array calibration is to use redundant information in the impinging signals to estimate the array shape [GWR89, TN88, Wah93]. A typical signal-based calibrator uses phase- or time-delay information from **calibrating signals** and estimates the hydrophone locations by imposing geometric constraints. If the calibrating signals are the same ones whose parameters are to be estimated then this is known as **self calibration**. This thesis deals largely with self-calibration methods and in part with the combination of data from self calibrators and heading sensors. Signals used for self calibration of towed arrays are assumed to be uncooperative. That is, there is no control over their DOA or spectrum and they can't be turned on and off as desired.

Array processors make use of correlations. The correlations are measured between pairs of sensors. The spatial separation between sensors is known as the **baseline** over which the correlation is measured. The correlations are functions of signal and noise parameters and spatial separation. Array processors estimate the signal parameters given the correlations as a function of separation (i.e. the known sensor positions). When the separations are unknown

a towed-array self calibrator estimates the sensor positions without knowledge of the signal parameters. Once the array has been calibrated the array processor then estimates the desired signal parameters. Estimating the sensor positions and signal parameters from the correlations is an inverse problem; i.e. knowing correlation as a function of separation, what is separation as a function of correlation?

Inverse problems are notoriously difficult. Towed-array self calibration is akin to finding the discrete Fourier transform of a signal from discrete samples without knowing the times at which the samples were taken. From this description, it is not obvious that the correlation function will be invertible. A proof of the existence of the inverse and the conditions under which it does is the first topic of this thesis.

However, the proof is necessary but not sufficient for practical applications. Although the correlation function is invertible, this does not indicate whether the inversion is well posed. A proof of invertibility is based on exact knowledge of the function (in our case, the correlations). In practice, the correlations are not known exactly and must be estimated in the presence of noise. Any algorithm that solves for the sensor and signal parameters will be sensitive, in some degree, to the noisy correlation estimates. An algorithm necessarily makes certain assumptions about the signals and noise. In practice the assumptions may not be entirely accurate. I discuss how sensitive an algorithm is to deviations from the assumed conditions and how robust it is to adverse conditions such as noisy correlation estimates.

I mentioned two approaches to towed-array calibration: sensor based and signal based. A third possibility is to combine the two approaches. Combining sensor and signal information will result in more accurate calibration. Problems to be overcome with this approach include synchronising data, proper weighting of data according to the accuracy of the individual measurements and combining the two measurement systems in an efficient framework.

1.1 Problem Setting

For the purpose of self calibration, the SNR of underwater acoustic signals can vary, as a guide only, from -20 dB to 10 dB. The range to the signal source and the type of vessel generating the signal affect the SNR; a merchant ship produces a lot of acoustic energy while a submarine is designed to produce very little. The spectra of vessel-generated signals are strongest at frequencies in the range of tens to hundreds of hertz [Coa90]. There are strong spectral lines at the frequencies of rotating machinery, such as the engine's and propeller shaft's, with harmonics at the propeller blade rate. Signal processing can be done in a broadband or narrowband context. Broadband processing can be used to obtain a spectral signature of a signal source. A skilled operator can look at the position of the spectral lines from a signal source

and name the type of vessel that makes them. Narrowband processing at one of the high SNR spectral lines can be used for DOA estimation. It may be argued that the SNR of underwater acoustic signals is too low for self-calibration to be feasible. This view is not supported by the literature. There are a number of papers that present successful sea-trials of signal-based algorithms [FGR92, Wah93, Buc78].

Acoustic noise is always present in towed arrays. It comes from three sources: ambient noise, tow-vessel noise and self noise [Coa90]. The ambient noise is generated by breaking waves, rainfall, marine life and so on. It is considered isotropic and directional; isotropic in the sense that a sensor will receive the same noise power at any point, given similar conditions and directional because more energy will arrive from some directions than others, depending on the presence of boundaries around the sensor. Tow-vessel noise is caused by the bow wave, engine noise, propeller cavitation, etc. Self noise of the towed array is due to micro effects of the cylinder being drawn through the water. Noise from surface waves, rainfall and array self noise has a continuous spectrum with Gaussian statistics. Signals from ships or submarines present a mixed spectrum with both continuous and discrete components.

The ocean behaves as a waveguide. Sound waves reflect off the surface with a phase inversion [Coa90] and scattering will occur when the surface is not calm. At the bottom of the ocean sound will be reflected from and transmitted into the sea bed. The speed of sound in the sea bed is higher than in water and so at angles of incidence greater than the critical angle total internal reflection occurs. Energy is lost when sound is transmitted into the sea bed. The presence of direct and reflected-path signals is called **multipath** propagation. The direct and reflected-path signals will be coherent and, unfortunately, many array processors are sensitive to coherent signals. It is important to consider the effects of signal coherence on array processing.

The speed of sound depends on three physical properties of the medium: specific heat at constant pressure, density and isothermal bulk modulus of elasticity [Coa90]. In distilled water at 20°C and atmospheric pressure the speed of sound is 1481 ms^{-1}. In the ocean the speed of sound is modelled as varying vertically but constant horizontally. In my simulations the speed of sound is 1500 ms^{-1}.

I show in Chapter 3 that for a self calibrator, up to six impinging signals are required to estimate an array's shape in 3D. The existence of so many uncooperative signals cannot be guaranteed. And so towed-array self calibration is viewed as a 2D problem which generally requires only one signal. The assumption of only two dimensions is an approximation but a reasonable one when signals are assumed to be in the far field and within a certain depth of the array.

1.2 Literature Overview

This section presents a very general and incomplete overview of the literature with emphasis on the more significant towed-array research. A more complete review is given in Chapter 5 which compares eight self calibrators with theory and computer simulation.

The dynamic behaviour of towed, thin, flexible cylinders was investigated by Paidoussis [Pai66a, Pai66b, Pai73a, Pai73b]. Paidoussis gave a differential equation describing the motion of a towed cylinder in response to tow-point induced motion. The differential equation was examined under special cases by Kennedy [Ken81], Kennedy and Strahan [KS81] and Ortloff and Ives [OI69]. Dowling examined the same special cases using a corrected version of Paidoussis' equation [Dow88a, Dow88b]. In a Kalman-filter calibrator [GAB88, GAB93], Gray et al. took advantage of a special form of the Paidoussis equation, valid for low-frequency disturbances, known as the **water-pulley** model. This Kalman-filter calibrator is significant because it uses the entire measurement history to calibrate the array as opposed to only the most recent measurements. No other known algorithms make use of the array's dynamic behaviour. The measurements in the Kalman-filter calibrator come from heading sensors.

Other heading-sensor-based calibrators have been developed by Owsley [Ows81, Ows84a]. The heading sensors are used to estimate a low order polynomial approximation of the array shape. The slowly varying heading-sensor biases are also estimated.

Self calibration has been a concern of astronomers for longer than it has been for sonar processors. Bucker [Buc78] and later Ferguson [Fer90b] adapted a technique known as **sharpness** for towed-array calibration. Sharpness was originally used to correct, in real time, atmospherically-distorted optical telescope images [MB74]. Sharpness was proven [HON77] to be identical to another self-calibration algorithm that makes use of redundant baselines [MM92].

A number of array calibrators rely on the assumption that there is only one narrowband signal impinging upon the array at a particular frequency or at a particular time (known as **disjoint source** assumption) [GWR89, Dor78, WRM94, AGP93, MM92]. This signal is called the **calibrating signal**. The calibrators are sensitive, in varying degrees, to the disjoint source assumption. Phase information from the calibrating signal is used to estimate the locations of the array's hydrophones.

Some calibrators use the eigenstructure of the array-covariance matrix [LM87, FW88]. They begin by estimating the number of signals that are represented in the array-covariance matrix. This non-trivial task relies on the relative magnitudes of the eigenvalues. An iterative scheme is used to obtain the unknown sensor positions and signal DOAs. Eigenstructure methods suffer

from a number of problems. They are sensitive to the presence of coherent signals and to low SNR and they have a large computational load.

A few array calibrators assume the availability of broadband signals with which to calibrate an array [TN88, Wah93]. They use time-delay estimates to estimate the locations of the array's hydrophones. Time-delay estimation is insensitive to coherent and interfering signals but tends to be more sensitive to noise than some of the narrowband calibrators.

1.3 Contributions

The thesis contributes the following knowledge on towed-array calibration:

1. A proof of the fundamental question of the invertibility of the spatial correlation function (Chapter 3). I prove this for generic arrays and also relate the results to the more specific case of towed arrays.
2. Closed-form solutions for the sensor positions and signal DOAs from signal phase or time-delay information for both 2D and 3D arrays (Section 3.2.2).
3. Three new towed-array calibrators, including one that makes simultaneous use of both heading-sensor and signal data (Chapter 4).
4. A method for reducing the number of computations of a Kalman Filter when there are more measurements than states (Section 4.4.4).
5. Analysis and comparison, using computer simulations, of a selection of towed-array calibrators from the literature (Chapter 5). I show how robust the calibrators are to signal-source distributions and noise. I show how sensitive they are to their underlying assumptions.
6. A new sharpness function that can be maximised to calibrate a towed array. This was found after analysing the sharpness algorithm (Chapter 6).

1.4 Thesis Outline

Chapter 2 introduces basic array processing. This includes a derivation of the array-covariance matrix and a formal definition of the array-calibration problem. The assumptions used in this thesis are given. Received signal information is expressed for both 2D and 3D arrays and narrowband and broadband signals. In Section 2.4 I briefly describe conventional beamforming. Section 2.5 gives the geometric constraints on a towed array's shape and describes a procedure for combining the constraints with signal information to obtain hydrophone position estimates. This procedure is known as the **chord approach**.

In Chapter 3 I give the conditions under which the spatial correlation function will be invertible. The analysis is applicable to generic arrays, for which only general sensor location information is known *a priori*. Similar analyses have been done in [RS87a, RS87b, Lo92]. The thesis generalises these analyses and clarifies a number of the results. The proofs are more intuitive than the ones given in [RS87a, RS87b, Lo92] as they are geometric rather than purely algebraic. In addition they yield closed form solutions for the sensor locations and signal DOAs from the phase-delay information. Based on the geometric constraints of Section 2.5, I infer the conditions for which sensor and signal parameters will be unique for towed arrays.

I give three new array-calibration algorithms in Chapter 4. Two of the algorithms use a least-square error optimisation. One uses a narrowband signal to estimate phase delays, and the other uses a broadband signal to estimate time delays. The broadband algorithm is insensitive to the presence of interfering and coherent signals. The third algorithm is based on a state-space model of the array shape that includes a model of the array's dynamic motion. The model allows signal and heading-sensor information to be combined easily. The states of the model define the array's shape and a Kalman filter is used to estimate the states. I use computer simulations to verify the theory.

In Chapter 5 I compare a number of representative array calibrators from the literature. They were chosen on the basis that all calibrators in the literature are similar to one of the representative calibrators. I identify the explicit and implicit assumptions made for each calibrator. Computer simulations are used to investigate the sensitivity of the calibrators to the underlying assumptions. I investigate how robust the calibrators are to variations in the distribution of signal sources and in the array shape. I found that broadband calibrators outperform narrowband calibrators in the presence of coherent signals.

Conflicting reports have been given concerning an algorithm known as sharpness. Bucker [Buc78] and Ferguson [Fer90b] report that the sharpness algorithm is an effective towed-array calibrator. Davidson and Cantoni [DC92] analyse sharpness algebraicly and show that the sharpness algorithm will work only in special cases and is generally unusable for towed arrays. In Chapter 6 I resolve the discrepancies between these reports. I investigate sharpness as it is applied to towed arrays and compare it with the original sharpness algorithm which was applied to optical telescopes. The sharpness algorithm is unique amongst signal-based calibration algorithms. It ostensibly makes no assumptions about the signals. Further, it is conceivable that it can be used to estimate parameters other than the array shape; the range to the signal sources, for example. Simulations reveal new sharpness functions that give more robust array-shape estimates than the functions in [Buc78, Fer90b].

The final chapter summarises the thesis and discusses the merits of various algorithms. I give some suggestions for further research topics.

Chapter 2 Array Processing

This chapter gives expressions for the hydrophone signals. I introduce the **travelling-wave** model of the signals and the **array-covariance matrix**. I use the same model of the array and signals as given in [Pil89]. The derivations for 2D arrays are essentially the same as for 3D arrays, the only difference being in the size of the vectors that describe the sensor positions and signal DOAs. In Chapter 3, 2D and 3D arrays are dealt with as separate cases. In the remaining chapters the array and all signal sources are assumed to lie in a horizontal plane.

2.1 Hydrophone Signals

In this section I make no assumption about the bandwidth of the signals. Assume that the signals impinging upon the array have an, as yet, unspecified bandwidth with centre frequency f_0 Hz. If the speed of sound in water is c_s then the wavelength at the centre frequency is $\lambda = c_s/f_0$. Throughout the thesis all distances are made dimensionless by normalising with $\lambda/2$.

Figure 1 Definition of coordinate system.

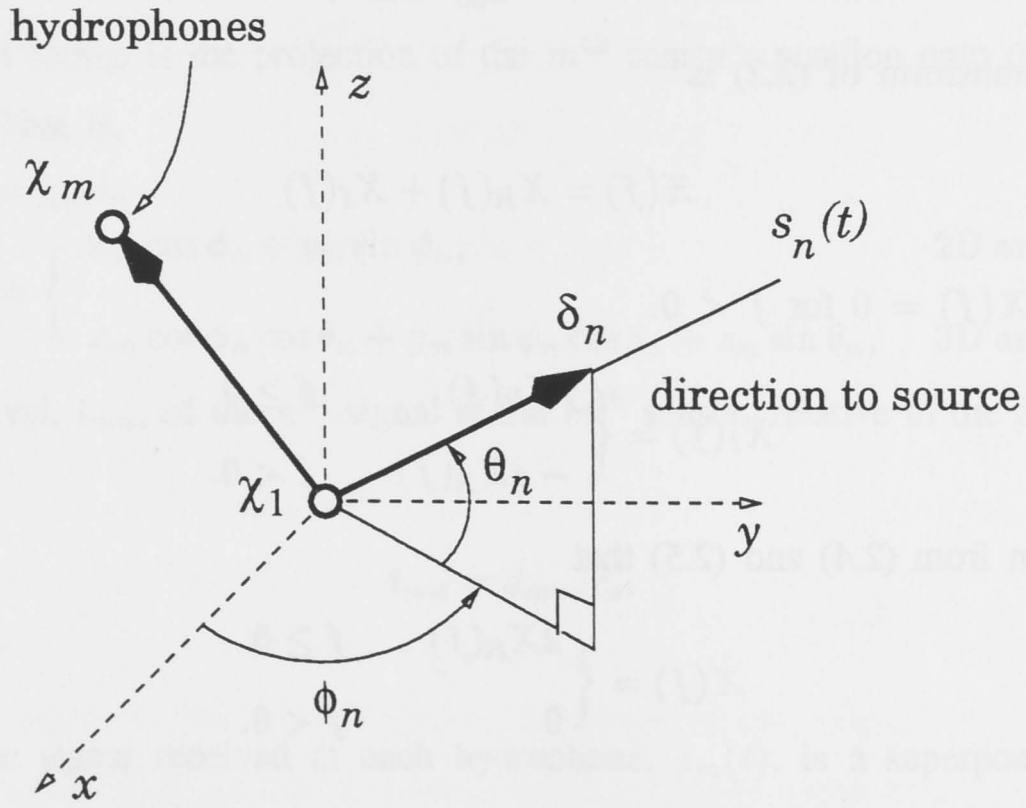

Let the array have M hydrophones and let the m^{th} be located at

$$\chi_m = \begin{cases} (x_m, y_m), & \text{2D array} \\ (x_m, y_m, z_m), & \text{3D array,} \end{cases} \tag{2.1}$$

as shown in Figure 1. A coordinate system is chosen in which the first hydrophone is at the origin, $\chi_1 = \mathbf{0}$, and the remaining $M - 1$ hydrophones have unknown locations.

If the array is equispaced and the distance between hydrophones is ρ then the optimum frequency for beamforming is one for which the signals have a wavelength of 2ρ. This frequency is known as the **design frequency**. It is optimum in the sense that the beamformer will have the highest resolution without spatial aliasing. It can be seen that if the centre frequency is also the design frequency $\rho = 1$.

Definition: Analytic Signals

Analytic signals have no negative frequency component. They are so named because they "represent the restriction to the real axis of an analytic function of a complex variable, i.e. they can be expanded in series in a region which contains this axis" [Bel84]. Let $x_R(t)$ be a real-valued signal and $x(t)$ be the corresponding analytic signal. Then $x_R(t)$ is the real part of $x(t)$ and

$$x(t) = x_R(t) + jx_I(t). \tag{2.2}$$

The real and imaginary functions, $x_R(t)$ and $x_I(t)$, are Hilbert transforms of each other:

$$x_I(t) = -\frac{1}{\pi} \int_{-\infty}^{\infty} \frac{x_R(t')}{t - t'} \mathrm{d}t'. \tag{2.3}$$

The Fourier transform of (2.2) is

$$X(f) = X_R(f) + X_I(f) \tag{2.4}$$

and because $X(f) = 0$ for $f < 0$,

$$X_I(f) = \begin{cases} jX_R(f) & f \geq 0 \\ -jX_R(f) & f < 0. \end{cases} \tag{2.5}$$

It can be seen from (2.4) and (2.5) that

$$X(f) = \begin{cases} 2X_R(f) & f \geq 0 \\ 0 & f < 0. \end{cases} \tag{2.6}$$

Sound signals are travelling waves. This means that sound pressure fluctuates as a function of time and of distance from the signal source. Suppose there are N impinging, analytic signals, $\{s_n(t)\}$. Let the DOAs of the signals be $\{\phi_n, \theta_n\}$, where ϕ_n is the azimuth and θ_n

is the elevation. Azimuth is measured from the positive x-axis in the xy-plane and elevation is measured from the xy-plane as shown in Figure 1. If the array and signals lie in a plane then $\theta_n = 0, \ \forall n$.

Assume that the signal sources are in the far field and the propagating medium is non-dispersive. The signal wavefronts that impinge upon the array will be planar. The **direction-cosine vectors**, $\{\delta_n\}$, are unit vectors in the DOAs of the signals and are given by

$$\delta_n = \begin{cases} [\cos\phi_n, \sin\phi_n]^{\mathrm{T}}, & \text{2D array} \\ [\cos\phi_n \cos\theta_n, \sin\phi_n \cos\theta_n, \sin\theta_n]^{\mathrm{T}}, & \text{3D array.} \end{cases} \tag{2.7}$$

Figure 2 Projection of sensor position onto the direction cosine vector.

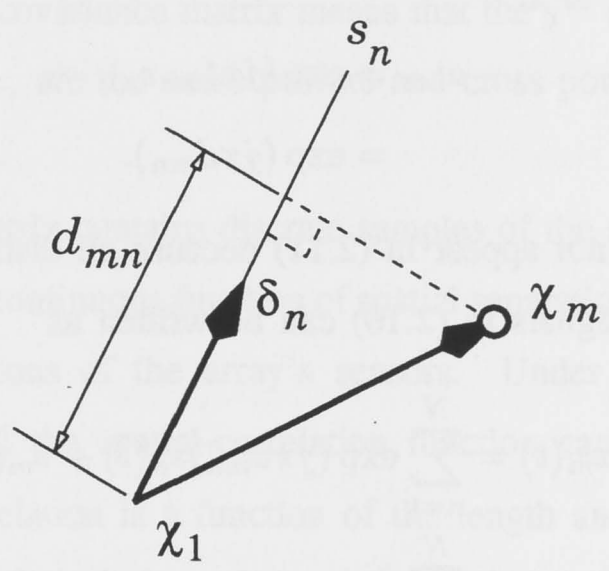

Refer to Figure 2. The distance, d_{mn}, from the first sensor to the m^{th} in the line of sight to the n^{th} signal source is the projection of the m^{th} sensor's position onto the n^{th} direction cosine vector. That is,

$$\begin{aligned} d_{mn} &= \chi_m \delta_n \\ &= \begin{cases} x_m \cos\phi_n + y_m \sin\phi_n, & \text{2D array} \\ x_m \cos\phi_n \cos\theta_n + y_m \sin\phi_n \cos\theta_n + z_m \sin\theta_n, & \text{3D array.} \end{cases} \end{aligned} \tag{2.8}$$

The time of arrival, t_{mn}, of the n^{th} signal at the m^{th} sensor, relative to the first, is therefore given by

$$t_{mn} = d_{mn}/c_s. \tag{2.9}$$

The analytic signal received at each hydrophone, $z_m(t)$, is a superposition of the N, appropriately-delayed impinging signals and noise. Noise includes effects such as internal electronic noise and external background noise. Therefore,

$$z_m(t) = \sum_{n=1}^{N} s_n(t - t_{mn}) + v_m(t), \tag{2.10}$$

where $v_m(t)$ is noise. Equation (2.10) is valid for both narrowband and broadband signals. I have assumed that the propagating medium is lossless in the region of the array so that the amplitude of the signals are unaffected, in the region of the array, by the distance they have travelled.

2.2 Narrowband Signals

Assume that the impinging signals are narrowband. I define what is meant by narrowband in an array-processing context in the next section. For the moment, a narrowband signal is one that has infinitesimal bandwidth. The time delays of (2.9) and (2.10) can be replaced with phase changes, $\{a_{mn}\}$, that are related to the time delays by

$$\begin{aligned} a_{mn} &= \exp\left(j\pi t_{mn} c_s\right) \\ &= \exp\left(j\pi d_{mn}\right). \end{aligned} \tag{2.11}$$

Note that wavelength does not appear in (2.11) because all distances are normalised by $\lambda/2$. Thus, the sum of delayed signals in (2.10) can be written as

$$\begin{aligned} z_m(t) &= \sum_{n=1}^{N} \exp\left(j\pi d_{mn}\right) s_n(t) + v_m(t) \\ &= \sum_{n=1}^{N} a_{mn} s_n(t) + v_m(t). \end{aligned} \tag{2.12}$$

Using matrix notation: $\mathbf{z}(t) = [z_1(t), \ldots, z_M(t)]^{\mathrm{T}}$, $\mathbf{s}(t) = [s_1(t), \ldots, s_N(t)]^{\mathrm{T}}$, $\mathbf{v}(t) = [v_1(t), \ldots, v_M(t)]^{\mathrm{T}}$ and $\mathbf{A}$ is the matrix of elements $\{a_{mn}\}$. Then,

$$\mathbf{z}(t) = \mathbf{A}\mathbf{s}(t) + \mathbf{v}(t). \tag{2.13}$$

The N column vectors, $\{\mathbf{a}_n\}$, of $\mathbf{A}$ are known as **steering vectors**. A steering vector represents the relative complex amplitude of a signal as it arrives at each hydrophone.

2.3 Array-Covariance Matrix

The array-covariance matrix, sometimes called **cross-spectral matrix**, is important in processing narrowband array signals. The elements of the array-covariance matrix are the correlations of pairs of signals received by the sensors of the array. I assume the following:

1. noise is uncorrelated with the signals, and
2. the array shape and signal DOAs are changing slowly.

The array-covariance matrix, $\mathbf{R}$, is given by

$$\begin{aligned}\mathbf{R} &= \langle \mathbf{z}(t)\mathbf{z}^{\mathrm{H}}(t) \rangle \\ &= \mathbf{A}\langle \mathbf{s}(t)\mathbf{s}^{\mathrm{H}}(t) \rangle \mathbf{A}^{\mathrm{H}} + \langle \mathbf{v}(t)\mathbf{v}^{\mathrm{H}}(t) \rangle \\ &= \mathbf{A}\mathbf{R}_s\mathbf{A}^{\mathrm{H}} + \mathbf{R}_n,\end{aligned} \tag{2.14}$$

where superscript H is the Hermitian transpose operator, and $\langle \ldots \rangle$ denotes a time average. The matrix of steering vectors, $\mathbf{A}$, is taken outside the time average because it is approximately constant for the period of averaging if assumption 2 is true. The matrix $\mathbf{R}_n = \langle \mathbf{v}(t)\mathbf{v}^{\mathrm{H}}(t) \rangle$ is called the **noise-covariance matrix** and $\mathbf{R}_s = \langle \mathbf{s}(t)\mathbf{s}^{\mathrm{H}}(t) \rangle$ is called the **signal-covariance matrix**. The diagonal elements of $\mathbf{R}_s$ are the signal powers and the off-diagonal elements are the cross powers. If the signals are incoherent $\mathbf{R}_s$ is diagonal. A non-zero value at the $(jk)^{\mathrm{th}}$ element of the signal-covariance matrix means that the j^{th} and k^{th} signals are coherent. Likewise, the elements of $\mathbf{R}_n$ are the noise powers and cross powers and if noise is spatially uncorrelated $\mathbf{R}_n$ is diagonal.

The array-covariance matrix contains discrete samples of the spatial **correlation function**. The correlation function is a continuous function of spatial separation but the function is sampled only at the discrete separations of the array's sensors. Under the infinitesimal bandwidth assumption from Section 2.2 the spatial-correlation function can be seen by expanding one of the terms in the $\mathbf{R}$. Correlation is a function of the length and orientation of the baseline upon which it is observed. It is independent of the position of that baseline if the signals originate in the far field; i.e. if the wavefronts are planar. Expanding (2.14), (2.11) and (2.8), the noise-free correlation as a function of separation for one signal is

$$r(\chi_j - \chi_k) = \sigma_s^2 \exp\left(j\pi(\chi_j - \chi_k)\delta_1\right), \tag{2.15}$$

where σ_s^2 is the signal power. Using $\chi = \chi_j - \chi_k$,

$$r(\chi) = \sigma_s^2 \exp\left(j\pi\chi\delta_1\right). \tag{2.16}$$

This is a periodic function.

If the signals have finite bandwidth with a rectangular passband then the observed spatial correlation function will be modulated by a sinc-function envelope [Tho89]. The width of the main lobe of the sinc function is approximately c_s/BW where BW is the bandwidth of the impinging signals. Because of the envelope the full amplitude of the spatial correlation function is observed only when the distance between sensors in the direction of the signal is zero (i.e. $d_{mn} = 0$). The longest baseline for which the spatial correlation function amplitude is within $x\%$ of the maximum value, where x is small, can be obtained from [Tho89],

$$\left(\pi BW \frac{d_{mn}}{c_s}\right)^2 < \frac{6x}{100}. \tag{2.17}$$

For example if the array is 100 m long and beams are formed at all angles to endfire ($d_{mn} = 100$) and 10% attenuation of the spatial correlation function is allowable then the bandwidth must be less than 3.7 Hz. Therefore, narrowband, in an array processing context, is any bandwidth smaller than that defined by (2.17).

Equations (2.7) to (2.14) describe how to obtain the exact array-covariance matrix given the signal, sensor and noise parameters. This is the forward problem. The array-covariance matrix contains discrete samples of the spatial correlation function. Array calibration is the inverse problem. Given the discrete samples of the correlation function, without knowing the baselines on which they were measured, the aim of self-calibration is to find those baselines; the baselines define the array shape.

2.3.1 Signal model – deterministic or random?

There are two models commonly used to describe the signals:

Deterministic the signal is represented as a phasor, i.e. it is a constant complex number, and

Random the signal is a random, zero-mean, complex variable.

The choice of model does not affect the signal and correlation equations (2.13), (2.14) and (2.15). However, model choice does affect the second order statistics of the signals and their correlations. In Section 4.4 I use the second order statistics of a self calibrator. I assumed a random signal model. Elsewhere, I have not been concerned with the statistics and so the choice of signal model is unimportant. There is no clear argument for or against using either of the models.

2.4 Beamforming

The purpose of array processing is to isolate a wanted signal from interfering signals and noise and to estimate parameters of the isolated signal such as DOA or power. This is spatial filtering. A **beamformer** (also known as **delay-and-sum beamformer** and **conventional beamformer**) estimates received power, $P_b(\phi, \theta)$, as a function of DOA [Pil89]. It delays the hydrophone signals and sums them so that, for a given look direction, a signal arriving from that direction is summed coherently (see Figure 3). The summed signal is squared and averaged to obtain a power estimate. Signals not in the look direction are summed destructively. The delays, $\{\tau_m\}$, equal the path delays given in (2.9) when the look direction is the same as the

n^{th} signal's DOA. That is, $\tau_m = \chi_m \delta_{\phi,\theta}$, where

$$\delta_{\phi,\theta} = \begin{cases} [\cos\phi, \sin\phi]^{\mathrm{T}}, & \text{2D array} \\ [\cos\phi\cos\theta, \sin\phi\cos\theta, \sin\theta]^{\mathrm{T}}, & \text{3D array.} \end{cases} \tag{2.18}$$

Thus, beamformer power is

$$P_b(\phi,\theta) = \left\langle \left| \sum_{m=1}^{M} z_m(t + \tau_m(\phi,\theta)) \right|^2 \right\rangle. \tag{2.19}$$

Figure 3 Schematic of a delay and sum beamformer.

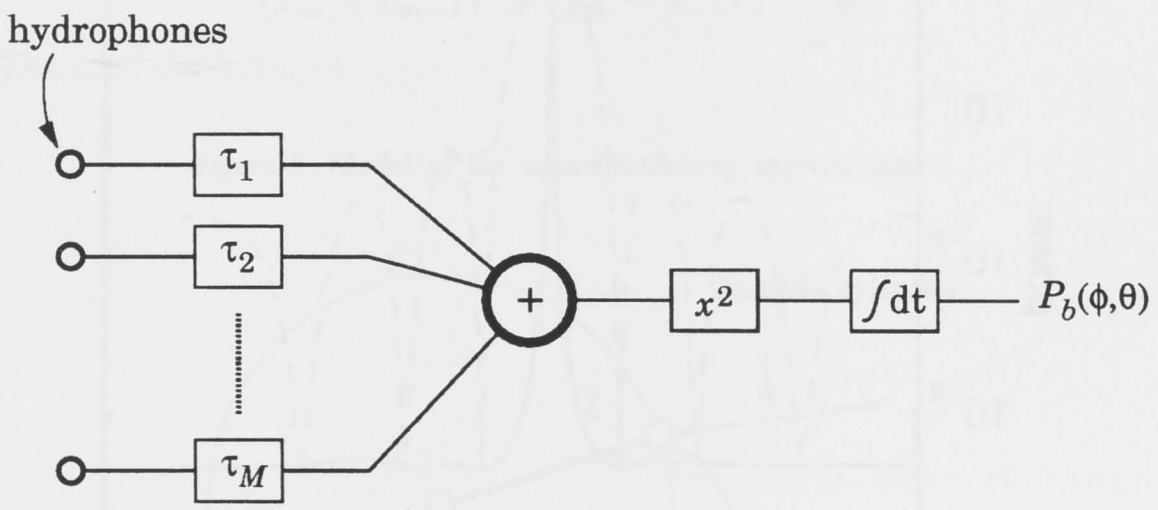

If the signals are narrowband then, as in Section 2.2, the time delays can be replaced by phase changes, $w_m(\phi,\theta) = \exp(j\pi\tau_m(\phi,\theta)c_s)$. The **weight vector** for the conventional beamformer is

$$\mathbf{w} = [\exp(j\pi\tau_1 c_s), \ldots, \exp(j\pi\tau_M c_s)]^{\mathrm{T}}. \tag{2.20}$$

Therefore, the beamformer power is

$$\begin{aligned} P_b &= \left\langle \left| \mathbf{w}^{\mathrm{H}}\mathbf{z} \right|^2 \right\rangle \\ &= \left\langle \mathbf{w}^{\mathrm{H}}\mathbf{z}\mathbf{z}^{\mathrm{H}}\mathbf{w} \right\rangle \\ &= \mathbf{w}^{\mathrm{H}} \left\langle \mathbf{z}\mathbf{z}^{\mathrm{H}} \right\rangle \mathbf{w} \\ &= \mathbf{w}^{\mathrm{H}}\mathbf{R}\mathbf{w}. \end{aligned} \tag{2.21}$$

A beamformer image for a uniform array with 7 sensors and a single impinging signal broadside to the array is shown in Figure 4 (dashed line).

There are other algorithms that estimate power or DOA. One of them is the Capon estimator which I will describe without going into any mathematical detail. The Capon estimator has better resolution than the conventional beamformer but it is more sensitive to sensor-position errors. It achieves this by choosing a weight vector such that the received power is minimised

while constraining the gain in the look direction to be unity. This has the effect of reducing power-estimate bias caused by interfering signals. The weight vectors of the Capon estimator are calculated from the array-covariance matrix unlike the conventional beamformer where they are independent of the signals and so can be calculated off line. A Capon estimator image for a uniform array with 7 sensors and a single impinging signal broadside to the array is shown in Figure 4 (solid line).

Figure 4 Images from a uniform, 7–sensor array using a conventional beamformer (dashed line) and a Capon estimator (solid line).

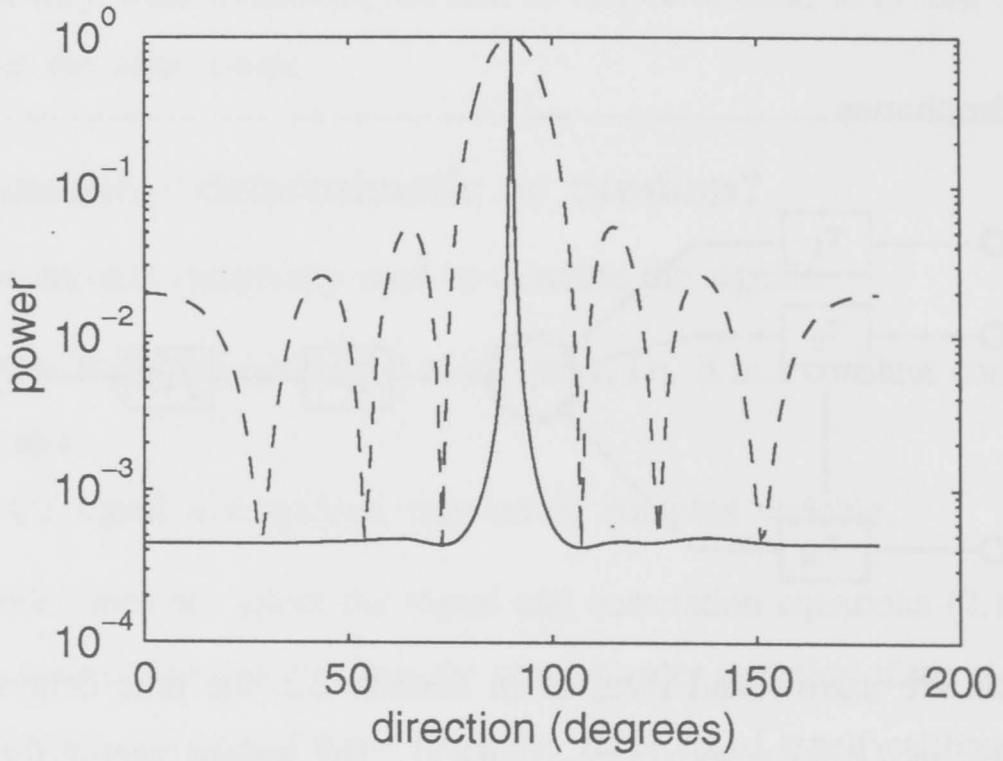

2.5 Geometric Constraints and the Chord Approach

In this section I show how constraints on the shape of a towed array simplify the problem of estimating it. A number of self-calibrators in the literature, as well as those presented in Chapter 4, make use of what Gray et al. [GWR89] call the **chord approach**. The chord approach is simply a method of combining known constraints on the array's geometry with a calibrating signal's phase- or time-delay information to estimate the array shape. It is assumed that the array is 2D and the calibrating-signal source lies in the plane of the array.

Self calibrators can give estimates of the *shape* of an array and the DOA of the impinging signals in relation to the estimated shape. However, there will always be a rotational and reflectional ambiguity to the shape unless supplemental information is available[1]. In this section, I show how a single heading sensor added to the array can eliminate the rotational ambiguity and

[1] Rotational and reflectional ambiguities are described in Chapter 3. Without additional information, such as from heading sensors, a self calibrator can not give the orientation of the array with respect to an arbitrary coordinate system, such as the earth's magnetic field.

a second heading sensor can eliminate the reflectional ambiguity. The supplemental heading-sensor information is easily integrated with the chord approach.

Let the inter-hydrophone arc length of the flexible cylinder bearing the array be ρ. If the flexible cylinder is assumed not to stretch then each hydrophone must lie within a circle (or sphere in 3D) of radius ρ that is centred on the previous hydrophone. Further, if the distance between hydrophones is not large then the flexible cylinder can be approximated by straight line segments between hydrophones. Each hydrophone will, therefore, lie on the circumference of the circle (or sphere in 3D) of radius ρ that is centred on the previous hydrophone (see Figure 5). That is,

$$(x_m - x_{m-1})^2 + (y_m - y_{m-1})^2 = \rho^2. \tag{2.22}$$

Figure 5 Model of the segmented array approximation.

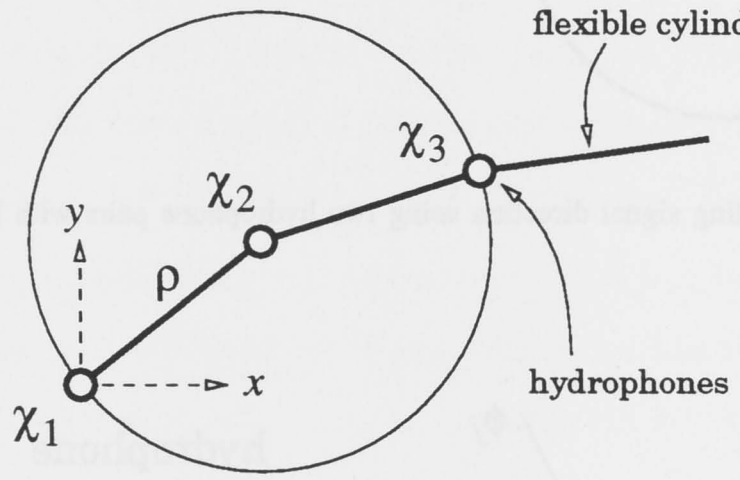

The distance between the wavefronts of the calibrating signal arriving at one hydrophone and the next, $d_{mn} - d_{m-1,n}$, equals the difference between the relative arrival times of the signal multiplied by the speed of sound,

$$d_{mn} - d_{m-1,n} = c_s(t_{mn} - t_{m-1,n}). \tag{2.23}$$

I will drop the subscript n because we are dealing with only one signal. Assume that the DOA of the calibrating signal, ϕ, is known. A coordinate system is chosen so that the first hydrophone is at the origin and the tow vessel is travelling in the negative x-direction. To be consistent with the relative time of arrival, t_m, the location, (x_m, y_m), of the m^{th} hydrophone must be on the straight line

$$\begin{aligned}(x_m - x_{m-1})\cos\phi + \\ (y_m - y_{m-1})\sin\phi = \ d_m - d_{m-1}.\end{aligned} \tag{2.24}$$

This line is the signal's wavefront at a distance $d_m - d_{m-1}$ before the $(m-1)^{\text{th}}$ hydrophone. The location of the m^{th} hydrophone is at the intersection of (2.24) and (2.22). There are two

simultaneous solutions to (2.24) and (2.22) so to resolve this twin ambiguity we choose the solution that is closest to the tow-vessel's path (i.e. the x-axis), given by

$$\begin{aligned} x_m &= \cos\phi(d_m - d_1) + \sin\phi \sum_{k=1}^{m} \sqrt{\rho^2 - (d_k - d_{k-1})^2} \\ y_m &= \sin\phi(d_m - d_1) - \cos\phi \sum_{k=1}^{m} \sqrt{\rho^2 - (d_k - d_{k-1})^2}, \end{aligned} \tag{2.25}$$

and as shown in Figure 6.

Figure 6 Choose the solution closest to the tow-vessel's path.

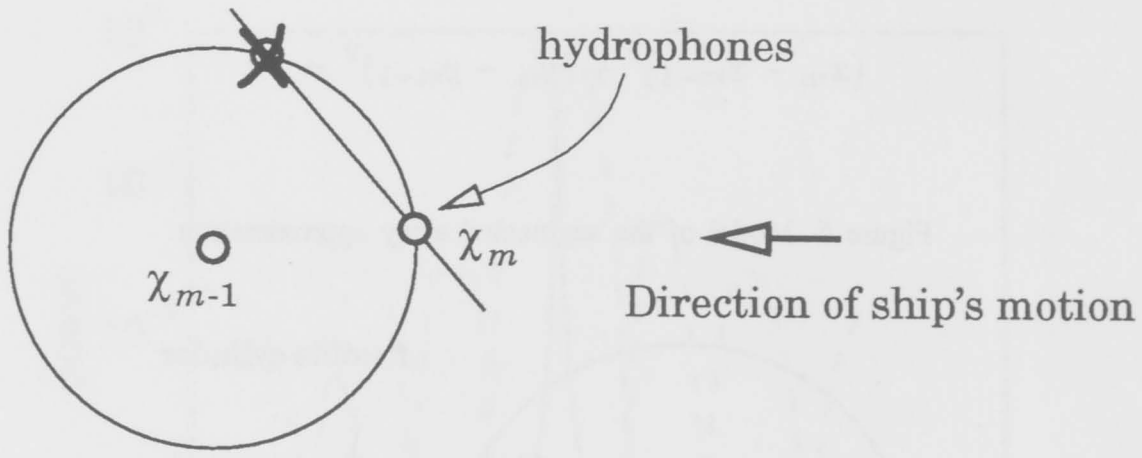

Figure 7 Estimating signal direction using two hydrophone pairs with heading sensors.

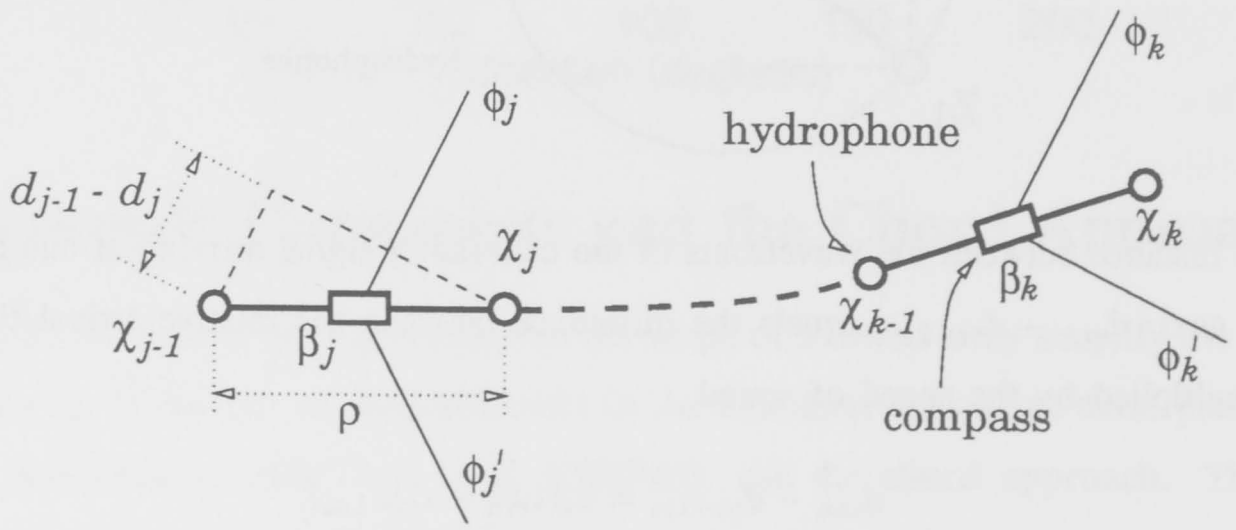

When the calibrating signal's DOA is not known it must be estimated. It can be seen from Figure 7 that $d_j - d_{j-1} = \rho\cos\phi_j$, and so

$$\phi_j = \cos^{-1}\left(c_s(t_j - t_{j-1})/\rho\right) \tag{2.26}$$

which has two solutions. We resolve this ambiguity by equipping two pairs of adjacent hydrophones, $(j-1, j)$ and $(k-1, k)$, with heading sensors to measure the absolute bearing of their baselines. Each pair of hydrophones will give two solutions, one corresponding to the real source direction, ϕ_j, and the other a virtual source direction, ϕ_j'. The virtual source always appears as a reflection of the real source in the pair's baseline. The absolute bearing, α_j, of a

source whether it be real or virtual is $\alpha_j = \phi_j + \beta_j$ where β_j is the heading sensor measurement of that baseline. If $\beta_j \neq \beta_k$ then $\alpha_j = \alpha_k$ and $\alpha'_j \neq \alpha'_k$, which eliminates the ambiguity. If $\beta_j = \beta_k$ the two special baselines are parallel and the ambiguity can not be resolved.

From the perspective of array-shape ambiguities, the first heading sensor removes the rotational ambiguity and the second sensor removes the reflectional ambiguity. Using the two heading sensors to determine the calibrating-signal DOA ensures that the estimated array shape will agree with the measurements from the heading sensors.

Chapter 3 Inverting the Spatial Correlation Function

3.1 Problem Description and Background

In the literature on towed-array self calibration there is an implicit assumption that there is enough information in the impinging signals to estimate both the array shape and the signals' parameters. It is important to verify that this assumption is true; and under what conditions. The conditions tell us whether there are certain assumptions that a self calibrator must make to estimate the array shape unambiguously and, if the assumptions are incorrect, what form an ambiguity will take. The form of an ambiguity might be whether a sensor exists in one of a finite number of positions or in one an infinite number. This chapter deals with both generic and towed arrays. I show that for towed arrays, if there is only one signal, every hydrophone will have two possible positions. If there is a second signal the ambiguity is eliminated.

I present the necessary conditions for uniqueness of the spatial correlation function's inverse. That is, I give the conditions for the locations of an array's sensors and the parameters of the signals that impinge upon the array to be unique. The only information used is the exact narrowband array-covariance matrix which is derived purely from the impinging signals. No attempt is made to analyse the sensitivities of the sensor and signal parameters' estimates when the array-covariance matrix is not known exactly. Nor does this chapter include algorithms for estimating these parameters, only evidence that a hypothetical algorithm will or will not have a unique solution to search for. In the manner of control systems theorists, I will say that the sensor and signal parameters are **observable** if they are unique for a given array-covariance matrix.

If the signals are incoherent with each other then at least three signals for a two-dimensional array, and six for a three-dimensional array are required to determine the sensor, signal and noise parameters uniquely. If all signals originate from one source, and are thus coherent with each other, there is an infinite number of solutions for the sensor and signal parameters. The question of observability is unanswered when there are coherent signals and two or more signal sources.

Observability of the sensor and signal parameters was investigated by Rockah and Schultheiss [RS87a, RS87b], for two-dimensional arrays. They assumed that the signals are distinct from one another by virtue of being separated spectrally or temporally. Such an analysis

is useful if one has the option to deploy controlled signal sources, or can otherwise guarantee that the signals will be disjoint. Rockah and Schultheiss gave the number of signals and sensors required for observability, for both near- and far-field signal sources. They demonstrated that, without additional information, translational or rotational uncertainties of the array shape and signal field would be inevitable. Signals can only give information about the shape of an array and the distribution of the signal sources in relation to the array; they give no information about the absolute position of the array or its orientation. Thus, if one solution can be found for the array shape and signal DOAs, any translation, rotation or reflection of that solution will also be a solution (see Figure 8). These ambiguities can be eliminated by assuming that the location of three sensors, two sensors and a signal DOA, or one sensor and two signal DOAs are known *a priori*. However, for this chapter, I will regard all translations, rotations and reflections as trivial duplications of the one solution.

Figure 8 Translations (b), rotations (c) and reflections (d) are regarded as trivial duplications of the one solution (a).

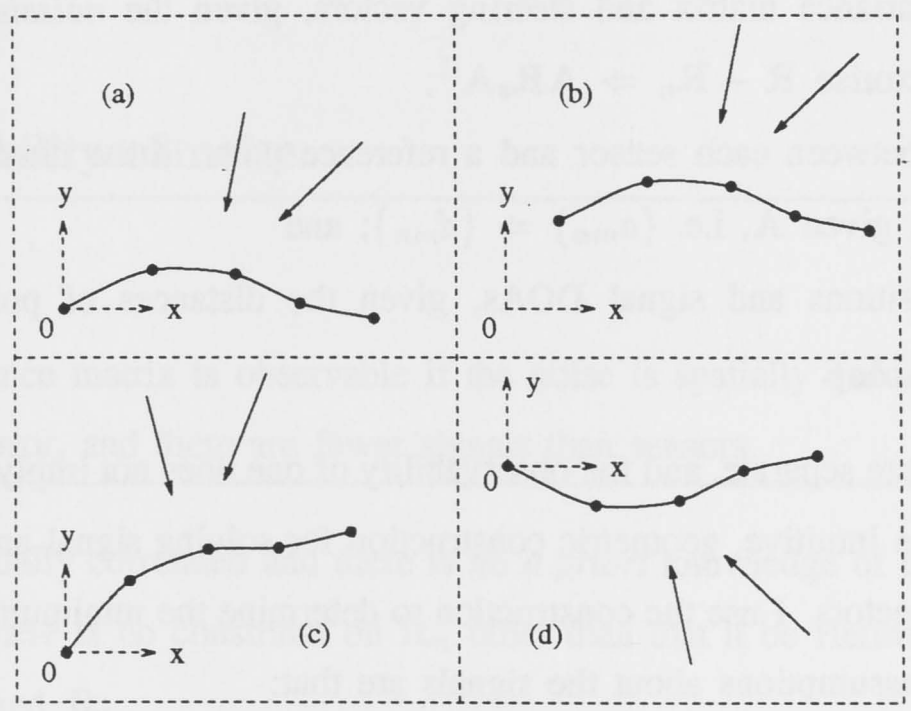

Lo and Marple [Lo92] investigated the more general problem of observability conditions when the signals are not spectrally or temporally disjoint. This involved another question; are the two or more steering vectors that make up the array-covariance matrix unique? Schmidt [Sch81] called this **rank-*n*** ambiguity. Lo and Marple assumed that all the signals are incoherent with one another, and that the noise-covariance matrix is known. They gave a proof for the minimum required numbers of signals and sensors to estimate their parameters from the steering vectors, which confirmed the results of [RS87a, RS87b]. The proof bears no obvious relation to what is a geometric problem, and so is not illuminating.

Here I discuss the following topics that are not treated in [RS87a, RS87b, Lo92]: observability of the noise-covariance matrix, 3D arrays, coherent signals and closed-form solutions for the sensor and signal parameters, given phase information from the signals. In Section 3.2 I

generalise the results of [RS87a, RS87b] and [Lo92]. The observability of noise characteristics is discussed in Section 3.2.1. If noise is assumed spatially correlated then it, and the signal and sensor parameters, will be unobservable. If noise is spatially uncorrelated and noise power is equal at all sensors, and if there are fewer signals than sensors, then the noise power is observable. Section 3.2.2 discusses the observability of the sensor and signal parameters, given that the noise-covariance matrix is known or deduced, and assuming that the signals are incoherent. The generalised results include conditions on

1. the minimum numbers of sensors and signals necessary to observe their parameters, when the array and signal sources are assumed to exist in two and three dimensions, and
2. a lower bound on the numbers of signals and sensors required when at least some of the signals are assumed to be coherent.

There are three issues involved here; these are observability of

1. the signal-covariance matrix and steering vectors, given the *noiseless* array-covariance matrix, i.e. factorise $\mathbf{R} - \mathbf{R}_n \Rightarrow \mathbf{A}\mathbf{R}_s\mathbf{A}^{\mathrm{H}}$;
2. the distances between each sensor and a reference point in the direction of each of the signal sources, given $\mathbf{A}$, i.e. $\{a_{mn}\} \Rightarrow \{d_{mn}\}$; and
3. the sensor positions and signal DOAs, given the distances of point 2, i.e. factorise $\{d_{mn}\} \Rightarrow \{\chi_m \delta_n\}$.

These three issues are separate, and the observability of one does not imply observability of the others. I provide an intuitive, geometric construction for solving signal and sensor parameters from the steering vectors. I use the construction to determine the minimum numbers of signals and sensors. The assumptions about the signals are that:

1. the signals are narrowband,
2. the signals are uncorrelated with noise,
3. the signals are neither spectrally nor temporally disjoint, and
4. there are fewer signals than sensors.

In Sections 3.2.3 and 3.2.4, I discuss the question of observability assuming that some or all of the signals are coherent. In the first case, I assume that there is just one signal source, with multiple, coherent signals originating from it, and in the second I assume that there are two or more signals sources, with at least two coherent signals. I show that in the first case the sensor and signal parameters are unobservable and give an example. I provide no proof of the observability conditions for the second case but offer a conjecture based upon the number of unknown parameters to be observed.

In Section 3.3 I relate the results of Section 3.2.2 to towed arrays. This is simply a matter of taking what we have learned in this Chapter and applying the geometric constraints of Section 2.5 to it.

3.2 Uniqueness of the Factorisation of the Array-Covariance Matrix

In this section I show the necessary conditions for the parameters, $\{\chi_m, \phi_n, \theta_n, \mathbf{R}_s, \mathbf{R}_n\}$, of a given array-covariance matrix, $\mathbf{R}$, to be observable, ignoring translations, rotations and reflections. Conditions on spatial correlation of noise and coherence of signals are treated separately. To avoid translational, rotational and reflectional ambiguities I use a coordinate system that is aligned with some of either the sensors or the signals. For convenience, (2.14) is rewritten below:

$$\mathbf{R} = \mathbf{A}\mathbf{R}_s\mathbf{A}^{\mathrm{H}} + \mathbf{R}_n. \tag{3.1}$$

3.2.1 Observability of noise.

Theorem 1

The noise-covariance matrix is observable if the noise is spatially uncorrelated with equal power at each sensor, and there are fewer signals than sensors.

If noise is spatially correlated and there is no *a priori* knowledge of the noise-covariance matrix, $\mathbf{R}_n$, then there is no constraint on $\mathbf{R}_n$ other than that it be Hermitian. Therefore, for any choice of $\mathbf{A}$ and $\mathbf{R}_s$,

$$\mathbf{R}_n = \mathbf{R} - \mathbf{A}\mathbf{R}_s\mathbf{A}^{\mathrm{H}}, \tag{3.2}$$

there is an infinite number of solutions to (3.1), and the noise, sensor and signal parameters are unobservable. When the noise is spatially uncorrelated, the noise-covariance matrix, $\mathbf{R}_n$, is diagonal. Assume that the noise powers are equal at every receiver, σ^2, so that

$$\mathbf{R}_n = \sigma^2\mathbf{I}, \tag{3.3}$$

where $\mathbf{I}$ is the identity matrix. In a real system there must be at least one solution to (3.1), which we nominate $\mathbf{A}\mathbf{R}_s\mathbf{A}^{\mathrm{H}} + \mathbf{R}_n$. Suppose a second, hypothetical, solution, $\mathbf{B}\mathbf{R}'_s\mathbf{B}^{\mathrm{H}} + \mathbf{R}'_n$ exists, where $\mathbf{R}'_n = \epsilon^2\mathbf{I}$, so that

$$\begin{aligned} \mathbf{R} = \mathbf{A}\mathbf{R}_s\mathbf{A}^{\mathrm{H}} + \mathbf{R}_n &= \mathbf{B}\mathbf{R}'_s\mathbf{B}^{\mathrm{H}} + \mathbf{R}'_n, \\ \mathbf{A}\mathbf{R}_s\mathbf{A}^{\mathrm{H}} - \mathbf{B}\mathbf{R}'_s\mathbf{B}^{\mathrm{H}} &= \mathbf{R}'_n - \mathbf{R}_n. \end{aligned} \tag{3.4}$$

It can be shown that $\mathbf{A}\mathbf{R}_s\mathbf{A}^{\mathrm{H}}$ and $\mathbf{B}\mathbf{R}'_s\mathbf{B}^{\mathrm{H}}$ have equal rank and, furthermore, the columns of $\mathbf{A}$ and the columns of $\mathbf{B}$ span the same space (see Appendix A). Thus, the rank of $\mathbf{R}'_n - \mathbf{R}_n$ is equal to or less than the rank of $\mathbf{A}\mathbf{R}_s\mathbf{A}^{\mathrm{H}}$. But $\mathbf{R}'_n - \mathbf{R}_n = \left(\epsilon^2 - \sigma^2\right)\mathbf{I}$, which is either full rank or zero rank if $\epsilon^2 = \sigma^2$. But $\mathbf{A}\mathbf{R}_s\mathbf{A}^{\mathrm{H}}$ is not full rank, which is the case when there are fewer signals than sensors. Therefore $\mathbf{R}'_n = \mathbf{R}_n$ and $\mathbf{A}\mathbf{R}_s\mathbf{A}^{\mathrm{H}} = \mathbf{B}\mathbf{R}'_s\mathbf{B}^{\mathrm{H}}$. And so, when the noise is spatially uncorrelated, with equal power at every receiver, the noise power, σ^2, and hence the noise-covariance matrix, is observable.

Once the noise-covariance matrix is known, the observability of sensor and signal parameters depends on whether the factorisation of the *noiseless* covariance matrix, $\mathbf{R}_a = \mathbf{R} - \mathbf{R}_n$, is unique. I address this in two parts; when the signals are incoherent, and when they are coherent.

3.2.2 Observability of signal and sensor parameters when the signals are incoherent and noise is spatially uncorrelated.

When the noise is spatially uncorrelated and has equal power at every receiver, Section 3.2.1 showed that the noise-covariance matrix in (3.1) is observable. Now I look at whether the sensor positions, and signal DOAs and powers are observable, given the noiseless covariance matrix,

$$\mathbf{R}_a = \mathbf{A}\mathbf{R}_s\mathbf{A}^{\mathrm{H}}. \tag{3.5}$$

This depends on three separate observability issues:

1. from (3.1), $\mathbf{A}$ must be observable when given $\mathbf{R}_a$,
2. from (2.11), $\{d_{mn}\}$ must be observable when given $\{a_{mn}\}$, and
3. from (2.8), $\{\chi_m\}$ and $\{\phi_n\}$ (or $\{\phi_n, \theta_n\}$ in the 3D case) must be observable when given $\{d_{mn}\}$.

Conditions for the observability of the signal and sensor parameters under various conditions are given in [Lo92]. For completeness, I include a brief explanation of the results for the first two points in the above list. For the third point I provide a proof of the necessary conditions using geometric constructions.

Theorem 2

Matrix $\mathbf{A}$ is observable, given $\mathbf{R}_a$, if the signals are incoherent, and a linear combination of the steering vectors in $\mathbf{A}$ does not give another steering vector.

We know that for uncorrelated signals, $\mathbf{R}_s$ must be diagonal, positive and full rank, because each element on the diagonal of $\mathbf{R}_s$ represents a signal power, and the steering vectors of $\mathbf{A}$ must have elements with unit magnitude. As shown in Appendix A, all solutions for $\mathbf{A}$ in (3.5)

will exist in one common subspace, $\mathbb{C}^N$, of the space, $\mathbb{C}^M$, when the number of signals, N, is less than the number of sensors, M. Therefore a solution for $\mathbf{A}$ must lie on the intersection of the subspace $\mathbb{C}^N$ and the set of all possible steering vectors (i.e. complex vectors that have all elements with unit magnitude). Because we are dealing with a real system, there must be at least one solution to (3.1); let that solution be $\mathbf{A}\mathbf{R}_s\mathbf{A}^{\mathrm{H}}$. Any other solution for $\mathbf{A}$, say $\mathbf{B}$, can therefore be expressed as a linear combination of $\mathbf{A}$, given by $\mathbf{B} = \mathbf{A}\mathbf{U}$, where $\mathbf{U}$ is an $N \times N$ matrix. However, apart from some special cases, there is no matrix, $\mathbf{U}$, that will result in all columns of $\mathbf{B}$ being steering vectors. It was shown in [Lo92] that when there are two signals, the columns of $\mathbf{B}$ can be steering vectors if, and only if, all sensors lie on two parallel lines whose direction bisects the DOAs of the two signals, as shown in Figure 9. It was conjectured that when there are more than two signals, $N > 2$, the columns of $\mathbf{B}$ can be steering vectors if, and only if, there is an $N \times N$ sub matrix of $\mathbf{A}$ that is full rank and every other row of $\mathbf{A}$ is a scalar multiple of one of the rows of the sub matrix. This is physically impossible when there are more than three signals. Because the sensor positions and signal DOAs are independent of each other the chances of these constraints being met are small, and so, in general, no matrix $\mathbf{U}$ exists such that $\mathbf{B} = \mathbf{A}\mathbf{U}$ is composed of steering vectors. The trivial exceptions to this are the elementary column-swapping matrices, which are simply an identity matrix with two or more columns switched around. Their effect is simply to renumber the sensors. Therefore, apart from these special cases, $\mathbf{A}$ and $\mathbf{R}_s$ are observable given $\mathbf{R}_a$, when the signals are incoherent.

Figure 9 A linear combination of two steering vectors will be a steering vector only if all sensors lie on two parallel lines whose direction bisects the DOAs of the two signals.

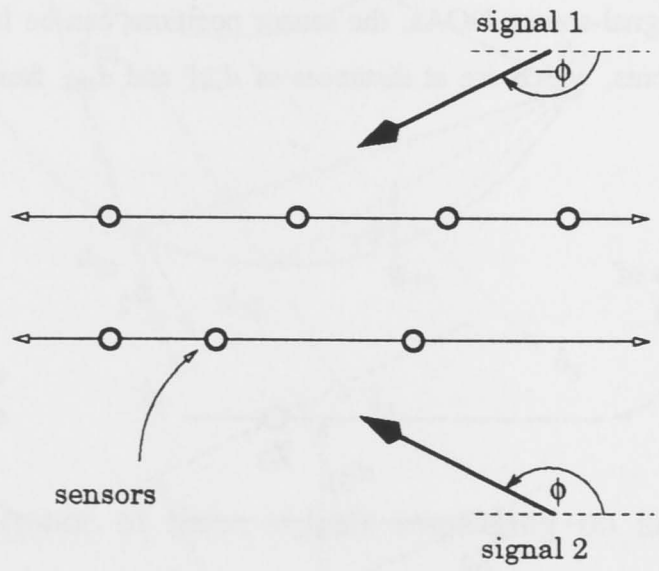

The second observability issue, obtaining the $\{d_{mn}\}$ from the $\{a_{mn}\}$, depends on (2.11).

Theorem 3

The distances, $\{d_{mn}\}$, from the reference point to the sensors in the DOAs of the signals are observable, given matrix $\mathbf{A}$, if and only if the sensor positions are known *a priori* to within half the wavelength of the impinging signals.

Taking the logarithm of both sides of (2.11) gives

$$\begin{aligned} d_{mn} &= \chi_m \cdot \delta_n \\ &= \frac{\log a_{mn}}{j\pi} + \lambda_{mn} \end{aligned} \tag{3.6}$$

where λ_{mn} is an even integer which takes account of phase wrapping. In [Lo92] it is shown that the $\{\lambda_{mn}\}$ are unique if *a priori* estimates of the positions of the sensors are accurate to within half the wavelength of the impinging signals. If a signal contains more than one narrowband component then replace "half the wavelength" in the previous sentence with "half the lowest common integral multiple of the wavelengths".

3.2.2.1 Two-Dimensional solution for sensor positions and signal DOAs

Theorem 4

The 2D sensor locations and signal DOAs are observable, given $\{d_{mn}\}$, if there are at least three signals and three sensors.

Restricting the array and signals to two dimensions, suppose that there is only one signal source. In this case the factorisation into sensor and signal parameters will not be unique because one signal cannot provide information about both the x- and y-directions of a sensor.

Figure 10 Given two signal-source DOAs, the sensor positions can be found as the intersection of two sets of wavefronts, which are at distances of d_{m1} and d_{m2} from the reference point.

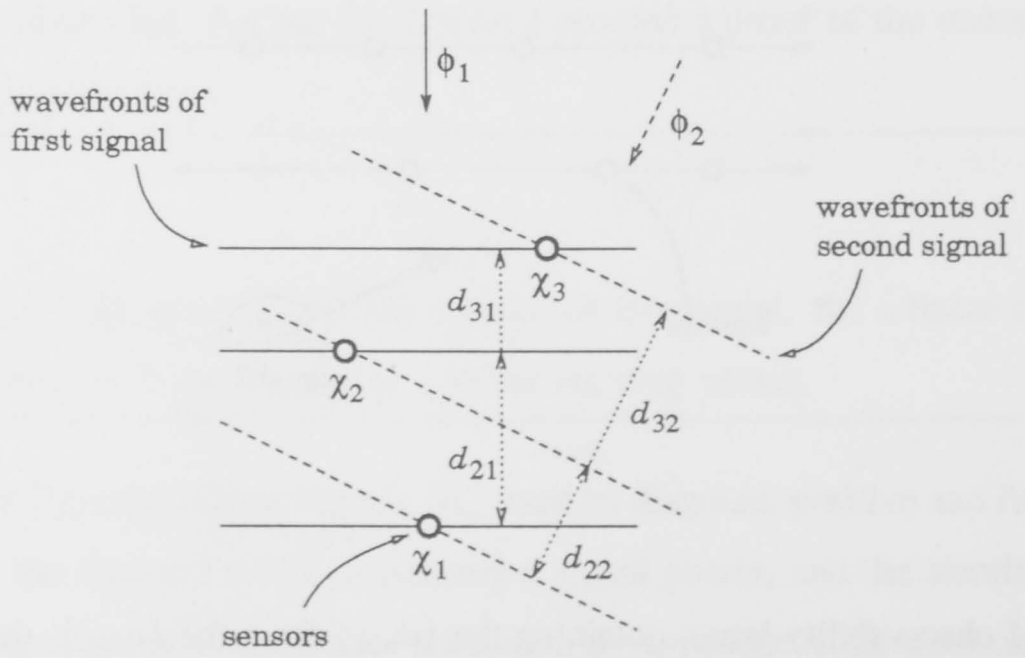

Now suppose there are two signal sources. The solution for $\{\chi_m\}$ and $\{\phi_n\}$ in (2.8) can be found as the intersection of two sets of signal wavefronts, as in Figure (10). We remove the problem of rotational ambiguity by making the first signal DOA equal to 90°. The second sensor is free to exist anywhere in the plane. The set of solid lines represents the wavefronts from the first signal, as the signal arrives at each sensor, which are defined by,

$$\{y_m = d_{m1}\}, \tag{3.7}$$

and the dashed set of parallel lines represents the wavefronts of the second signal from direction, ϕ_2. The set of lines corresponding to the second signal source is defined by,

$$\left\{y_m = \frac{-x_m}{\tan\phi_2} + \frac{d_{m2}}{\sin\phi_2}\right\}, \tag{3.8}$$

and the simultaneous solution to (3.7) and (3.8) is,

$$\begin{aligned}&\left\{x_m = \left(\frac{d_{m2}}{\sin\phi_2} - d_{m1}\right)\tan\phi_2\right\},\\ &\{y_m = d_{m1}\}.\end{aligned} \tag{3.9}$$

So, with two signal sources, we have a valid solution for $\{\chi_m\}$ and $\{\phi_n\}$ for any choice of ϕ_2, and so there is no unique solution for $\{\chi_m\}$ and $\{\phi_n\}$.

Figure 11 Basic system, with 3 signals and 3 sources. The intervals χ_1-χ_2 and χ_1-χ_3 are the diameters of circles upon which the points, at distances $\{d_{mn}\}$ from the origin in the direction of the signals, $\{\delta_n\}$, must lie.

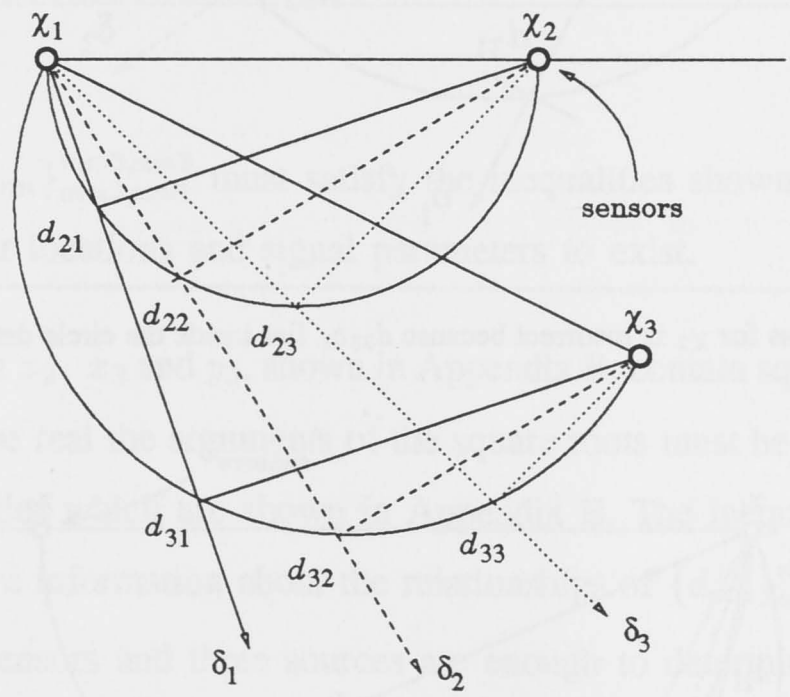

Now consider the existence of three signals impinging on an array with three sensors. The system is represented geometrically in Figure 11. The intervals χ_1-χ_2 and χ_1-χ_3 are the diameters of circles, and because the points at $\{d_{mn}\delta_n\}$ are the projections of $\{\chi_m\}$ onto $\{\delta_n\}$, the $\{d_{mn}\delta_n\}$ must lie on the associated circles. The interval χ_1-χ_2 may be no smaller than the largest of $\{d_{2n}\}$ which, in Figure 11, is d_{23}. So, when trying to determine $\{\chi_m\}$ and $\{\delta_n\}$ from

the $\{d_{mn}\}$, an initial guess for χ_1-χ_2 can be equal to the largest of $\{d_{2n}\}$. Figure 12 shows our first attempt, where χ_1-$\chi_2 = d_{23}$. The interval χ_1-χ_2 defines one circle and the direction-cosine vectors can be found from the intersection of $\{d_{2n}\delta_n\}$ with the circle. The points χ_1, $d_{31}\delta_1$, and $d_{32}\delta_2$ uniquely define the second circle, the diameter of which is the interval χ_1-χ_3. Because the point $d_{33}\delta_3$ lies outside the circle this cannot be a solution to (2.8). Our second attempt at determining $\{\chi_m\}$ and $\{\delta_n\}$ is shown in Figure 13. This time the point $d_{33}\delta_3$ lies inside the second circle so it, too, is not a solution to (2.8). The position of $d_{33}\delta_3$ will move from outside to inside the second circle as the estimate of the interval χ_1-χ_2 increases, and so $d_{33}\delta_3$ will lie on the second circle once, and only once, over the domain of χ_1-χ_2. Thus the solution for $\{\chi_m\}$ and $\{\delta_n\}$ from (2.8) is unique, and they are observable when the array is two-dimensional.

Figure 12 The first guess for χ_2 is incorrect because $d_{33}\delta_3$ lies outside the circle defined by χ_1, $d_{31}\delta_1$ and $d_{32}\delta_2$.

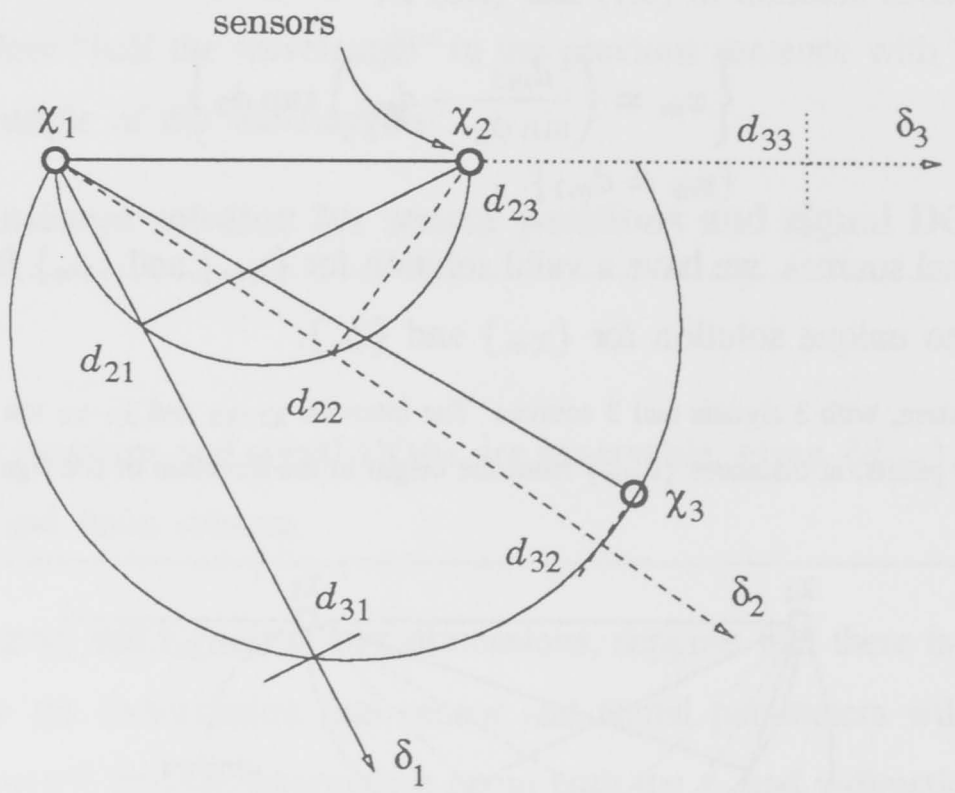

Figure 13 The second guess for χ_2 is incorrect because $d_{33}\delta_3$ lies inside the circle defined by χ_1, $d_{31}\delta_1$ and $d_{32}\delta_2$.

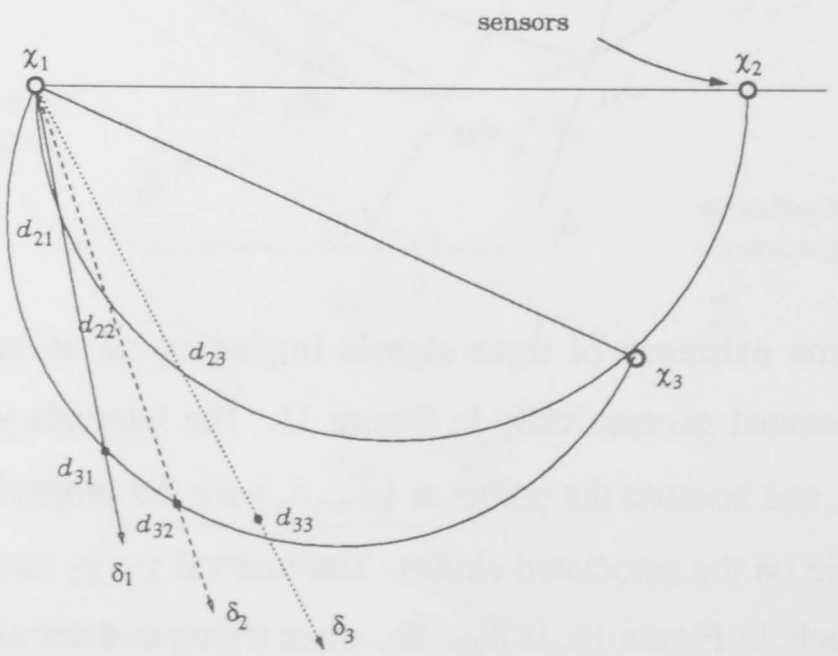

In fact, it is possible to find a closed-form solution for $\{\chi_m\}$ and $\{\delta_n\}$ as follows. A coordinate system is chosen in which the second sensor lies on the x-axis, so $y_2 = 0$ and from (2.8) we have

$$\begin{gathered}\{\cos\phi_n = d_{2n}/x_2\}_{n=1}^{3}, \\ \left\{\sin\phi_n = \frac{\pm\sqrt{x_2^2 - d_{2n}^2}}{x_2}\right\}_{n=1}^{3},\end{gathered} \tag{3.10}$$

which defines the signal DOAs in terms of the $\{d_{2n}\}$. Then

$$\left\{d_{3n} = x_3\frac{d_{2n}}{x_2} \pm y_3\frac{\sqrt{x_2^2 - d_{2n}^2}}{x_2}\right\}_{n=1}^{3}, \tag{3.11}$$

and rearranging the equation gives,

$$\begin{aligned} x_2^2\left(d_{31} - x_3\frac{d_{21}}{x_2}\right)^2 &= y_3^2(x_2^2 - d_{21}^2), \\ x_2^2\left(d_{32} - x_3\frac{d_{22}}{x_2}\right)^2 &= y_3^2(x_2^2 - d_{22}^2), \\ x_2^2\left(d_{33} - x_3\frac{d_{23}}{x_2}\right)^2 &= y_3^2(x_2^2 - d_{23}^2). \end{aligned} \tag{3.12}$$

The simultaneous solution of x_2, x_3 and y_3 in terms of $\{d_{mn}\}_{m=2,n=1}^{m=3,n=3}$, from (3.12), is shown in Appendix B. There are four sets of solutions, three of which are reflections of the first about the x- and y-axes, and which we regard as trivial. Hence, apart from translations, rotations and reflections, the factorisation of the distances $\{d_{mn}\}$ into two-dimensional sensor and signal parameters, $\{\chi_m\}$ and $\{\phi_n\}$, is unique when there are at least 3 sensors and 3 signals.

Corollary

The elements $\{d_{mn}\}_{m=2,n=1}^{m=3,n=3}$ must satisfy the inequalities shown in Appendix B for a solution for the sensor locations and signal parameters to exist.

The expressions for x_2, x_3 and y_3, shown in Appendix B, contain square-root operators, and for the expressions to be real the arguments of the square roots must be greater than zero. This results in two inequalities which are shown in Appendix B. The inequalities are cumbersome and so offer no intuitive information about the relationships of $\{d_{mn}\}_{m=2,n=1}^{m=3,n=3}$ to one another.

Given that three sensors and three sources are enough to determine the first three signal DOAs and sensor locations, we now look at the conditions placed upon $\{d_{mn}\}_{m>3,n>3}$, when there are more than three sensors or sources. First, consider the addition of an n^{th} signal source, where $n > 3$. From (3.10), ϕ_n is defined to be within one of two quadrants, so to resolve the ambiguity we use,

$$d_{3n} = x_3\frac{d_{2n}}{x_2} \pm y_3\frac{\sqrt{x_2^2 - d_{2n}^2}}{x_2} \tag{3.13}$$

which also constrains d_{3n} to having one of two values.

Now consider the addition of an m^{th} sensor, χ_m, to our basic three-sensor, three-source system. Figure 14 shows that the perpendiculars from the lines defined by the direction cosines, $\{\delta_n\}_{n=1}^{3}$, at the points defined by the distances $\{d_{mn}\}_{n=1}^{3}$, must intersect at a common point, (x_m, y_m). The first two of these perpendicular lines are defined by,

$$\begin{aligned} y_m &= \frac{-x_m}{\tan\phi_1} + \frac{d_{m1}}{\sin\phi_1}, \\ y_m &= \frac{-x_m}{\tan\phi_2} + \frac{d_{m2}}{\sin\phi_2}, \end{aligned} \tag{3.14}$$

and the simultaneous solution of these equations defines (x_m, y_m) to be,

$$\begin{aligned} x_m &= \frac{d_{m1}\sin\phi_2 - d_{m2}\sin\phi_1}{\sin(\phi_2 - \phi_1)}, \\ y_m &= \frac{d_{m2}\cos\phi_1 - d_{m1}\cos\phi_2}{\sin(\phi_2 - \phi_1)}. \end{aligned} \tag{3.15}$$

This constrains d_{m3} to be,

$$d_{m3} = \frac{d_{m1}\sin(\phi_2 - \phi_3) + d_{m2}\sin(\phi_3 - \phi_1)}{\sin(\phi_2 - \phi_1)}, \tag{3.16}$$

where the solutions for ϕ_1, ϕ_2 and ϕ_3 are shown in Section 3.2.2.1.

Figure 14 The first three sensors define the signal DOAs so that for any other sensor the perpendiculars from the lines defined by the direction cosines, $\{\delta_n\}$, at the points defined by $\{d_{mn}\}$ must intersect at a common point.

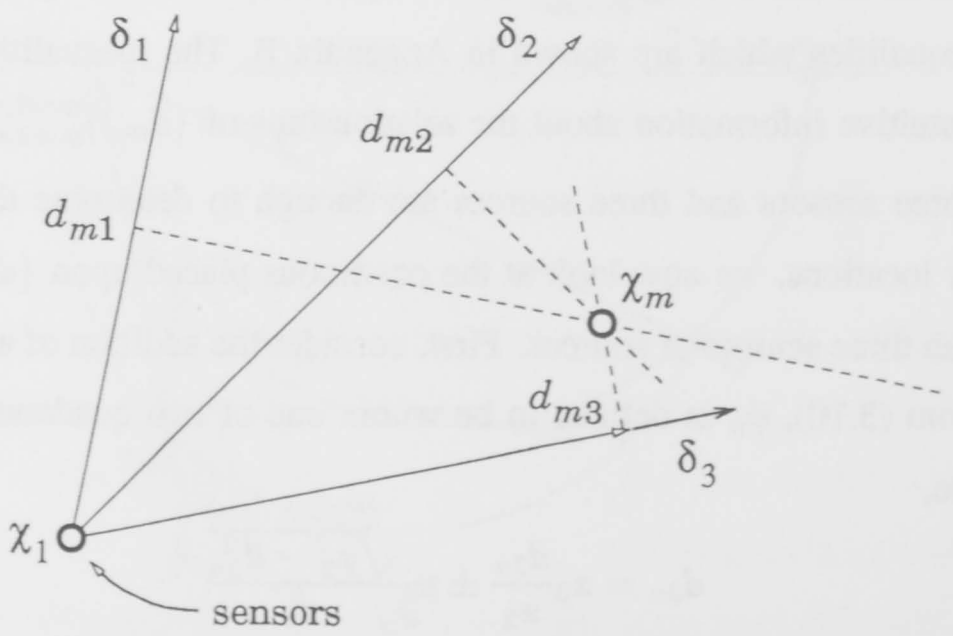

3.2.2.2 Three-dimensional solution for sensor positions and signal DOAs

When the signals and sensors are assumed to exist in a 3D space, the interval χ_1-χ_m is the diameter of a sphere upon whose surface every point $\{d_{mn}\delta_n\}$ will lie. No diagram can adequately depict this, but some thought will show that three interval lengths, instead of one for the 2D case, control the solution. In this case we must resort to algebra. From (2.8), and using matrix notation,

$$\mathbf{D} = \mathrm{X}\Delta, \tag{3.17}$$

where $\mathbf{D}$ is composed of the elements $\{d_{mn}\}$, $\mathrm{X} = [\chi_1, \chi_2, \ldots, \chi_M]^{\mathrm{T}}$ and $\Delta = [\delta_1, \delta_2, \ldots, \delta_N]$.

Lemma 1

The rank of $\mathbf{D}$ is 2 for the 2D case and 3 for the 3D case.

If the array and signal sources lie in a plane, if the array is not linear and if there are two or more signals with differing DOAs then both X and Δ will be rank 2 and so $\mathbf{D}$, being the product of X and Δ as in (3.17), will also be rank 2. In the 3D case, if the array is not planar, and if there are three or more signals with DOAs that are not coplanar, then X and Δ, and hence $\mathbf{D}$, will be rank 3.

As a starting point, if the number of known quantities is compared with the number of unknown quantities, we can obtain a lower bound on the numbers of sensors and signals for their parameters to be observable.

Lemma 2

A lower bound on the numbers of signals and sensors required for their parameters to be observable, given $\{d_{mn}\}$, is six and four, respectively.

From lemma 1, three columns of $\mathbf{D}$ will be independent, while the remaining columns provide only three independent pieces of information, namely, the linear multipliers that define those columns. And so the number of known quantities in $\mathbf{D}$ is given by $3(M-1) + 3(N-3)$, $N \geq 3$, where $M-1$ is used instead of M because the reference sensor (the first one) does not provide any information, i.e. $d_{1n} = 0$, $\forall\, n$. The number of unknown sensor parameters, $\{\chi_m = (x_m, y_m, z_m)\}$, is $3(M-1)$, and the number of unknown signal parameters, $\{\phi_n, \theta_n\}$, is $2N$. Therefore the total number of unknown quantities is $3(M-1) + 2N - 3$, where the -3 is the result of selecting a set of axes in which either two signals or three sensors are aligned with an axis and the plane of two axes. Requiring that the number of knowns equals

or exceeds the number of unknowns, we have

$$\begin{aligned} 3M + 3N - 12 &\geq 3M + 2N - 6, \\ N &\geq 6, \end{aligned} \tag{3.18}$$

and the minimum number of signals required is six when the equality is true. At least three non-zero rows are required in $\mathbf{D}$ to determine the linear multipliers that specify columns of $\mathbf{D}$ beyond the third. The first row of $\mathbf{D}$ contains only zeros, so there must be at least four rows, and hence four sensors.

Theorem 5

The 3D sensor locations and signal DOAs are observable, given $\{d_{mn}\}$, if there are at least four sensors and six signals.

To prove this I provide a closed-form solution for the sensor locations and signal DOAs from the $\mathbf{D}$ matrix. I choose a coordinate system, in which the first signal is in the direction of the positive x-axis and the second signal lies in the xy-plane, and so the direction cosine vectors are,

$$\begin{aligned} \delta_1 &= (1, 0, 0), \\ \delta_2 &= \left(a_2, \pm\sqrt{1 - a_2^2}, 0\right), \\ \delta_n &= \left(a_n, b_n, \pm\sqrt{1 - a_n^2 - b_n^2}\right), \quad n > 2, \end{aligned} \tag{3.19}$$

where $a_n = \cos\phi_n \cos\theta_n$, and $b_n = \sin\phi_n \cos\theta_n$. Let the linear multipliers for the n^{th} signal, $(n \geq 4)$, be μ_{1n}, μ_{2n}, and μ_{3n}, so that

$$\mu_{1n} d_{m1} + \mu_{2n} d_{m2} + \mu_{3n} d_{m3} = d_{mn}, \; n \geq 4, \tag{3.20}$$

and, combining this with (2.8),

$$\begin{aligned} \mu_{1n}\chi_m\delta_1 + \mu_{2n}\chi_m\delta_2 + \mu_{3n}\chi_m\delta_3 &= \chi_m\delta_n \\ (\mu_{1n}\delta_1 + \mu_{2n}\delta_2 + \mu_{3n}\delta_3 - \delta_n)\cdot\chi_m &= 0 \\ \Delta\mu\cdot\chi_m &= 0, \quad n \geq 4, \end{aligned} \tag{3.21}$$

where $\mu = [\mu_{1n}, \mu_{2n}, \mu_{3n}, -1]^T$ is a basis for the null space of

$$\begin{bmatrix} d_{21} & \cdots & d_{23} & d_{2n} \\ \vdots & \ddots & \vdots & \vdots \\ d_{M1} & \cdots & d_{M3} & d_{Mn} \end{bmatrix}. \tag{3.22}$$

This tells us that either χ_m is orthogonal to $\Delta\mu$, or $\Delta\mu = \mathbf{0}$. The first possibility can happen only in the degenerate system where all of the sensors exist in a plane or a line. Because we

are dealing specifically with 3D systems, we assume that this is not the case, so the second possibility must be true. Substituting (3.19) into (3.21) gives,

$$\begin{aligned} \mu_{1n} + \mu_{2n}a_2 + \mu_{3n}a_3 - a_n &= 0 \\ \mu_{2n}\sqrt{1-a_2^2} + \mu_{3n}b_3 - b_n &= 0 \\ \mu_{3n}\sqrt{1-a_3^2-b_3^2} - \sqrt{1-a_n^2-b_n^2} &= 0, \quad n \geq 4. \end{aligned} \tag{3.23}$$

The origin and the three points, $d_{m1}\delta_1$, $d_{m2}\delta_2$ and $d_{m3}\delta_3$, uniquely define a sphere on which surface they lie. The interval χ_1-χ_m is its diameter. The equation that defines the sphere is,

$$(x-\alpha)^2 + (y-\beta)^2 + (z-\gamma)^2 = r^2, \tag{3.24}$$

where

$$\begin{aligned} \alpha &= d_{m1}/2, \\ \beta &= \frac{d_{m2} - d_{m1}a_2}{2\sqrt{1-a_2^2}}, \\ \gamma &= \frac{(d_{m3} - d_{m1}a_3)\sqrt{1-a_2^2} + d_{m1}a_2b_3 - d_{m2}b_3}{2\sqrt{1-a_3^2-b_3^2}\sqrt{1-a_2^2}}, \text{ and} \\ r^2 &= \alpha^2 + \beta^2 + \gamma^2. \end{aligned} \tag{3.25}$$

The point $d_{mn}\delta_n$, where $n \geq 4$, must also lie on this sphere, and the equation that results when $d_{mn}\delta_n$ is substituted for (x, y, z) in (3.24) is,

$$\begin{aligned} &d_{m1}\left[\sqrt{1-a_2^2}\left(b_4(a_3^2+b_3^2-1) + b_3\sqrt{1-a_4^2-b_4^2}\sqrt{1-a_3^2-b_3^2}\right)a_2 + \right. \\ &\left.(a_2^2-1)(a_3^2+b_3^2-1)a_4 + \sqrt{1-a_4^2-b_4^2}\sqrt{1-a_3^2-b_3^2}(a_2^2-1)a_3\right] - \\ &d_{m2}\sqrt{1-a_2^2}\left[b_4(a_3^2+b_3^2-1) + b_3\sqrt{1-a_4^2-b_4^2}\sqrt{1-a_3^2-b_3^2}\right] - \\ &d_{m3}\sqrt{1-a_4^2-b_4^2}\sqrt{1-a_3^2-b_3^2}(a_2^2-1) - \\ &d_{mn}(a_2^2-1)(a_3^2+b_3^2-1) = 0. \end{aligned} \tag{3.26}$$

There are three of these equations, one for each of the sensors from two to four. These equations are linear in $\{d_{mn}\}$, and so they can be represented in matrix form by,

$$\begin{bmatrix} d_{21} & d_{22} & d_{23} & d_{2n} \\ d_{31} & d_{32} & d_{33} & d_{3n} \\ d_{41} & d_{42} & d_{43} & d_{4n} \end{bmatrix} \begin{bmatrix} f_1 \\ f_2 \\ f_3 \\ f_4 \end{bmatrix} = \begin{bmatrix} 0 \\ 0 \\ 0 \\ 0 \end{bmatrix}, \tag{3.27}$$

$$\mathbf{Df} = 0,$$

where $\mathbf{f} = [f_1, f_2, f_3, f_4]^T$, and from (3.26),

$$\begin{aligned} f_1 =& \sqrt{1-a_2^2}\left(b_4(a_3^2+b_3^2-1) + b_3\sqrt{1-a_4^2-b_4^2}\sqrt{1-a_3^2-b_3^2}\right)a_2 + \\ & (a_2^2-1)(a_3^2+b_3^2-1)a_4 + \sqrt{1-a_4^2-b_4^2}\sqrt{1-a_3^2-b_3^2}(a_2^2-1)a_3, \\ f_2 =& -\sqrt{1-a_2^2}\left[b_4(a_3^2+b_3^2-1) + b_3\sqrt{1-a_4^2-b_4^2}\sqrt{1-a_3^2-b_3^2}\right], \\ f_3 =& \sqrt{1-a_4^2-b_4^2}\sqrt{1-a_3^2-b_3^2}(1-a_2^2), \\ f_4 =& (1-a_2^2)(a_3^2+b_3^2-1). \end{aligned} \tag{3.28}$$

And so, from (3.27), the vector, $\mathbf{f}$, lies in the null space, $\lambda\mu$, of the matrix $\mathbf{D}$, where λ is an unknown scalar. Thus,

$$\begin{bmatrix} f_1 \\ f_2 \\ f_3 \\ f_4 \end{bmatrix} = \lambda \begin{bmatrix} \mu_{1n} \\ \mu_{2n} \\ \mu_{3n} \\ -1 \end{bmatrix}. \tag{3.29}$$

Combining the (dependent) equations in (3.23) with (3.29), a solution can be found for a_3, a_4, b_4 and λ in terms of the parameters a_2 and b_3,

$$\begin{aligned} a_3 &= \frac{-2\mu_{2n}\mu_{3n}b_3\sqrt{1-a_2^2} - \mu_{1n}^2 - 2\mu_{1n}\mu_{2n}a_2 - \mu_{2n}^2 - \mu_{3n}^2 + 1}{2\mu_{3n}(\mu_{1n} + \mu_{2n}a_2)}, \\ a_4 &= \frac{-2\mu_{2n}\mu_{3n}b_3\sqrt{1-a_2^2} + \mu_{1n}^2 + 2\mu_{1n}\mu_{2n}a_2 + 2\mu_{2n}^2a_2^2 - \mu_{2n}^2 - \mu_{3n}^2 + 1}{2(\mu_{1n} + \mu_{2n}a_2)}, \\ b_4 &= \mu_{2n}\sqrt{1-a_2^2} + \mu_{3n}b_3. \end{aligned} \tag{3.30}$$

The value for λ is unimportant, aside from the fact that it is unique, and has not been given here. There are seven more parameterised solutions, other than that in (3.30), which are reflections of each other through the x-, y- and z-axes, and which we regard as trivial duplications of the one solution. From (3.30), and using $4 \leq n \leq 6$, we have three simultaneous equations

$$\begin{aligned} a_3 &= \frac{-2\mu_{24}\mu_{34}b_3\sqrt{1-a_2^2} - \mu_{14}^2 - 2\mu_{14}\mu_{24}a_2 - \mu_{24}^2 - \mu_{34}^2 + 1}{2\mu_{34}(\mu_{14} + \mu_{24}a_2)}, \\ a_3 &= \frac{-2\mu_{25}\mu_{35}b_3\sqrt{1-a_2^2} - \mu_{15}^2 - 2\mu_{15}\mu_{25}a_2 - \mu_{25}^2 - \mu_{35}^2 + 1}{2\mu_{35}(\mu_{15} + \mu_{25}a_2)}, \\ a_3 &= \frac{-2\mu_{26}\mu_{36}b_3\sqrt{1-a_2^2} - \mu_{16}^2 - 2\mu_{16}\mu_{26}a_2 - \mu_{26}^2 - \mu_{36}^2 + 1}{2\mu_{36}(\mu_{16} + \mu_{26}a_2)}, \end{aligned} \tag{3.31}$$

and solving for a_2 and b_3 we obtain

$$a_2 = \frac{\begin{array}{c}[\mu_{34}\mu_{36}(\mu_{14}\mu_{26} - \mu_{16}\mu_{24})(\mu_{15}^2 + \mu_{25}^2 + \mu_{35}^2 - 1) \\ +\mu_{34}\mu_{35}(\mu_{15}\mu_{24} - \mu_{14}\mu_{25})(\mu_{16}^2 + \mu_{26}^2 + \mu_{36}^2 - 1) \\ +\mu_{35}\mu_{36}(\mu_{16}\mu_{25} - \mu_{15}\mu_{26})(\mu_{14}^2 + \mu_{24}^2 + \mu_{34}^2 - 1)]\end{array}}{\begin{array}{c}2[\mu_{14}\mu_{24}\mu_{35}\mu_{36}(\mu_{15}\mu_{26} - \mu_{16}\mu_{25}) + \mu_{16}\mu_{26}\mu_{34}\mu_{35}(\mu_{14}\mu_{25} - \mu_{15}\mu_{24}) \\ +\mu_{15}\mu_{25}\mu_{34}\mu_{36}(\mu_{16}\mu_{24} - \mu_{14}\mu_{26})]\end{array}}, \tag{3.32}$$

$$b_3 = \frac{\begin{array}{c}[(\mu_{15}\mu_{35} + \mu_{25}\mu_{35}a_2)(\mu_{14}^2 + 2\mu_{14}\mu_{24}a_2 + \mu_{24}^2 + \mu_{34}^2 - 1) \\ -(\mu_{14}\mu_{34} + \mu_{24}\mu_{34}a_2)(\mu_{15}^2 + 2\mu_{15}\mu_{25}a_2 + \mu_{25}^2 + \mu_{35}^2 - 1)]\end{array}}{2\mu_{34}\mu_{35}\sqrt{1-a_2^2}(\mu_{14}\mu_{25} - \mu_{15}\mu_{24})}. \tag{3.33}$$

Therefore, disregarding translations, rotations and reflections, the sensor locations and signal directions are observable, given $\{d_{mn}\}$, when the system has at least four sensors and six signals.

3.2.2.3 Summary of Sections 3.2.2.1 and 3.2.2.2

The four observability theorems discussed in this section are separate from one another in the sense that the existence of the conditions for theorem 2 does not imply existence of the conditions for theorems 3,4 or 5. Sections 3.2.2.1 and 3.2.2.2 require minimum systems of three sensors and three signals, and four sensors and six signals, in the 2D and 3D cases respectively. However, considering the observability of the noise (Section 3.2.1) there must be more sensors than signals for the sensor and signal parameters to be observable from the array-covariance matrix. Therefore, there must be a minimum of four and seven sensors for the 2D and 3D cases, respectively.

3.2.3 Observability of signal and sensor parameters when the signals are coherent and there is one signal source.

This section and the next deal with systems that have coherent signals. I start by introducing the extra notation to handle coherent signals, and then proceed on the assumption that there is only one source of all the signals. I assume there is more than one signal source in Section 3.2.4.

Suppose that some of the signals arriving at the array are reflections of other signals. All of the signals that originate from the one source will be coherent. Let the complex amplitudes of the κ^{th} signal group be $\mathbf{s}_\kappa = [s_{1\kappa}, s_{2\kappa}, \ldots, s_{\Gamma_\kappa\kappa}]^{\text{T}}$, where Γ_κ is the number of reflected and direct signals impinging upon the array, from the κ^{th} signal source. The form of the signal-covariance matrix, $\mathbf{R}_s$ will no longer be diagonal but, instead, will be block diagonal,

$$\mathbf{R}_s = \text{diag}\left[\mathbf{s}_1\mathbf{s}_1^{\text{H}}, \mathbf{s}_2\mathbf{s}_2^{\text{H}}, \ldots, \mathbf{s}_{\text{K}}\mathbf{s}_{\text{K}}^{\text{H}}\right], \tag{3.34}$$

where K is the number of signal sources, as opposed to the number of signals, N, which is given by $N = \sum_{\kappa=1}^{\text{K}} \Gamma_\kappa$. Each of the blocks, $\left\{\mathbf{s}_\kappa\mathbf{s}_\kappa^{\text{H}}\right\}$, in the signal-covariance matrix is rank 1 because $\mathbf{s}_\kappa$ is a vector, and so the rank of the signal-covariance matrix, $\mathbf{R}_s$, and of the noiseless covariance matrix, $\mathbf{R}_a = \mathbf{A}\mathbf{R}_s\mathbf{A}^{\text{H}}$, is K. If we write

$$\Sigma = \begin{bmatrix} s_1 & \mathbf{0} & \mathbf{0} & \mathbf{0} \\ \mathbf{0} & s_2 & \mathbf{0} & \vdots \\ \vdots & \vdots & \ddots & \mathbf{0} \\ \mathbf{0} & \mathbf{0} & \mathbf{0} & s_{\text{K}} \end{bmatrix}, \tag{3.35}$$

then the signal-covariance matrix is given by,

$$\mathbf{R}_s = \Sigma\Sigma^H. \tag{3.36}$$

The noiseless covariance matrix, $\mathbf{R}_a$, can be factorised in the form,

$$\mathbf{R}_a = \mathbf{B}\mathbf{B}^{\text{H}}, \tag{3.37}$$

where $\mathbf{B}$, which is of rank K, is given by

$$\mathbf{B} = \mathbf{A}\Sigma. \tag{3.38}$$

The column vectors, $\{\mathbf{b}_\kappa\}$, of $\mathbf{B}$, are linear combinations of steering vectors, and so if $\Gamma_\kappa > 1$, $\mathbf{b}_\kappa$, in general, will not be a steering vector. Indeed, when factorising $\mathbf{R}_a$, without any prior information about the signals, it cannot be assumed that any of the vectors in $\mathbf{B}$ are steering vectors. Further, we can discover only the number of signal sources, K, being equal to the rank of $\mathbf{R}_a$, and have no prior information about the total number of impinging signals, N. For the same reasons as in Section 3.2.2, all solutions for $\mathbf{B}$ in (3.37) must be linear combinations of one another. So, given that there must be at least one solution, say $\mathbf{B}\mathbf{B}^{\mathrm{H}}$, another possible solution, $\mathbf{C}$, is given by, $\mathbf{C} = \mathbf{B}\mathbf{U}$, where $\mathbf{U}$ is a K $\times$ K matrix. Then,

$$\begin{aligned} \mathbf{R}_a &= \mathbf{B}\mathbf{B}^{\mathrm{H}} \\ &= \mathbf{C}\mathbf{U}^{-1}\mathbf{U}^{-\mathrm{H}}\mathbf{C}^{\mathrm{H}}, \end{aligned} \tag{3.39}$$

and, if $\mathbf{U}$ is unitary, then $\mathbf{R}_a = \mathbf{C}\mathbf{C}^{\mathrm{H}}$ is another possible factorisation. Thus, any rotation of one solution for B is also a solution. Given one possible solution, $\mathbf{B}$, to (3.37), the steering vectors must be determined from the equation,

$$\mathbf{b}_\kappa = \sum_{n=1}^{\Gamma_\kappa} \mathbf{a}_{(\gamma_\kappa+n)} s_{n\kappa}, \tag{3.40}$$

where $\mathbf{a}_{(\gamma_\kappa+n)}$ is the $(\gamma_\kappa + n)^{\mathrm{th}}$ steering vector of $\mathbf{A}$, $\gamma_\kappa = \sum_{n=0}^{\kappa-1} \Gamma_n$, $\Gamma_0 = 0$, and $\mathbf{b}_\kappa$ is the κ^{th} vector of $\mathbf{B}$. If $\mathbf{s}_\kappa$ is ordered so that $|s_{1\kappa}| \geq |s_{2\kappa}| \geq \ldots \geq |s_{\Gamma_\kappa\kappa}|$, then, from the triangle inequality we know that

$$\begin{aligned} \sum_{p=\mu}^{\Gamma_\kappa} |s_{p\kappa}| &\geq \max_m \left\{ \left| b_{m\kappa} - \sum_{q=1}^{\mu-1} a_{(\gamma_\kappa+q)} s_{q\kappa} \right| \right\}, \\ |s_{\mu\kappa}| - \sum_{p=\mu+1}^{\Gamma_\kappa} |s_{p\kappa}| &\leq \min_m \left\{ \left| b_{m\kappa} - \sum_{q=1}^{\mu-1} a_{(\gamma_\kappa+q)} s_{q\kappa} \right| \right\}, \quad 1 \leq \mu \leq \Gamma_\kappa. \end{aligned} \tag{3.41}$$

As is typical when using algebra to describe geometry, this is a tedious way of requiring that Γ_κ line segments with lengths $\{|s_{n\kappa}|\}_{n=1}^{\Gamma_\kappa}$, be able to span the distance from the origin to all of M points in a plane (the Argand diagram), when arranged end to end at various angles. Equation (3.41) obviously has an infinite number of solutions, as does (3.40), and so if we are to determine whether the sensor and signal parameters are observable, we must know whether the constraint that all the steering vectors conform to a common system of sensors and signals is enough to restrict the number of possible factorisations.

Definition

Two systems with equal numbers of sensors, that have different array shapes and/or different signal powers and DOAs, are **isocovariant** if their respective noiseless array covariance matrices are identical.

Theorem 6

If an array receives signals that are coherent and there is only one signal source, it will be isocovariant with an infinite number of other systems.

This theorem is proven by demonstrating an algorithm that can estimate an infinite number of systems from the one array-covariance matrix, when there is one signal source with multipath propagation. For the remainder of this section, suppose that only one signal source exists, and assume, for the purposes of our decomposition, that the direct signal, plus two reflections, impinge upon the array. The noiseless array-covariance matrix, $\mathbf{R}_a$, is rank 1, and can be factorised into, $\mathbf{R}_a = \mathbf{b}\mathbf{b}^{\mathrm{H}}$, which is unique because the only unitary 1×1 matrix is the identity matrix. From (3.40), we have,

$$b_m = a_{m1}s_1 + a_{m2}s_2 + a_{m3}s_3 \tag{3.42}$$

where m is the sensor number, and the subscript κ has been dropped because there is only one signal source. Because the $\{a_{mn}\}$ are complex, if the $\{s_n\}$ are given, then choosing a value for a_{m1} will determine the values for a_{m2} and a_{m3} to be one of two possible solutions. This can be seen as the intersection of two circles of radii $|s_2|$ and $|s_3|$, in Figure 15

Figure 15 Given a_{m1} and $\{s_n\}$, then a_{m2} and a_{m3} can be found from the intersection of two circles with radii $|s_2|$ and $|s_3|$.

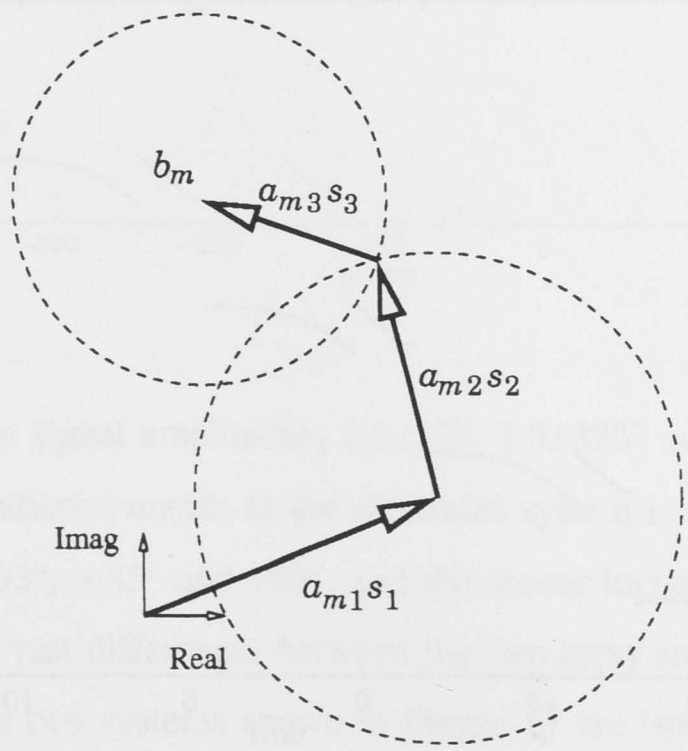

For a 2D system, Section 3.2.2 and Section 3.2.2.1 show that steering vector information from only the first three sensors and signals fully determines the locations of those sensors as well as the signal DOAs. Therefore, the $\{s_n\}$ may be selected in a random fashion, while respecting the constraints of (3.41). In practice, the constraints on $\{d_{mn}\}_{m=2,n=1}^{m=3,n=3}$, established in Appendix A are loose enough that (3.40) can be solved for random d_{21} and d_{31}, and the constraints in Appendix A will be met in about 50% of all cases. If the constraints in Appendix A are not met, simply by tweaking the value of either d_{21} or d_{31}, and correspondingly recalculating d_{m2} and d_{m3}, the constraints can be satisfied.

Having proceeded this far, $\{\delta_n\}_1^3$ and $\{\chi_m\}_1^3$ can be calculated using the closed-form expression of Appendix B, then we can simultaneously solve (3.40) and (3.16) to obtain solutions for $\{\chi_m\}_4^M$. Because $a_{mn} = \exp(j\pi d_{mn})$, the simultaneous equations are complicated by the inclusion of the transcendental terms, and no explicit solution for $\{\chi_m\}_4^M$ can be found.

Instead, a numerical zero-finding algorithm is applied to

$$f(d_{m1}) = d_{m3} - \frac{d_{m1}(\cos\phi_3 \sin\phi_2 - \cos\phi_2 \sin\phi_3) + d_{m2}(\cos\phi_1 \sin\phi_3 - \cos\phi_3 \sin\phi_1)}{\cos\phi_1 \sin\phi_2 - \cos\phi_2 \sin\phi_1}, \qquad (3.43)$$

which is a rearrangement of (3.16). Given d_{m1}, (3.40) can be used to calculate values for d_{m2} and d_{m3}, which are in the range -1 to 1. A typical plot of $f(d_{m1})$ versus d_{m1} is shown in Figure 16. The discontinuities are the result of phase wrapping of πd_{m2} and πd_{m3}. If multiples of 2 are added to the values for d_{m2} and d_{m3}, $f(d_{m1})$ will be shifted vertically, either up or down. The zero-finding algorithm calculates the function, $f(d_{m1})$, a number of times, using a range of multiples of 2 added to d_{m2} and d_{m3}. A zero is searched for in the region around the particular multiples of 2 that begin with a value for $f(d_{m1})$ closest to zero. Any number of zeros may be found using different additive multiples of 2.

Figure 16 Plot of typical function $f(d_{m1})$.

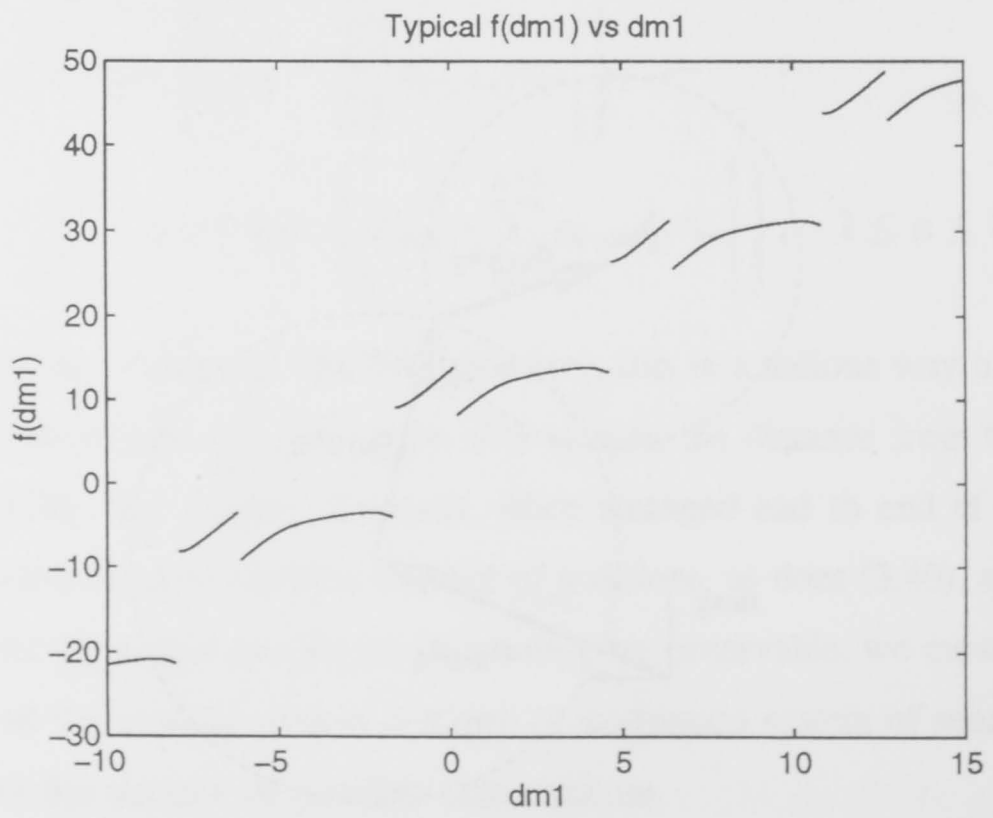

The algorithm presented can be used on any system that has only one signal source. Regardless of the number of signals in the real system, the algorithm will always find an infinite number of isocovariant systems with three signals. Clearly, a one-signal source system does not have a unique array-covariance matrix. The algorithm can be adapted to estimate a system with more than three versions of the signal source impinging upon the array, but, for the purpose of proving whether the array-covariance matrix is unique or not, this is not necessary.

Simulation studies were done to verify theorem 6. The simulated system comprised a 40-element array, in the shape shown by the solid line in Figure 17, with four coherent signals of amplitudes, $1\angle 0°$, $0.8\angle 30°$, $0.8\angle 300°$ and $0.7\angle 45°$, where $x\angle y°$ is a signal with amplitude x and relative phase $y°$. The signals' respective DOAs were 90°, 70°, 140° and $-50°$, measured anti clockwise from the x-axis. The speed of the signals in the propagating medium is 500 s^{-1} and the centre frequency of the signals is 250 Hz. Noise is assumed to be spatially uncorrelated. The noiseless array-covariance matrix is calculated using (2.8), (2.11), (3.36) and (3.5).

Figure 17 Two equivalent systems have array shapes shown by the solid line and the circles, respectively.

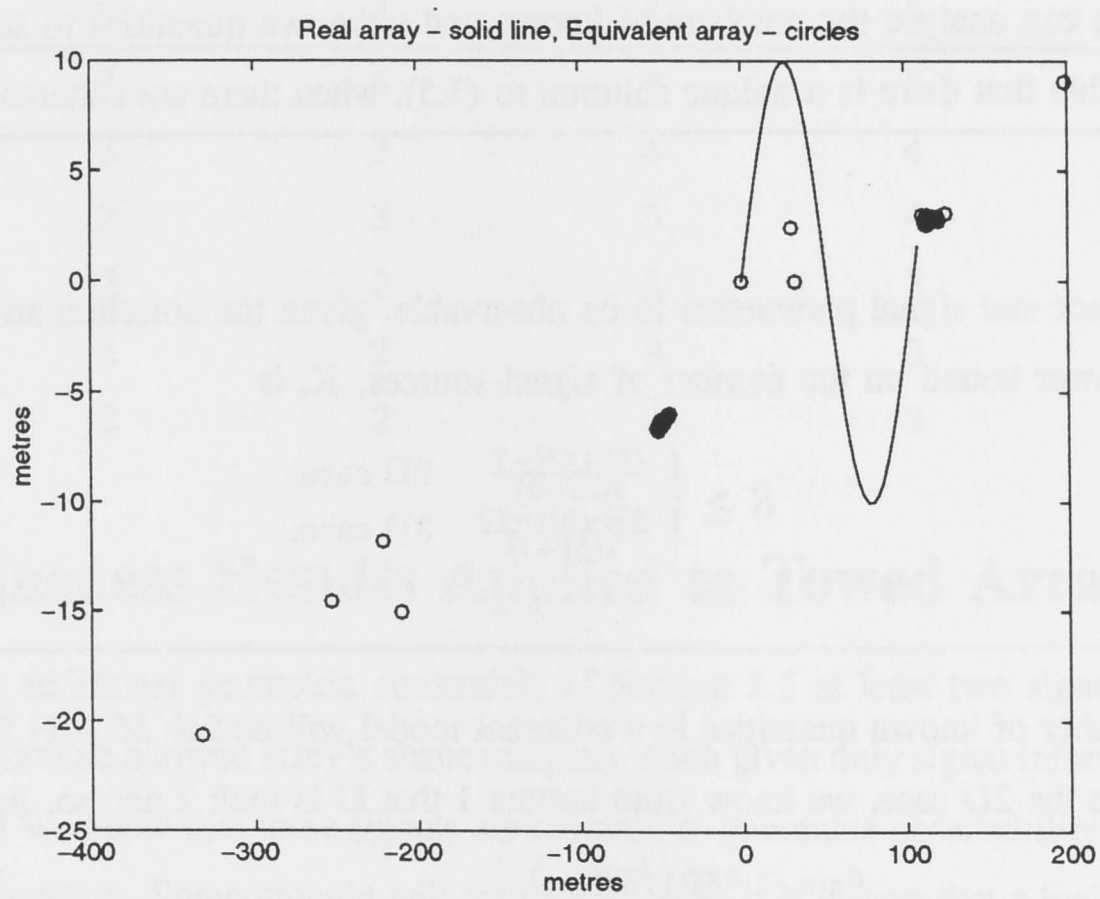

With randomly chosen signal amplitudes, $2.9\angle 17°$, $3.0\angle 325°$ and $2.8\angle 163°$, a system that has an identical array-covariance matrix to the simulated system is depicted in Figure 17. The three signal DOAs are $-93°$, $-85°$ and +93°, and the sensor locations are represented by the small circles. Despite the vast differences between the two array shapes, and the difference in the number of signals, the two systems shown in Figure 17 are isocovariant.

3.2.4 Observability of signal and sensor parameters when the signals are coherent and there is more than one signal source.

Continuing from the results of the previous section, suppose that the 2D system includes a κ^{th} signal source with its associated reflections. Given that the first signal source has allowed us to determine the (non-unique) sensor positions, all steering vectors associated with the κ^{th} signal source must be appropriate for that array shape. The equations that govern the unknown variables, $\{s_{n\kappa}, \phi_n, \Gamma_\kappa\}$, are given by (3.40), and (2.8). Using $x_m = |\chi_m| \cos(\angle\chi_m)$, and $y_m = |\chi_m| \sin(\angle\chi_m)$, where $|\chi_m|$ and $\angle\chi_m$ are the distance from the origin, and the angle from the positive x-axis, to the m^{th} sensor, respectively, and breaking (3.40) into two real equations, we have the following system of simultaneous equations:

$$\begin{aligned} d_{mn} &= |\chi_m| \cos(\phi_n - \angle\chi_m), \\ \Re\text{e}\{b_{m\kappa}\} &= \sum_{\gamma=1}^{\Gamma_\kappa} |s_{\gamma\kappa}| \cos(\angle s_{\gamma\kappa} + \pi d_{m\gamma}), \\ \Im\text{m}\{b_{m\kappa}\} &= \sum_{\gamma=1}^{\Gamma_\kappa} |s_{\gamma\kappa}| \sin(\angle s_{\gamma\kappa} + \pi d_{m\gamma}). \end{aligned} \tag{3.44}$$

No solution to (3.44) could be found (unique or otherwise) due to the transcendental terms. However, we can analyse the numbers of known and unknown quantities to see whether it is at least possible that there is a unique solution to (3.5), when there are coherent signals.

Lemma 3

For the sensor and signal parameters to be observable, given the noiseless array-covariance matrix, a lower bound on the number of signal sources, K, is

$$\text{K} \geq \begin{cases} \frac{2M+4N-7}{2(M-2)} & \text{2D case} \\ \frac{3M+5N-13}{2(M-2)} & \text{3D case.} \end{cases} \tag{3.45}$$

The number of known quantities in a coherent model will be $2\text{K}(M-1)$ for the complex matrix, B. In the 2D case, we know from lemma 1 that D is rank 2 and so, from (3.20)

$$\begin{aligned} a_{mn} &= \exp(j\pi d_{mn}) \\ &= \exp(j\pi\mu_{1n} d_{m1}) \exp(j\pi\mu_{2n} d_{m2}) \\ &= (a_{m1})^{\mu_{1n}} (a_{m2})^{\mu_{2n}}, \ \forall\ n > 2. \end{aligned} \tag{3.46}$$

The number of unknown quantities consists of $2(M-1)$ for the first two signals in the matrix D, $2(N-2)$ for the linear multipliers $\{\mu_{1n}, \mu_{2n}\}$ of the remaining signals, $2N$ for the complex signal amplitudes $\{s_{n\kappa}\}$, K for the number of signals arriving at the array from each signal source,$\{\Gamma_\kappa\}$ and $\text{K}-1$ for the rotation angles that define the unitary matrix U in (3.39). Thus

the total number of unknowns is $2M + 4N + 2\mathrm{K} - 7$, so for the number of known quantities to be greater than the number of unknown quantities,

$$\mathrm{K} \geq \frac{2M + 4N - 7}{2(M - 2)}. \tag{3.47}$$

By definition, $N \geq \mathrm{K}$, so the inequality of (3.47) is met under the conditions tabulated in Table 1. For example, if there are 5 sensors and 3 signals, there must be at least 3 signal sources, and because $\mathrm{K} = N$ then, despite the assumption to the contrary, the signals must be incoherent.

If the 3D model is assumed then the total number of unknowns is $3M + 5N + 2\mathrm{K} - 13$ and the inequality that must be satisfied is

$$\mathrm{K} \geq \frac{3M + 5N - 13}{2(M - 2)}. \tag{3.48}$$

Table 1 A lower bound on the minimum number of signal sources required for a 2D system with M sensors and N signals to have a unique array-covariance matrix.

Sensors,	Number of Signals, N				
M	3	4	5	6	7
5	3	4	4	5	6
6	3	3	4	4	5
7	2	3	3	4	4
8	2	2	3	3	4
9	2	2	3	3	3
10	2	2	3	3	3

3.3 Uniqueness Results Applied to Towed Arrays

Given the additional geometric constraints of Section 2.5 at least two signal sources are required to determine a towed array's shape uniquely when given only signal information. From Section 3.2.2.1 we know that three signals are required to guarantee observability of the sensor and signal parameters. Some thought will reveal that when it is known that a hydrophone must lie on a circle of radius ρ less than three signals are required to guarantee observability. But is it one signal or two? If there is one signal then as explained in Section 2.5 there will be a twin ambiguity with regard to the position of each hydrophone. And so, a second signal is required to resolve the ambiguity.

In Section 2.5 the twin ambiguity was resolved not by using a second signal but by assuming the solution closest to the x-axis is the correct one. If the slope of the array in the y-direction

with respect to the x-direction is small, then the twin-ambiguity assumption will be correct most of the time. From Figure 18(a), if the signal DOA angle is greater than the angle between the baseline of two sensors and the x-axis then the twin-ambiguity assumption will be correct. In Figure 18(b) it can be seen that if the signal DOA angle is less than the angle between the baseline of two sensors and the x-axis then the twin-ambiguity assumption will be incorrect. If the slopes of the baselines are small then the chance of a calibrating-signal DOA angle being less than the angle of the baseline will also be small.

Figure 18 Resolving the twin ambiguity when (a) signal DOA is greater than the angle of the baseline and (b) signal DOA is less than the angle of the baseline.

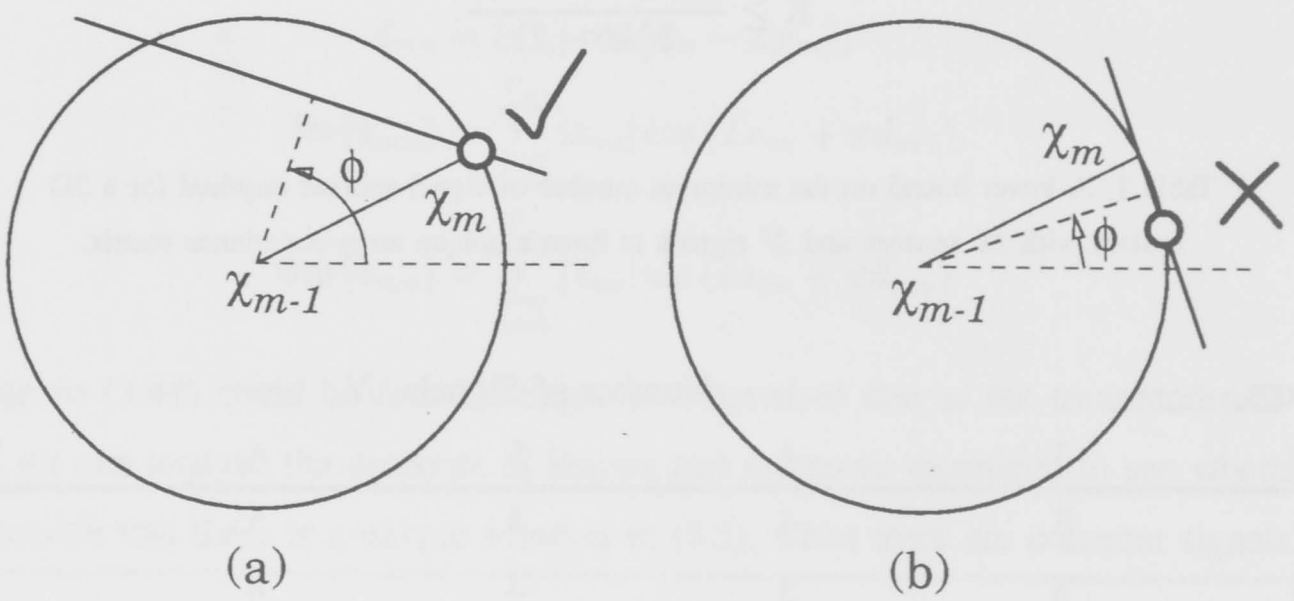

3.4 Summary of Chapter 3

Sensor locations, signal DOAs, powers and cross-powers and noise power are observable, given the array-covariance matrix, under the following conditions:

1. noise is spatially uncorrelated with equal power at every sensor,
2. signals are incoherent,
3. there are at least three signals for a 2D array and six signals for a 3D array, and
4. there are more sensors than signals.

The factorisation of the array-covariance matrix will not be unique under the following conditions:

1. when noise is spatially correlated,
2. when signals are coherent and there is only one signal source, or
3. when signals are coherent and there is not the minimum number of signal sources required by (3.45).

When the noise is spatially uncorrelated, when there are coherent signals and when the conditions of (3.45) are met, it is not known whether the sensor and signal parameters are observable. These results were based on the assumption that the distance each signal travels from each sensor to the reference point is known to within plus or minus half a signal wavelength, which eliminates the ambiguities caused by phase wrapping. It is interesting to discover that the matrix **D**, where the $(mn)^{\text{th}}$ element of **D** is the distance from the m^{th} sensor to a reference point in the direction of arrival of the n^{th} signal, is rank 2 in the 2D case and rank 3 in the 3D case.

Chapter 4 New Array Calibrators

4.1 Enter the Calibrators

In this Chapter I describe three new array calibrators. Two of the algorithms are self calibrators. The first, given in Section 4.2, assumes the presence of a narrowband signal. It is designed to have a low computational demand on the array processor and to be insensitive to spatially uncorrelated noise. It uses a simple linear regression to obtain an impinging signal's phases at each hydrophone from measurements of the phase difference between all pairs of hydrophones. The phase-difference measurements come directly from the array-covariance matrix.

The second calibrator, given in Section 4.3, uses a broadband signal and estimates time delays. It is similar to the first because it uses the same linear regression to estimate the signal's times of arrival at each hydrophone from measurements of the time delay between all pairs of hydrophones. Broadband processing eliminates a number of problems that affect narrowband algorithms. Narrowband algorithms are sensitive to the presence of

1. multiple signals,
2. coherent signals and
3. spatially correlated noise;

the broadband algorithm in Section 4.3 is not. The computational requirements of this algorithm are greater than that of the narrowband self-calibrator. However, an advantage is that it is not necessary to find a suitable narrowband signal from the available spectrum. Both calibrators use the chord approach to apply known geometric constraints to the calibrating signal information to estimate the hydrophones' positions. The chord approach is described in Section 2.5.

The last towed-array calibrator that I present is based on a state-space representation of the array. This representation is derived from a simple, dynamical model of a towed, flexible cylinder's motion. A Kalman filter can be used to recursively estimate the array shape from heading-sensor data [GAB93]. I show how to include a self calibrator into the state-space framework and combine the signal information with heading-sensor data. The Kalman filter has a memory; the latest array-shape estimate is consistent with previous estimates according to the dynamical model of the array's motion. Thus, the Kalman filter will give array-shape estimates that are more accurate than a self calibrator alone can give. Although any self calibrator may

be used with the Kalman filter, I chose to use the narrowband one presented in Section 4.2. This inspired an interesting question: can a system with more measurements than states be equivalent to a system with an equal number of measurements as states? The answer is yes and I give a proof for this in Section 4.4.4.

4.2 A Narrowband Self Calibrator

I present a towed-array self calibrator that uses redundant information from an impinging, narrowband signal. The method is simple and computationally efficient, although its sensitivity to the presence of interfering signals is greater than methods which are computationally more complex. Hereafter, the algorithm is referred to as the least-squares error (LSE) method.

While a number of self calibrators exist in the literature, the LSE method was developed because of a perceived need to solve two problems with these algorithms. The first problem, shared by the eigenstructure [BMH91, GWR89, LM87] and sharpness [Buc78, Fer90b] methods, is the high computational demand they put on the signal processor; the LSE method puts a much lower computational load on the signal processor. The second problem, which the algorithms in [Dor78, WF88] exhibit, is the high sensitivity of the array-shape estimator to noise. The underwater acoustic environment is a noisy one and, possibly, the first estimation of the quality of towed-array calibrators will be based on how well they perform at low SNRs. Computer simulations have shown the LSE method to perform as well as any method at low SNR (Chapter 5). The LSE method does, however, show greater sensitivity to the presence of interfering signals than the self-calibrator in [GWR89]; this is the trade-off for reduced computational load.

For the LSE method, I make the following assumptions in addition to those given in Chapter 2:

1. the array and signals are restricted to two dimensions,
2. there is a far-field narrowband signal source (referred to as the **calibrating signal**) that allows us to estimate the array-shape,
3. the noise is spatially uncorrelated,
4. the calibrating signal is the only signal impinging upon the array in its frequency band,
5. the interhydrophone spacing is equal to, or less than, half the calibrating signal wavelength,

The arguments of the elements of the array-covariance matrix are modulo-2π measurements of the difference in phase of the calibrating signal between each pair of hydrophones. Section 4.2.1 describes the relation of the phase differences to the distance between pairs of hydrophones, in the direction of the calibrating signal. I show how the modulo-2π phase-difference measurements can be unwrapped uniquely, by observing that no phase-wrapping will occur between

hydrophones that are separated by less than half a wavelength. Section 4.2.2 contains the results of computer simulations of the LSE method. I investigate its sensitivity to noise and calibrating-signal frequency and DOA and compare the computational load with that of the calibrator in [GWR89].

4.2.1 Theory

Assuming there is only one narrowband signal impinging upon the array at a given frequency, then, from (2.15), the $(jk)^{\text{th}}$ element of the array-covariance matrix is given by

$$\begin{aligned} r_{jk} &= \sigma_s^2 \exp\left(j\pi(\chi_j - \chi_k)\delta_1\right) \\ &= \sigma_s^2 \exp\left(j\pi(d_{j1} - d_{k1})\right). \end{aligned} \tag{4.1}$$

From now on the subscript 1 will be dropped because there is only one impinging signal. Let $\{\psi_{jk}\}$ be the arguments of the array-covariance matrix elements so that $\psi_{jk} = \pi(d_j - d_k)$ modulo 2π. If the exact array-covariance matrix is not known and an estimate is used then an error term, e_{jk}, must be included. This gives a system of equations of the form

$$\left\{\hat{\psi}_{jk} + \lambda_{jk} = \pi(d_j - d_k) + e_{jk}\right\}, \tag{4.2}$$

where λ_{jk} is a multiple of 2π and the hat indicates an estimate. Using matrix notation we can write this as

$$\hat{\psi} + \lambda = \pi\mathbf{B}\mathbf{d} + \mathbf{e}, \tag{4.3}$$

where

$$\begin{aligned} \psi &= [\psi_{12}, \ldots, \psi_{1M}, \psi_{23}, \ldots, \psi_{M-1,M}]^{\mathrm{T}}, \\ \lambda &= [\lambda_{12}, \ldots, \lambda_{1M}, \lambda_{23}, \ldots, \lambda_{M-1,M}]^{\mathrm{T}}, \\ \mathbf{d} &= [d_1, \ldots, d_M]^{\mathrm{T}}, \\ \mathbf{e} &= [e_{12}, \ldots, e_{1M}, e_{23}, \ldots, e_{M-1,M}]^{\mathrm{T}} \end{aligned} \tag{4.4}$$

and $\mathbf{B}$ is a matrix of ± 1's and 0's of the form

$$\mathbf{B} = \begin{bmatrix} 1 & -1 & 0 & \ldots & 0 \\ 1 & 0 & -1 & \ldots & 0 \\ \vdots & \vdots & \vdots & \vdots & \vdots \\ 0 & \ldots & 0 & 1 & -1 \end{bmatrix}. \tag{4.5}$$

There are $M(M-1)/2$ pairs of hydrophones and so, for an array with more than two hydrophones, (4.3) is over determined. We take a least-square error estimate of $\mathbf{d}$ by minimising the error function $C = \left\|\hat{\psi} + \lambda - \pi\mathbf{B}\hat{\mathbf{d}}\right\|^2$, where $\|\ldots\|$ denotes a norm. If $\mathbf{P}$ is the Moore-Penrose pseudo inverse of $\mathbf{B}$ then C is minimised by choosing

$$\hat{\mathbf{d}} = \frac{\mathbf{P}\left(\hat{\psi} + \lambda\right)}{\pi}. \tag{4.6}$$

The estimate of $\mathbf{d}$ requires only one matrix multiplication, as $\mathbf{P}$ can be precalculated, which is an advantage for real-time applications.

Because $\hat{\psi}$ is a modulo-2π measurement of phase difference, some of the elements of λ are likely to be nonzero. However, we have assumed that the array has an interhydrophone spacing less than or equal to half the calibrating signal wavelength, so we know that there can be no phase wrapping between adjacent hydrophones and $\lambda_{m,m+1} = 0, \quad 1 \leq m < M - 1$. Also, the phase difference of the calibrating signal between two hydrophones, j and k, is equal to the sum of phase differences between each pair of adjacent hydrophones, in-between the j^{th} and k^{th},

$$\hat{\psi}_{jk} + \lambda_{jk} = \hat{\psi}_{j,(j+1)} + \hat{\psi}_{(j+1),(j+2)} + \ldots + \hat{\psi}_{(k-1),k} + \varepsilon_{jk}, \tag{4.7}$$

where the error term, ε_{jk}, is included because we have only the estimates of the phase differences. So, the 2π multiples that are associated with nonadjacent hydrophone pairs, $\lambda_{jk}, \quad k > j + 1$, can be found by choosing the value of λ_{jk} that minimises ε_{jk} in (4.7).

Once $\mathbf{d}$ is estimated the chord approach of Section 2.5 is used to estimate the hydrophones' positions.

4.2.2 Examples

To test the LSE algorithm I simulated a 35-element, uniformly spaced array with an interhydrophone spacing of 1. The sound field consists of spatially uncorrelated noise and a single 0 dB far field, narrowband signal with a centre frequency equal to the design frequency. The shape of the array is represented by the solid line in Figure 19. The exact noiseless array-covariance matrix was calculated using $\mathbf{R}_a = \mathbf{a}_1\mathbf{a}_1^{\text{H}}$, and an estimate of the noise-covariance matrix was added to this. The exact noise-covariance matrix is diagonal for spatially uncorrelated noise but its estimate has small nonzero terms off the diagonal. It is calculated with the time average of the covariances of 35 channels of white Gaussian noise, with 256 samples in each channel. The asterisks on Figure 19 represent the array shape estimated by the least-squares error algorithm, which closely matches the true array shape, when the signal was located at an angle of 90°. Figure 20 shows the wavelength-normalised, hydrophone position errors at each hydrophone. The RMS error is less than one-hundredth of a wavelength which is accurate enough for even very sensitive array processors.

Figure 19 Actual and estimated array shapes. Source direction is 90°.

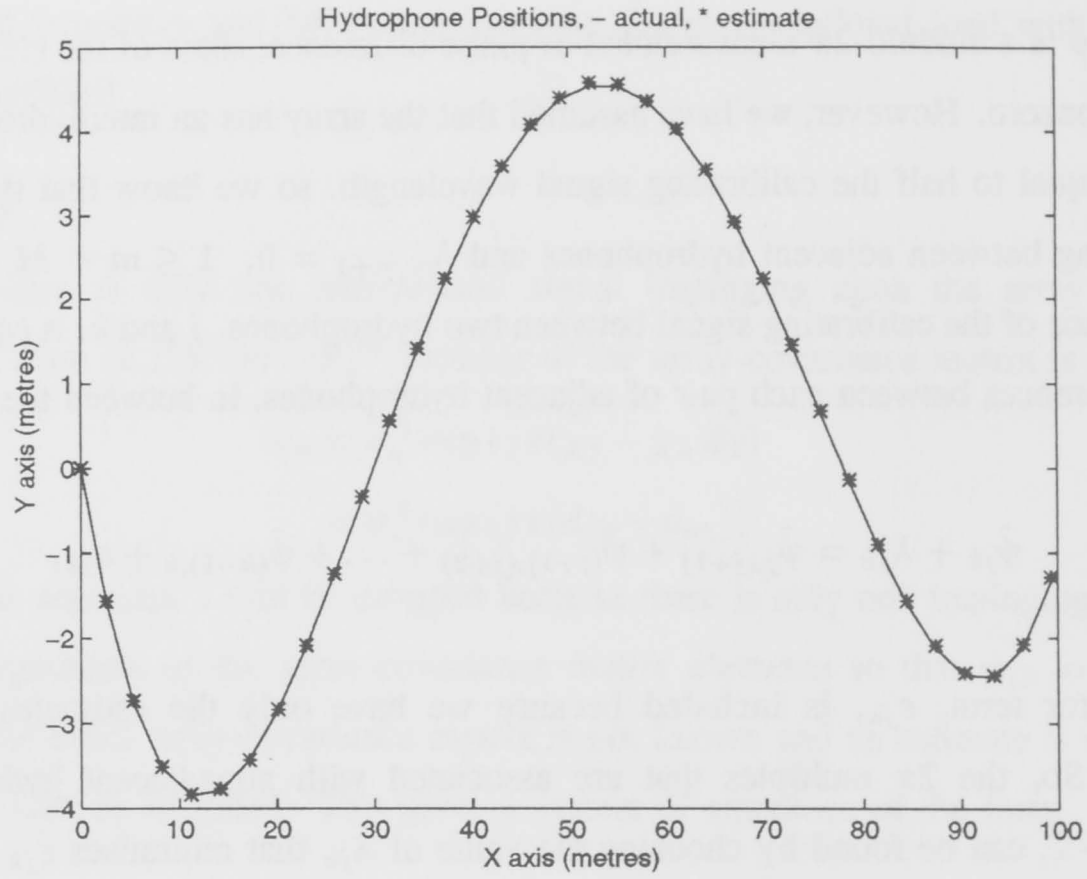

Figure 20 Normalised hydrophone position errors at each hydrophone. Source direction is 90°.

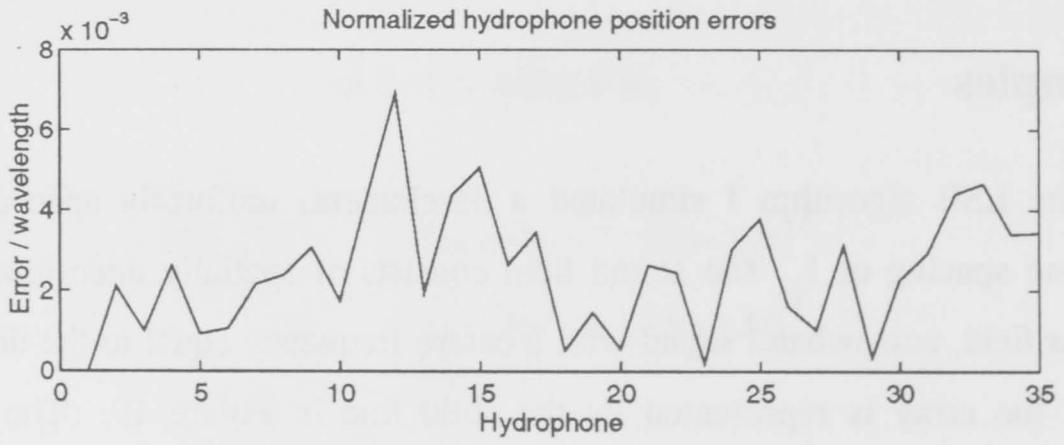

The LSE algorithm requires approximately $8M^3$ floating-point operations to produce an array shape from the array-covariance matrix. By comparison, the eigen decomposition of the array-covariance matrix, which is the fundamental operation used in [BMH91, GWR89, LM87], requires between $16M^3/3$ and $32M^3/3$ floating-point operations alone [PFTV87]. Thus, the LSE algorithm uses approximately one-half of the processing power of the algorithms of [BMH91, GWR89, LM87].

Table 2 shows some of the performance parameters for calibrating signal DOAs other than 90°, obtained through Monte Carlo trials of 50 simulations each. The performance parameters are

1. the calibrating-signal DOA estimation error,

2. the RMS error of estimation of the distance between each hydrophone and the reference point, in the direction of the calibrating signal, normalised by the signal wavelength, and
3. the RMS hydrophone position estimation error, normalised by the signal wavelength.

Regardless of the calibrating signal's DOA, the RMS, normalised distance error is of the order of 10^{-2}. The direction estimation error is less than 0.5° in all cases. The normalised hydrophone-position error is calculated with regards to the direction estimation error, that is, it indicates the accuracy of the shape estimate, and not the rotational errors which are caused by the direction-estimation error. The normalised hydrophone-position errors reflect the accurate relative distance estimates, until the calibrating signal sources reaches shallow DOAs, of 10° or less. At this point, the RMS position errors become unacceptably high. Of the two simultaneous solutions to (2.24) and (2.22) we assumed that the one closest to the x-axis was the correct one. When the signal DOA angle is less than the angle of the baseline from one hydrophone to the next, then that assumption is false, and large position errors will occur at these hydrophones, despite the high accuracy of the relative distance estimates. This can be seen in Figure 21, where the estimated array shape deviates from the actual between about $x = 20$ and $x = 50$ m.

Figure 21 Actual and estimated array shapes. Source direction is 10°.

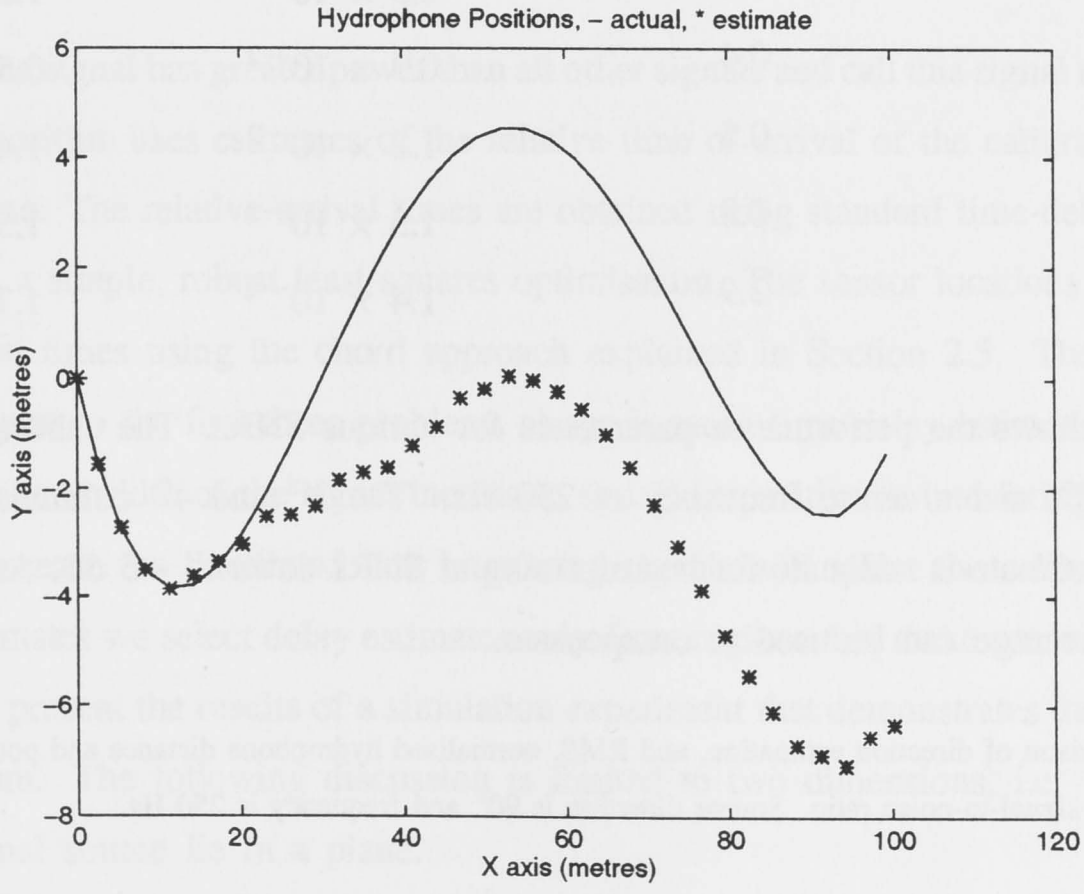

Table 3 shows the performance parameters as a function of the centre frequency of the calibrating signal, when the calibrating signal is at 90° and the array's design frequency is 250 Hz. The relative distance error is consistently good over all signal frequencies but the direction estimate becomes markedly worse at lower frequencies. This is consistent with the fact that resolution becomes worse at lower frequencies.

Table 2 Comparison of direction estimation and RMS, normalised, hydrophone distance and position errors as a function of source direction. Signal frequency is 250 Hz.

Signal DOA (degrees)	direction estimation error (degrees)	RMS distance error (dimensionless)	RMS position error (dimensionless)
90	0.3	1.3×10^{-2}	1.5×10^{-2}
45	0.2	1.4×10^{-2}	2.0×10^{-2}
20	0.3	1.3×10^{-2}	14×10^{-2}
10	0.3	1.3×10^{-2}	3.7
5.0	0.4	1.4×10^{-2}	7.9
1.0	0.4	1.3×10^{-2}	12

Table 3 Comparison of direction estimation, and RMS, normalised hydrophone distance and position errors as a function of frequency. Source direction is 90°.

Frequency (Hz)	direction estimation error (degrees)	RMS distance error (dimensionless)	RMS position error (dimensionless)
300	0.2	1.4×10^{-2}	1.5×10^{-2}
250	0.3	1.3×10^{-2}	1.5×10^{-2}
200	0.3	1.3×10^{-2}	1.5×10^{-2}
150	0.4	0.3×10^{-2}	0.5×10^{-2}
100	0.5	1.2×10^{-2}	1.4×10^{-2}
50	0.8	1.3×10^{-2}	1.5×10^{-2}
25	2.9	1.4×10^{-2}	1.7×10^{-2}

Table 4 shows the performance parameters for various SNRs. The calibrating signal has a DOA of 90°, and a centre frequency of 250 Hz. The 3rd and 4th columns show that the array-shape estimate is adequate for beamforming at SNRs down to −5 dB. At lower SNRs a longer time average can be used to compensate.

Table 4 Comparison of direction estimation, and RMS, normalised hydrophone distance and position errors as a function of signal-to-noise ratio. Source direction is 90° and frequency is 250 Hz.

Signal-to-noise ratio (dB)	direction estimation error (degrees)	RMS distance error (dimensionless)	RMS position error (dimensionless)
0	0.3	1.3×10^{-2}	1.5×10^{-2}
−5	0.7	4.2×10^{-2}	4.8×10^{-2}
−10	56	18	20

4.2.3 Summary of the narrowband self calibrator

The LSE algorithm estimates the signal delays with sufficient accuracy for beamforming over a wide range of frequencies. The method is insensitive to uncorrelated noise, because noise terms in the array-covariance matrix only appear on the diagonal, while the algorithm uses only off-diagonal elements. The effects of noise will be smaller when the array-covariance matrix is averaged for longer. The LSE method is computationally more efficient than the methods described in [BMH91, GWR89, LM87] by a factor of 2 or more. The method is compared, using computer simulations, with a variety of other self calibrators in Chapter 5.

4.3 A Broadband Self Calibrator

In this section I present an algorithm for calibrating a towed array using broadband signals. This algorithm is also known as the time domain method. The algorithm addresses the problems of

1. the availability of narrowband signals,
2. the presence of interfering signals, and
3. the presence of coherent signals.

I assume that one signal has greater power than all other signals and call this signal the calibrating signal. The algorithm uses estimates of the relative time of arrival of the calibrating signal at each hydrophone. The relative arrival times are obtained using standard time-delay estimation techniques and a simple, robust least-squares optimisation. The sensor locations are estimated from the arrival times using the chord approach explained in Section 2.5. The algorithm is robust with regard to the first three problems above because time-delay estimation is 1) more accurate as the bandwidth of the signal increases, and 2) insensitive to interfering and coherent signals. To decrease the likelihood that interfering signals will affect the calibrating signal's time-delay estimates we select delay estimates only from regions that make sense physically. In Section 4.3.2 I present the results of a simulation experiment that demonstrates the performance of the algorithm. The following discussion is limited to two dimensions, i.e. the array and calibrating signal source lie in a plane.

4.3.1 Estimating the relative time of arrival of the calibrating signal

Let the one impinging signal's time of arrival at the m^{th} hydrophone be t_m. The time of arrival is given by (2.9) where the subscript n for signal number is dropped because we are only interested in one signal, designated the calibrating signal. The **time delay of arrival** (TDOA), T_{jk}, between any pair of hydrophones is, by definition, the difference in relative

times of arrival. And so,

$$T_{jk} = t_j - t_k. \tag{4.8}$$

If the unknown TDOAs are estimated we must include an error term, e_{jk}, in (4.8). This gives a system of equations of the form

$$\left\{\hat{T}_{jk} = t_j - t_k + e_{jk}\right\}. \tag{4.9}$$

Using matrix notation we can write this as

$$\hat{\mathbf{T}} = \mathbf{Bt} + \mathbf{e}, \tag{4.10}$$

where

$$\begin{aligned} \mathbf{T} &= [T_{12}, \ldots, T_{1M}, T_{23}, \ldots, T_{M-1,M}]^{\mathrm{T}}, \\ \mathbf{t} &= [t_1, \ldots, t_M]^{\mathrm{T}}, \\ \mathbf{e} &= [e_{12}, \ldots, e_{1M}, e_{23}, \ldots, e_{M-1,M}]^{\mathrm{T}}, \end{aligned} \tag{4.11}$$

and $\mathbf{B}$ is a matrix of ± 1's and 0's of the form

$$\mathbf{B} = \begin{bmatrix} 1 & -1 & 0 & \ldots & 0 \\ 1 & 0 & -1 & \ldots & 0 \\ \vdots & \vdots & \vdots & \vdots & \vdots \\ 0 & \ldots & 0 & 1 & -1 \end{bmatrix}. \tag{4.12}$$

There are $M(M-1)/2$ pairs of hydrophones so, for an array with more than two receivers, (4.10) is over determined. We take a least-squares error estimate of $\mathbf{t}$ by minimising the cost function $C = \left\|\hat{\mathbf{T}} - \mathbf{Bt}\right\|$. The estimate of $\mathbf{t}$ is given by

$$\hat{\mathbf{t}} = \mathbf{P}\hat{\mathbf{T}}, \tag{4.13}$$

where $\mathbf{P}$ is the Moore-Penrose pseudo inverse of $\mathbf{B}$. The pseudo inverse can be calculated off line so that after estimating the TDOAs only one matrix multiplication is required to obtain the relative times of arrival.

The TDOA, T_{jk}, between every pair of hydrophones can be estimated using well-known generalised cross-correlation (GCC) techniques [Car93]. The generalised cross-correlation function is a standard cross correlator with two prefilters (see Figure 22). Various choices of the prefilters, $H_1(f)$ and $H_2(f)$, have been designed to enhance frequencies where the signal is strong, and attenuate frequencies where the noise is strong [Car93]. The TDOA estimate is the lag at which the GCC function is a maximum. There are no conditions on the spectrum of the signals; they do not have to be narrowband. In fact, the wider the bandwidth of the signals, the less is the chance of ambiguous TDOA estimates [Car93]. If the hydrophones receive N signals there will be N peaks in the GCC function. The lag of a peak corresponds to a particular

signal's TDOA between the two hydrophones. Assuming that the power of one of the signals is sufficiently greater than all the others, the delay of that signal will always be found as the lag of the biggest peak. This also applies in the case of multipath propagation, which gives rise to coherent signals. Assuming that the direct-path signal has greater power than the reflected-path signals then the biggest peak will correspond to the direct-path signal. For these reasons the GCC is insensitive to the presence of multiple and/or coherent signals.

Figure 22 Block diagram of a generalised cross correlator.

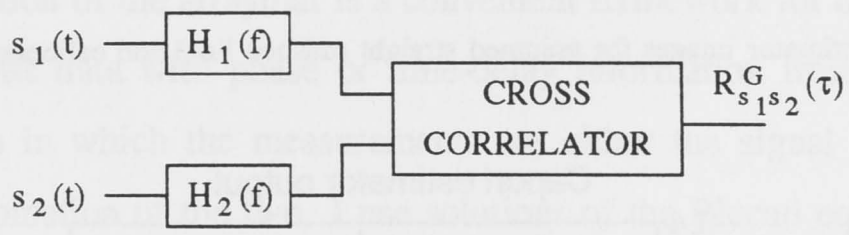

All of the time-delay estimates must relate to the one signal for (4.10) to be a consistent set of equations. In the presence of multiple signals consistency is ensured by the requirement that one source have greater power than any of the others. We can reduce interference from other signals and noise even further by searching for a maximum only in regions that make physical sense. If the hydrophones are adjacent the peak can be expected to occur at a lag in the range $-\rho/c_s \leq \hat{T}_{k,k+1} \leq \rho/c_s$, where ρ is the distance between the hydrophones. For non-adjacent hydrophones the peak can be expected to occur at a point close to the sum of the lags of all adjacent hydrophone pairs between the two being correlated. That is $\hat{T}_{jk} \approx \hat{T}_{j,j+1} + \ldots + \hat{T}_{k-1,k}$.

The times of arrival are used with geometric constraints to estimate the hydrophones' positions (see the description of the chord approach in Section 2.5).

4.3.2 Example

I simulate the array-calibration algorithm using a 32–element array with a hydrophone spacing of 1 and a speed of sound in water of 300 s^{-1}. The sound field consists of spatially uncorrelated noise and five far-field signal sources with a bandwidth of 1000 Hz. The first four signals have DOAs of 90°, 50°, 30° and 110°. Their SNRs are 0dB, −6dB, −6dB and −6dB respectively. The fifth signal simulates a reflection from the sea bed. It is coherent with the first, has a DOA of 90° and elevation 10° below the plane of the array with an SNR of −6dB. Standard cross correlations were used to estimate time delay using 1024 independent samples.

Figure 23 Actual (solid line) and estimated (dashed line) array shapes.

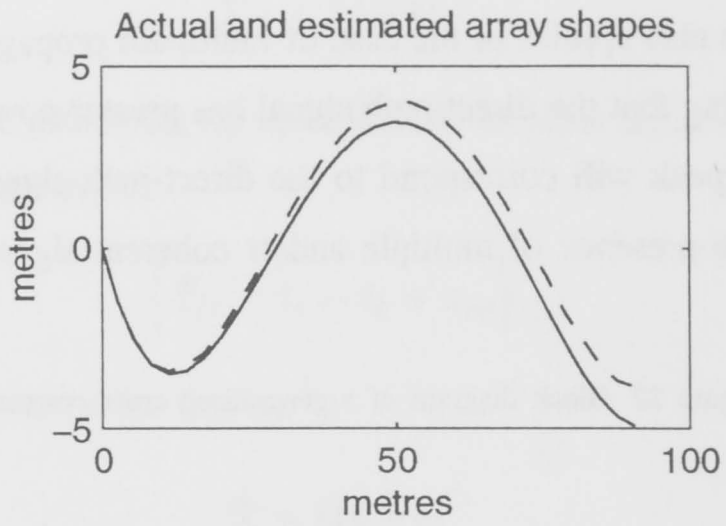

Figure 24 Capon estimator images for assumed straight (dashed line) and calibrated (solid line) arrays.

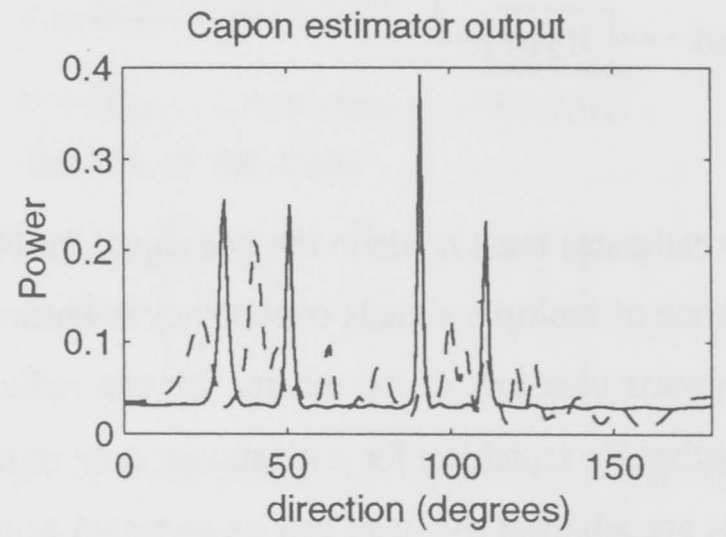

Figures 23 and 24 show the results of the simulation. In Figure 23 it can be seen that the estimated array shape appears identical to the actual shape, apart from a small rotation about the origin. The small rotation is due to a 0.7° error in the calibrating-signal DOA estimate. This error causes the beamformer image to be shifted by 0.7° but does not otherwise affect the image quality. Ignoring the DOA estimation error, the RMS hydrophone location error is only 2% of the interhydrophone distance (one-hundredth of a wavelength at the design frequency). Figure 24 shows the images from a Capon estimator assuming a straight array and a calibrated array. The straight array image shows no recognisable signal sources. However, the calibrated array image clearly shows all five signal sources (there are two at 90°).

4.3.3 Summary of the broadband self calibrator

The broadband algorithm estimates the shape of a towed array with sufficient accuracy for beamforming. The generalised cross correlation lends the algorithm robustness to the presence of interfering and coherent signals. If the SNR is low the effects of noise can be reduced by using more than 1024 samples for the generalised cross correlation. To minimise errors arising

from the incorrect assumption that the array shape is fixed for the duration of averaging, the number of samples cannot be too large. It is likely that low SNR would be the greatest hurdle for this algorithm when using real underwater data. Much substantial work on underwater time-delay estimation exists in the literature and so further investigation of this algorithm using underwater data is warranted.

4.4 Data Fusion Using Kalman Filters

In this Section I introduce a Kalman-filter-based array calibrator that uses heading-sensor measurements [GAB88, Gra86, GAB93, HRG90, RG]. The Kalman-filter calibrator uses a state-space representation of the arraythat is a convenient framework for data fusion. I propose combining the compass data with phase or time-delay information from a self calibrator. I present three systems in which the measurements are either the signal phases, the heading-sensor data or a combination of the two. I use solutions of the Riccati equation to predict and compare the mean-square error (MSE) of the state estimates, given each of these systems.

There is evidence that the shape of a towed array at one instant in time can be partially inferred from its shape at an earlier time [Ken81, RGH90]. For an array fitted with a small number of heading or depth sensors, this property can be used to estimate the slopes or transverse displacements of hydrophones at points where a heading or depth sensor is not located. Propagation of a thin, flexible cylinder's transverse displacements is described by a partial differential equation known as the **Paidoussis equation** [Pai66a, Pai66b]. Disturbances induced at the tow-point, termed **tow-point induced** (TPI) motion, with wavelengths that are long compared to the array length, propagate down the array at a speed close to the array's tow speed and are lightly attenuated [Dow88a, Dow88b, Ken81].

If the Paidoussis equation is discretised in time, the transverse displacement of a small segment of the array at one instant in time is related to the displacements of upstream segments at earlier instants. This suggests a discrete-time state-space formulation of the array, in which the state of the system is a finite-dimensional vector with components that are the transverse displacements of the segments [GAB93]. Alternatively, the states can be the slopes of the segments. The state-transition matrix, which describes how the states of the system at time t are related to the states at time $t-1$, is determined by the discretised Paidoussis equation. It is the same regardless of whether the states are displacements or slopes. Tow-point induced disturbances are introduced as driving terms which may or may not be known. The outputs of heading and depth sensors are related linearly to the states. Given this linear, state-space representation of the system, the Kalman filter is a powerful method of estimating the states of the system. Based on all measurements to the current time, it may be used to give an

estimate of the states at a future time (**prediction**), the present time (**filtering**) or some past time (**smoothing**). In addition, it is robust to model errors and incorrect assumptions about the noise statistics, which is desirable as oceanic conditions will introduce model errors in the array dynamics.

There are many examples of towed-array self calibrators in the literature [Buc78, Fer90b, Gor95c, GM95a, GWR89, MM92, Wah93]. Typically, these algorithms estimate the phase or time delay of a calibrating signal between each hydrophone and a reference hydrophone. The chord approach (Section 2.5) is then used to estimate the DOA of the calibrating signal and the hydrophone locations. The phase or time-delay estimates from any of these algorithms are related linearly to the states of the towed-array system, and so, they may be used to either replace or supplement measurements from heading sensors. The signal-based algorithms use the latest measurements only. Combining one of the self calibrators with the Kalman filter of [GAB93] will reduce the error of the hydrophone position estimates because all past measurements are used by the Kalman filter.

The state-space framework allows data from a self-calibrator to be fused with heading-sensor data. Data fusion will result in smaller errors than either a self-calibrator or heading-sensor-based calibrator alone will give.

In Section 4.4.1 I present the array-shape estimation problem within the state-space framework. The problem is assumed to be a two-dimensional one, where displacements are in the horizontal plane. The array is divided into equal-sized segments, each segment being a straight-line approximation of a short piece of the array. A hydrophone is assumed to be at each end of the segment. This assumption may be dropped at the expense of a more cumbersome notation. I assume TPI disturbances have long wavelengths in comparison to the length of the array so that the Paidoussis equation reduces to a simple, linear form. For the states I use the slopes of the segments which propagate down the array at close to the tow speed with little damping. The displacements of the segments may be used instead of slopes and the state-transition equations will not be any different. This is discussed further in Section 4.4.3.3.

The self calibrator I use is the least-squares error method of Section 4.2. I assume the DOA of the calibrating signal is known or estimated with the chord approach and the process noise-covariance matrix is diagonal. I give an interesting corollary that describes how to reduce the computational load of a Kalman filter when there are more measurements than states. The noise statistics of the phase estimates are all that is required to complete the state-space representation of the towed-array system [WRM94].

In section 4.4.2 I examine three systems that differ only by the measurements. The measurements for the three systems are heading sensors only, calibrating-signal phases only,

and phases and heading sensors combined. I compare the mean-square error of the Kalman filter's state estimates for each of the three systems. The mean-square errors of the three systems depend on the SNR of the hydrophone signals and heading sensors, the numbers of hydrophones or heading sensors, the number of snapshots of the hydrophone signals, the DOA of the calibrating signal and process noise of the state-transition equation. I briefly discuss transient response of the Kalman filter in Section 4.4.2.2

In Section 4.4.3 I discuss enhancements to the state-space system; I describe how the x-positions of the hydrophones may be incorporated into the state-space framework, observability of the measurement systems is examined and I give the measurement matrices for a system that uses displacements instead of slopes for the states.

4.4.1 Towed arrays in (state) space

Paidoussis [Pai66a, Pai66b, Pai73b] derived a differential equation describing the dynamics of thin, flexible cylinders towed in fluid. The Paidoussis equation was found by linearising viscous drag coefficients for small angles of attack. A term was omitted from this early work and Paidoussis gave the correct equation in [Pai73a]. A fourth-order term has a coefficient that depends on the bending stiffness of the cylinder. Because towed arrays have small diameters in relation to their lengths, the restoring force due to bending stiffness is very small. Recognising this, the bending stiffness has been assumed negligible and the Paidoussis equation approximated by a second order differential equation [Dow88a, Dow88b, Ken81, KS81, OI69]. It was found that for TPI disturbances with long wavelengths relative to the array length, every point on the cylinder follows the same path. This is referred to as **worm-in-hole** or **water pulley** motion. Incidentally, [Ken81, KS81, OI69] is based on Paidoussis' early erroneous equation, and [Dow88a, Dow88b] is based on Paidoussis' corrected equation. Despite this, these works agree in regards to long wavelength TPI motion.

In view of having already used the symbol x to represent hydrophones' longitudinal positions, I will go against convention and use the symbol $\mathbf{b}$ to represent the state vector. The discrete-time, state-space representation of a system is as follows [BH83]:

1. the linear system is modelled in the form

$$\mathbf{b}(t+1) = \mathbf{F}(t)\mathbf{b}(t) + \mathbf{u}(t) + \mathbf{w}(t) \tag{4.14}$$

and

2. the measurement of the process is represented by

$$\mathbf{z}(t) = \mathbf{H}(t)\mathbf{b}(t) + \mathbf{v}(t). \tag{4.15}$$

The terms and notation of (4.14) and (4.15) are:

$\mathbf{b}(t)$ =$(M \times 1)$ state vector at time t

$\mathbf{F}(t)$ =$(M \times M)$ state-transition matrix describing how the state at time $t+1$ is related to the state at time t in the absence of a forcing function

$\mathbf{u}(t)$ =$(M \times 1)$ driving-term vector at time t

$\mathbf{w}(t)$ =$(M \times 1)$ process-noise vector — a white sequence with known covariance

$\mathbf{z}(t)$ =$(N \times 1)$ measurement vector at time t

$\mathbf{H}(t)$ =$(N \times M)$ measurement matrix relating noise-free measurements to the state at time t

$\mathbf{v}(t)$ =$(N \times 1)$ measurement noise vector — a white sequence with known covariance that has zero cross correlation with $\mathbf{w}(t)$

Note that the number of measurements, N, may be different from the number of states, M. When the states are the slopes, the number of hydrophones is $M+1$. The covariance matrices of $\mathbf{w}(t)$ and $\mathbf{v}(t)$ are given by

$$\begin{aligned} \mathrm{E}\{\mathbf{w}(t)\mathbf{w}^{\mathrm{T}}(t)\} &= \mathbf{Q}(t) \\ \mathrm{E}\{\mathbf{v}(t)\mathbf{v}^{\mathrm{T}}(t)\} &= \mathbf{V}(t). \end{aligned} \tag{4.16}$$

I show how a towed array may be modelled as a state-space system in the following sections. Following the work of [Gra86, GAB88] Section 4.4.1.1 describes how the state-transition matrix is derived from the Paidoussis equation. Section 4.4.1.2 discusses the driving terms and model noise. The model noise accounts for approximation errors in the state-transition matrix and effects that are not due to TPI motion, such as ocean currents. Sections 4.4.1.3, 4.4.1.4 and 4.4.1.5 describe the three measurement systems that we will compare. These systems are: Section 4.4.1.3 heading-sensor measurement equations, Section 4.4.1.4 calibrating-signal measurement equations and Section 4.4.1.5 combined signal and sensor measurement equations. The signal and sensor data may be **synchronous** or **asynchronous**; the Kalman filter is able to handle both situations.

4.4.1.1 State-transition matrix

Assume we have a nominally linear towed array with hydrophones at regular spacings, ρ. Time is assumed to be normalised by the time it takes for the towing vessel to travel a distance of 1 (dimensionless unit). If the tow vessel's speed is U s^{-1} then time is normalised by $1/U$. Disturbances from long wavelength TPI motion were shown in [Ken81] to be governed by the equation

$$y(t,x) = f(x - \tilde{\omega}t). \tag{4.17}$$

The constant $\tilde{\omega}$ depends on the tangential and normal drags of the array, y is the transverse displacement of the array at distance x fro the tow point (x is measured in the opposite direction to the tow-vessel's course), and f describes the array's shape. The wavelength of a disturbance is considered to be long if it exceeds the length of the array. The term water pulley is used to describe disturbances that propagate down the array at a speed of $\tilde{\omega}U$ with little damping. The constant, $\tilde{\omega}$, is often close to unity.

Figure 25 Model of the discretised array.

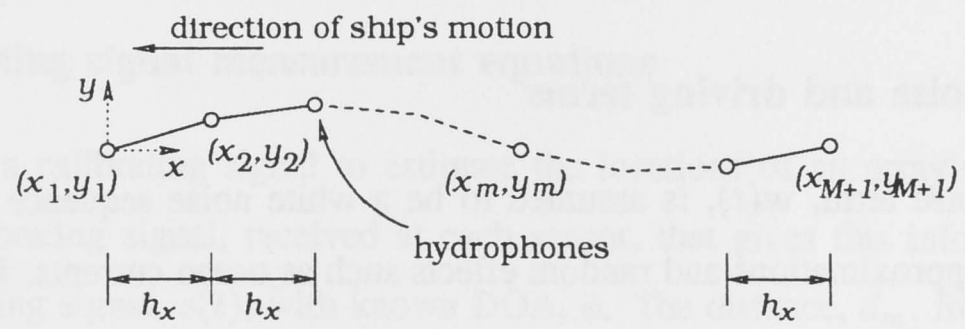

For small transverse deviations, I assume that the array shape can be represented using the model of Figure 25. In this model, the distances between adjacent hydrophones in the x-direction are constant and equal to the known hydrophone separation. Following [GAB93, Gra86], we discretise the Paidoussis equation in space and time. Let h_x be the spatial discretisation interval and h_t be the temporal discretisation interval. For a simpler notation we choose h_x to be equal to the hydrophone separation. The states, $\mathbf{b}(t) = [b_1(t), b_2(t), \ldots, b_M(t)]^T$, of the array system are the slopes of the segmented array between hydrophones and are given by

$$b_m = (y_{m+1} - y_m)/h_x. \tag{4.18}$$

The shape of an array with $M + 1$ hydrophones is completely defined by M states. The state-transition matrix, $\mathbf{F}$, for the water pulley model of (4.17) is

$$\mathbf{F} = (1 - \omega)\mathbf{I} + \omega\mathbf{L}, \tag{4.19}$$

where $\mathbf{L}$ is an $M \times M$ matrix whose only nonzero elements are on the first diagonal below the main diagonal and are equal to unity, i.e.

$$L = \begin{bmatrix} 0 & \cdot & \cdot & \cdot & 0 \\ 1 & 0 & \cdot & \cdot & \cdot \\ 0 & 1 & \cdot & \cdot & \cdot \\ \cdot & \cdot & \cdot & \cdot & \cdot \\ 0 & \cdot & 0 & 1 & 0 \end{bmatrix}. \tag{4.20}$$

The constant, ω, is given by

$$\omega = \tilde{\omega} h_t / h_x. \tag{4.21}$$

If the discretisation time, h_t, is selected so that $\omega = 1$, then $\mathbf{F} = \mathbf{L}$. This tells us that the slope of a segment at one instant equals the slope of an upstream segment at a previous instant. Bitmead and Anderson [BA84] suggest that the water pulley model is adequate in practice, and that it may be augmented by a damping coefficient, α, that is close to unity. With this, the state-transition matrix is

$$\mathbf{F} = \alpha\mathbf{L}. \tag{4.22}$$

4.4.1.2 Model-noise and driving terms

The model-noise term, $\mathbf{w}(t)$, is assumed to be a white noise sequence that accounts for transition matrix approximations and random effects such as ocean currents. Following [Gra86, GAB88], I assume that

$$\mathbf{Q}(t) = \sigma_q^2\mathbf{I}, \tag{4.23}$$

where σ_q^2 is the model-noise variance.

The driving term is defined by boundary conditions of the Paidoussis equation, and, for the water pulley model, $\mathbf{u}(t)$ is a vector with all elements zero except for the first. This represents TPI disturbances that are introduced into the system at each time instant. When the driving term is not known it is modelled as a white noise sequence with covariance, $\mathbf{U}(t) = \mathrm{diag}\left[\sigma_d^2, 0, \ldots, 0\right]$, where σ_d^2 is the TPI disturbance variance. The unknown driving term is uncorrelated with the model noise.

4.4.1.3 Heading sensor measurement equations

A heading sensor, placed in the middle of the m^{th} array segment, measures the angle of orientation, β_m, of that segment. This information is related linearly to the slope of the segment by

$$\begin{aligned}\tan\beta_m &= \frac{1}{h_x}(y_{m+1} - y_m) \\ &= x_m.\end{aligned} \tag{4.24}$$

Assume there are K heading sensors on segments $p_1, p_2, \ldots, p_K$ and the measurements are the tangents of the $\{\beta_m\}$. The measurement matrix, $\mathbf{H}_h$, is defined by

$$\mathbf{H}_h(k, m) = \delta_{p_k m}. \tag{4.25}$$

The measurement vector is given by $\mathbf{z}_h = [\tan\beta_1, \ldots, \tan\beta_K]^{\mathrm{T}}$. The measurement noise, $\mathbf{v}_h(t)$, will depend on the heading sensors used. I assume that the noise at one sensor is

independent of the noise at the other sensors and so the measurement noise-covariance matrix is diagonal. For small measurement variance, σ_β^2, the tan function can be approximated by a line around the mean of the angle measurement, $\bar{\beta}_m$. The slope of the tan function at this point is $\tan^2 \bar{\beta}_m + 1$. Therefore, the variance of the slope estimate is $\sigma_\beta^2 (\tan^2 \bar{\beta}_m + 1)^2$. And so, the measurement noise-covariance matrix can be approximated by

$$\mathbf{V}_c = \sigma_\beta^2 \text{diag}\left[(\tan^2 \bar{\beta}_1 + 1)^2, \ldots, (\tan^2 \bar{\beta}_K + 1)^2 \right]. \tag{4.26}$$

4.4.1.4 Calibrating signal measurement equations

When using a calibrating signal to estimate the locations of an array's sensors it is the phase of the calibrating signal, received at each sensor, that gives this information. Assume there is a calibrating signal, $s(t)$, with known DOA, ϕ. The distance, d_m, from the first sensor to the m^{th} along the line of sight to the calibrating signal source can be obtained by observing the phase, θ_m, of arrival of the calibrating signal as it is received at each sensor. From (2.11), d_m is given by

$$d_m = \frac{1}{\pi}(\theta_m - \theta_1), \tag{4.27}$$

where the subscript n has been dropped because we are dealing with only one signal.

Specific methods of obtaining the calibrating signal's phases is the subject of much literature. I have chosen to use the least-squares algorithm of Section 4.2. I choose this calibrator because it uses a simple linear regression to estimate $\{\theta_m\}$ which, in the context of Kalman filtering, poses an interesting question. The question deals with state-space systems that have more measurements than states and I discuss this in Section 4.4.4.

From (2.8) and (4.27),

$$\theta_m - \theta_1 = \pi(x_m \cos\phi + y_m \sin\phi), \tag{4.28}$$

and subtracting $\theta_{m-1} - \theta_1$ from both sides,

$$\begin{aligned} \theta_m - \theta_{m-1} &= \pi((x_m - x_{m-1})\cos\phi + (y_m - y_{m-1})\sin\phi) \\ &= \pi h_x(\cos\phi + b_m \sin\phi). \end{aligned} \tag{4.29}$$

This can be written in matrix form as

$$\mathbf{z}_s(t) = \pi h_x \sin\phi \mathbf{I}\,\mathbf{b}(t) + \mathbf{v}_s(t), \tag{4.30}$$

where

$$\begin{aligned} \mathbf{z}_s(t) = [\theta_2(t) - \theta_1(t), \ldots, \theta_{M+1}(t) - \theta_M(t)]^{\text{T}} \\ -\pi h_x \cos\phi(k)[1, \ldots, 1]^{\text{T}} \end{aligned} \tag{4.31}$$

and $\mathbf{v}_s(t)$ is the measurement noise of $\{\theta_m - \theta_{m-1}\}$. The measurement matrix is

$$\mathbf{H}_s = \pi h_x \sin\phi\, \mathbf{I}. \tag{4.32}$$

The measurement noise-covariance matrix, $\mathbf{V}_s$, is given by

$$\begin{aligned}\mathbf{V}_s &= \mathrm{E}\left[\mathbf{v}_s(t)\mathbf{v}_s^{\mathrm{T}}(t)\right] \\ &= \mathrm{Cov}\left[\mathbf{z}_s(t)\mathbf{z}_s^{\mathrm{T}}(t)\right] \\ &= \mathbf{P}\mathrm{Cov}\left[\left(\hat{\psi}(t)+\lambda(t)\right)\left(\hat{\psi}(t)+\lambda(t)\right)^{\mathrm{T}}\right]\mathbf{P}^{\mathrm{T}},\end{aligned} \tag{4.33}$$

where $\hat{\psi}(t) + \lambda(t)$ is given in (4.2). Wylie et al [WRM94] use a random model for the calibrating signal and show that

$$\mathrm{Cov}\left[\left(\hat{\psi}(\mathrm{t})+\lambda(\mathrm{t})\right)\left(\hat{\psi}(\mathrm{t})+\lambda(\mathrm{t})\right)^{\mathrm{T}}\right] = \frac{1}{2J}\left(1+\frac{\delta_{mk}}{\mathrm{SNR}}\right)\left(1+\frac{\delta_{jn}}{\mathrm{SNR}}\right), \tag{4.34}$$

where SNR is the signal-to-noise ratio and J is the number of time samples of data used to calculate the array-covariance matrix. We note that if a deterministic model for the calibrating signal is used the covariance matrix of $\hat{\psi}(t)+\lambda(t)$ will be different. There is no clear argument for using one model over the other so we use the random model.

4.4.1.5 Combined sensor and signal measurement equations

The state-space structure allows the two separate measurement equations of Sections 4.4.1.3 and 4.4.1.4 to be combined into one. Assuming that the measurements are available synchronously, the combined equation is

$$\mathbf{z}_c(t) = \mathbf{H}_c\mathbf{x}(t) + \mathbf{v}_c(t), \tag{4.35}$$

where

$$\mathbf{z}_c(t) = \left[\frac{\mathbf{z}_h(t)}{\mathbf{z}_s(t)}\right], \quad \mathbf{H}_c = \left[\frac{\mathbf{H}_h}{\mathbf{H}_s}\right], \quad \text{and} \quad \mathbf{v}_c(t) = \left[\frac{\mathbf{v}_h(t)}{\mathbf{v}_s(t)}\right]. \tag{4.36}$$

The heading-sensor measurement noise is independent of the calibrating-signal noise, and so, the measurement noise-covariance matrix is given by

$$\mathbf{V}_c = \begin{bmatrix}\mathbf{V}_h & \mathbf{0} \\ \mathbf{0} & \mathbf{V}_s\end{bmatrix}. \tag{4.37}$$

For convenience, I have, till now, dropped the notation showing dependency on time of $\mathbf{H}_c, \mathbf{H}_h, \mathbf{H}_s, \mathbf{V}_c, \mathbf{V}_h$ and $\mathbf{V}_s$. The Kalman filter allows these matrices to vary in time. And so, if heading-sensor and signal-phase measurements are not available at the same instants, the Kalman recursion equations need only use the $\mathbf{H}$ and $\mathbf{V}$ matrices that are appropriate. This **asynchronous** measurement Kalman filter makes use of whatever measurements are available at any instant.

4.4.2 Examples and discussion

Based on a set of measurements up to the current time, the Kalman filter may be used to estimate the states at a future time (prediction), the current time (filtering) or a past time (smoothing). One step prediction, denoted $\hat{\mathbf{b}}(t+1|t)$, predicts the state at time $t+1$, conditional on all measurements up to time t. Filtering, denoted $\hat{\mathbf{b}}(t|t)$, estimates the states at time t based on measurements up to the same time. For array calibration, this is the technique most likely to be used. **Fixed-lag** smoothing, denoted $\hat{\mathbf{b}}(t-K|t)$, estimates the states at K sampling instants before the latest measurement, where K is the fixed lag interval. The real-time constraints of processing power and memory requirements are likely to preclude smoothing from at-sea applications.

The Kalman filter recursively estimates the state-estimation error, as well as the states themselves. Solutions of the Riccati equation tell us what the steady-state, state-estimation error will be, independent of the measurements. In this section I compare the state-estimation errors for prediction, filtering and smoothing of the three systems defined by the measurement equations (4.25, 4.26), (4.30) and (4.36). I also investigate the sensitivity of the Kalman filter to calibrating-signal-DOA estimation errors. The simulated array is uniform and has 20 hydrophones (19 states) and the states are the slopes of the flexible cylinder between adjacent hydrophones. The spatial discretisation interval, h_x is 1. Deviations in the tow-vessel's course cause TPI motion of the array. The TPI motion has a frequency low enough that the water pulley model may be used. The temporal discretisation interval is chosen to be $h_t = 1/\tilde{\omega}$, so that $\omega = \tilde{\omega}h_x/h_t = 1$. In other words, the temporal discretisation interval is the time taken for a disturbance to move one spatial discretisation interval. The variance of the heading sensor measurements is assumed to be 1°. The sampling rate of the hydrophones is 1428 per discretisation interval. The process attenuation constant, α, is 0.9, which corresponds to a damping of 0.14 over the whole array. The driving term is unknown and is assumed to have variance equal to the process noise variance. Hydrophone SNR, process noise variance, σ_q^2, and calibrating-signal DOA are treated specially in 4.4.2.1. There are four heading sensors located at the first, 5th, 10th and 15th segments of the array.

4.4.2.1 Specific examples

Figure 26 shows the steady-state estimation errors for prediction, filtering and infinite fixed-lag smoothing. The SNR is -20dB, $\sigma_q^2 = 0.05$ and calibrating signal DOA is 90°. Part (a) shows results for the heading-sensor-only measurement equations (4.25, 4.26), part (b) shows the results for the calibrating-signal-only measurement equations (4.30) and part (c) shows the results for the combined measurement equations (4.36). Mean-square errors are plotted against

segment number. Prediction is represented by the dotted lines, filtering by the solid lines and smoothing by the dashed lines.

Figure 26 Mean square errors of the Kalman filter for (a) calibrating-signal measurements only, (b) heading-sensor measurements only and (c) calibrating-signal and heading-sensor measurements combined. SNR=−20dB, $\sigma_q^2 = 0.05$ and DOA=90°.

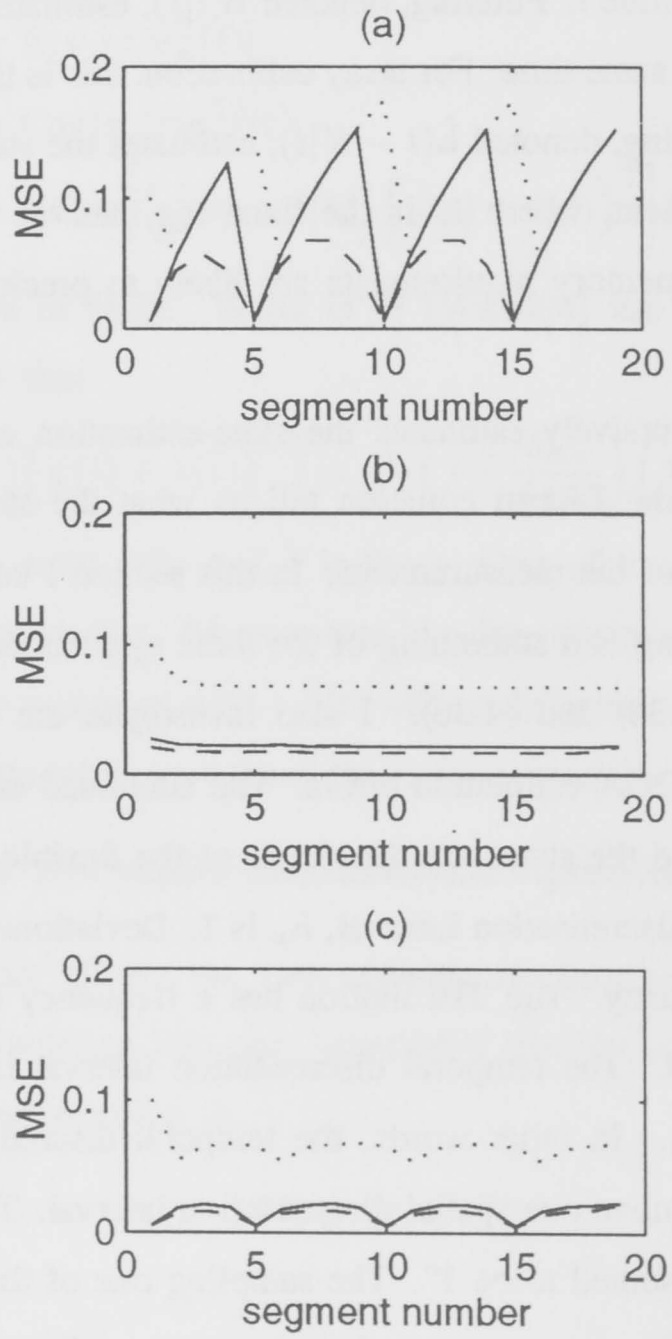

The characteristics of the MSEs in Figure 26(a) have been discussed in [GAB93], and I briefly recount that discussion. At segments with a heading sensor, the MSE equals the heading sensor variance. Downstream of heading sensors the MSE increases by σ_q^2 less an amount proportional to the damping factor. The damping factor causes the filter's MSE function to curve on the upward ramp. Without a heading sensor at the end of the array the prediction, filtering and smoothing MSEs are identical after the last heading sensor. Prediction and filtering errors only differ at segments where heading sensors are located

The MSEs in Figure 26(b) are largely constant with respect to segment number. Slight variations of the errors are due to the non-uniform structure of the calibrating-signal, noise-covariance matrix of (4.34). At this SNR the error of the phase estimates is around 0.11π. After division by π and filtering, the MSE of the state estimates is around 0.03. The error

reduction is due to the Kalman filter's use of all measurements to the current time. The MSE of the predictor is the sum of the filter MSE and the process noise variance. As expected, the infinite fixed-lag smoother has a smaller error than the filter.

The MSEs for the combined heading-sensor and calibration-signal measurements (Figure 26(c)) are always less than the MSEs of the separate measurement systems. Given that, in this example, the MSEs of Figure 26(b) are much less than those of Figure 26(a), the improvement in Figure 26(c) over Figure 26(b) is not very great.

Figure 27 shows the effect of DOA on the MSE of the calibrating-signal measurement system. The DOA in Figure 27 is (a) 90°, (b) 45°, (c) 10° and (d) 0° and the SNR is −20 dB. The graphs show only the filter MSE. The performance of the calibrating-signal-only measurement system is dependent on DOA. As the DOA approaches endfire the calibrating signal provides less information about the transverse displacements of the hydrophones, and so, the MSE increases. When the calibrating signal is at endfire, it gives no information about the transverse displacements at all, and the Kalman filter will estimate a straight array shape.

Figure 27 MSE of the Kalman filter state estimates using a calibrating signal with DOA of (a) 90°, (b) 45°, (c) 10° and (d) 0°. SNR is −20 dB.

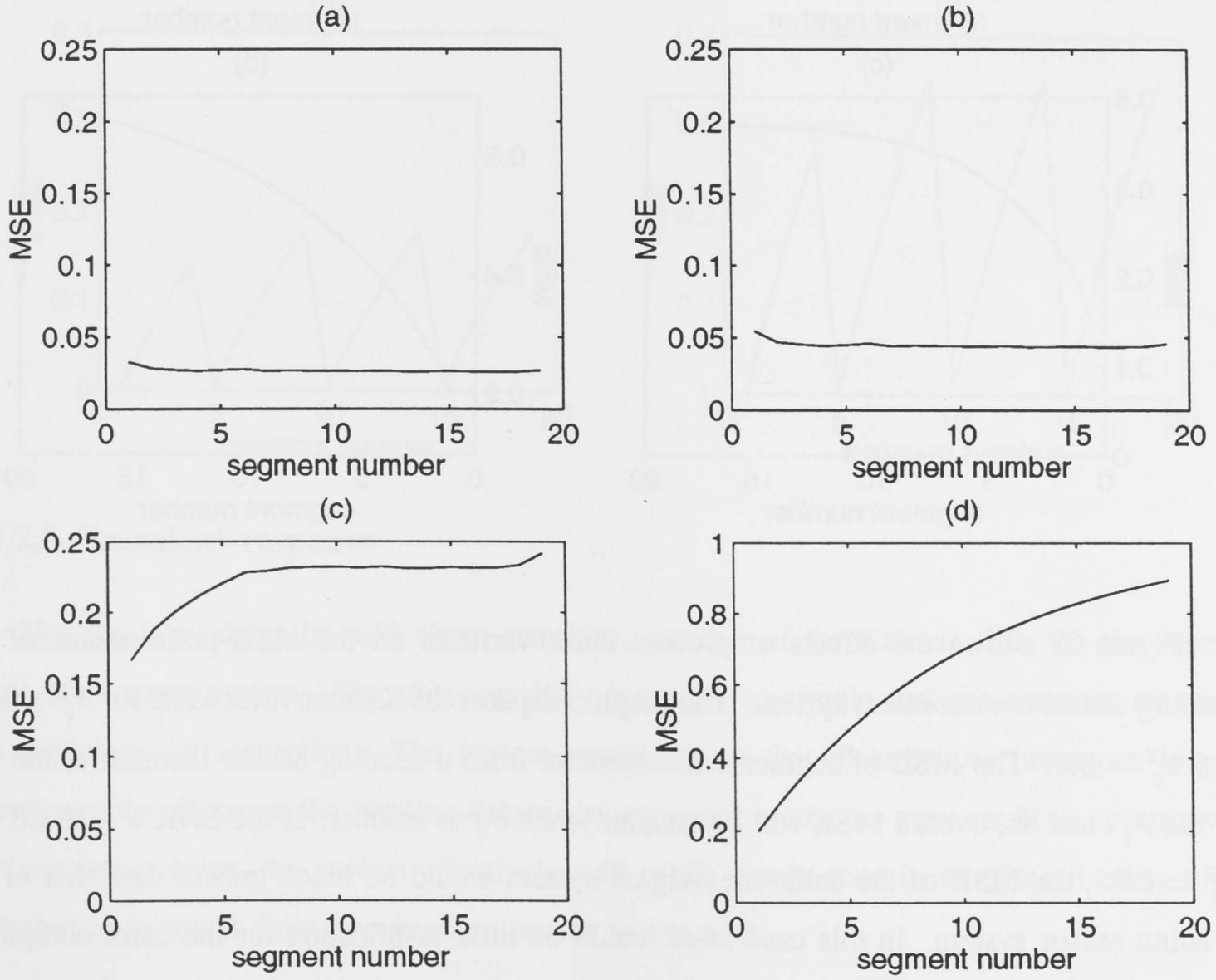

Figure 28 shows the MSE performance of the calibrating-signal measurement system at different SNRs. The filter MSE is shown for SNRs of (a) −20 dB, (b) −25 dB, (c) −30 dB

and (d) −35 dB and DOA of 90°. As expected, the MSE is greater at low SNR. The effects of low SNR can be offset by increasing the number of hydrophone signal samples, although, the maximum number of samples is limited by errors arising from the incorrect assumption that the array shape is fixed for the duration of averaging. If the number of hydrophones is increased, the redundancy of the measured information will be greater. Therefore, increasing the number of hydrophones will offset the effects of low SNR, too.

Figure 28 MSE of the Kalman filter state estimates using a calibrating signal with SNR of (a) −20 dB, (b) −25 dB, (c) −30 dB and (d) −35 dB. DOA is 90°.

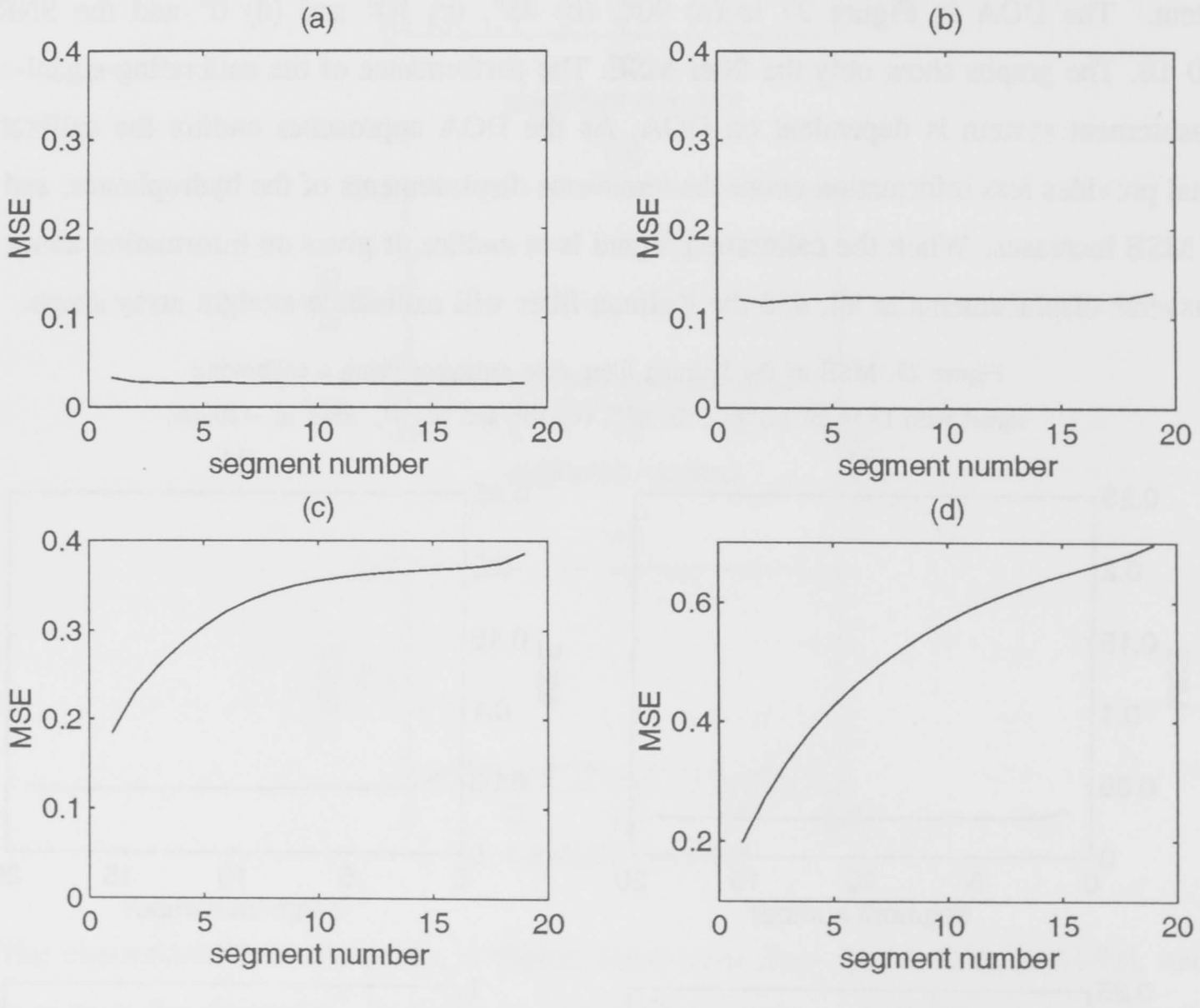

Figure 29 shows the effects of process noise variance on the MSE performance of the heading-sensor measurement system. The graph compares the Kalman filter MSE for $\sigma_q^2 = 0.05$ and $\sigma_q^2 = 0.1$. The MSE of segments downstream from a heading sensor increase at the rate of the σ_q^2, and so, overall MSE will be smaller when σ_q^2 is smaller. If the SNR = −30 dB and $\sigma_q^2 = 0.05$, the MSE of the calibrating-signal system would be much greater than that of the heading-sensor system. In this case there would be little justification for the extra computing effort of using calibrating-signal information in a combined-measurement system. On the other hand, if SNR = −20 dB and $\sigma_q^2 = 0.1$, the MSE of the heading-sensor system would be much greater than that of the calibrating-signal system, while the DOA is not near endfire. In this

case, in a combined measurement system, heading-sensors would only be useful if the DOA was near endfire.

Towed-array self calibrators rely on knowledge of the calibrating-signal DOA. So far, I have assumed that the calibrating-signal DOA is known exactly. In practice, it will not be known and an estimate will have to be used instead. For this reason, it is important to know how sensitive the state estimates are to errors in the estimate of DOA. The array model of Figure 25 counteracts rotational ambiguities by constraining the array to be close to a line defining the tow-vessel's path. Overall, the Kalman filter is insensitive to calibrating-signal-DOA estimation errors. Figure 30 compares MSEs when the DOA is known exactly (solid line) and when it is known approximately (dashed line). When the DOA is 80° and the estimate is 90° (Figure 30(a)) the MSE appears no worse than if the DOA had been known exactly. When the DOA is 10° and its estimate is 20° (Figure 30(b)) there is a slight deterioration of the MSE over the case when DOA is known exactly. The MSE is increased by only 4% at most, when there is a 10° DOA-estimation error.

Figure 29 MSE of the Kalman filter state estimates using heading sensors with process noise variance of (a) 0.05 and (b) 0.1.

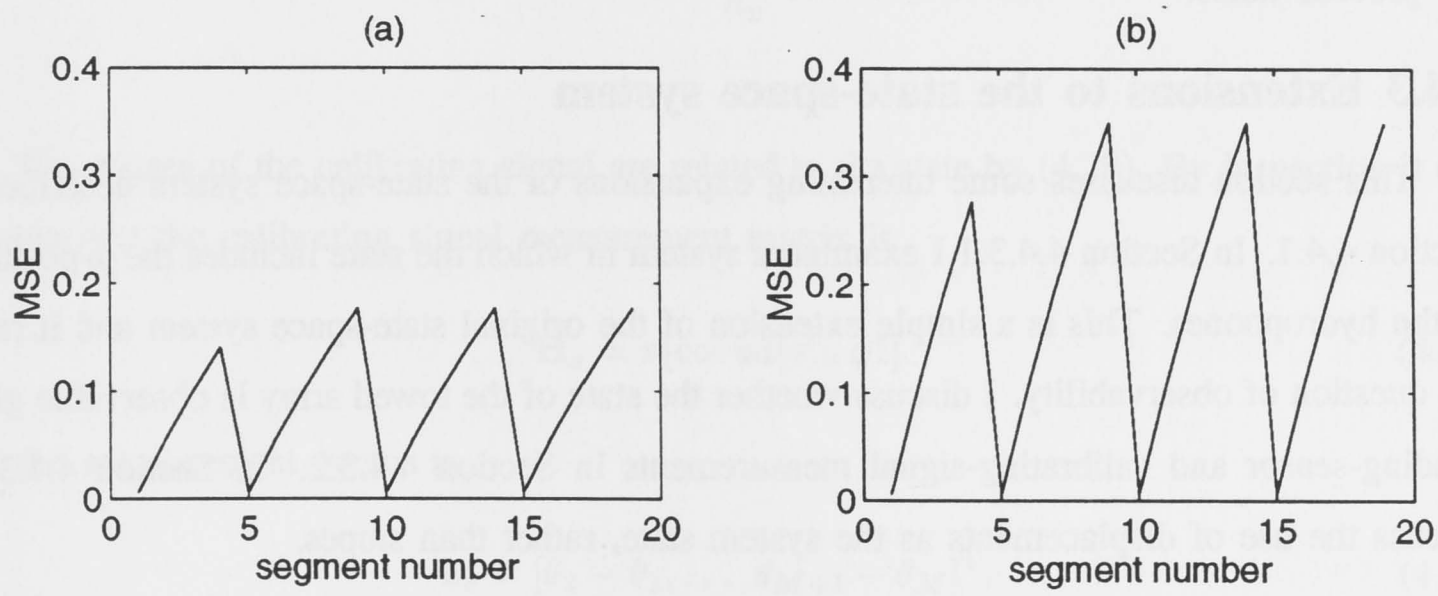

4.4.2.2 Transient response

Not much needs to be said about transient response of the Kalman filter on the towed-array, state-space system. The state-transition matrix is so simple that the transient response can explained by inspection. The system model shows that disturbances propagate in one direction only. Because the heading-sensor-measurement errors are very small in comparison to the process noise, the system effectively will reach steady state in the time it takes for a disturbance to travel from one heading sensor to the next.

The signal-based-measurement errors are comparable to the process noise and so, even though measurements are made at every spatial discretisation interval, a disturbance will have to travel some number of intervals before the Kalman filter reaches a steady-state error. The

Figure 30 MSE of the state estimates when the DOA is known exactly (solid line) and when DOA estimate is used in place of its true value (dashed line). (a) ϕ=80°, $\hat{\phi}$=90°, (b) ϕ=10°, $\hat{\phi}$=20°.

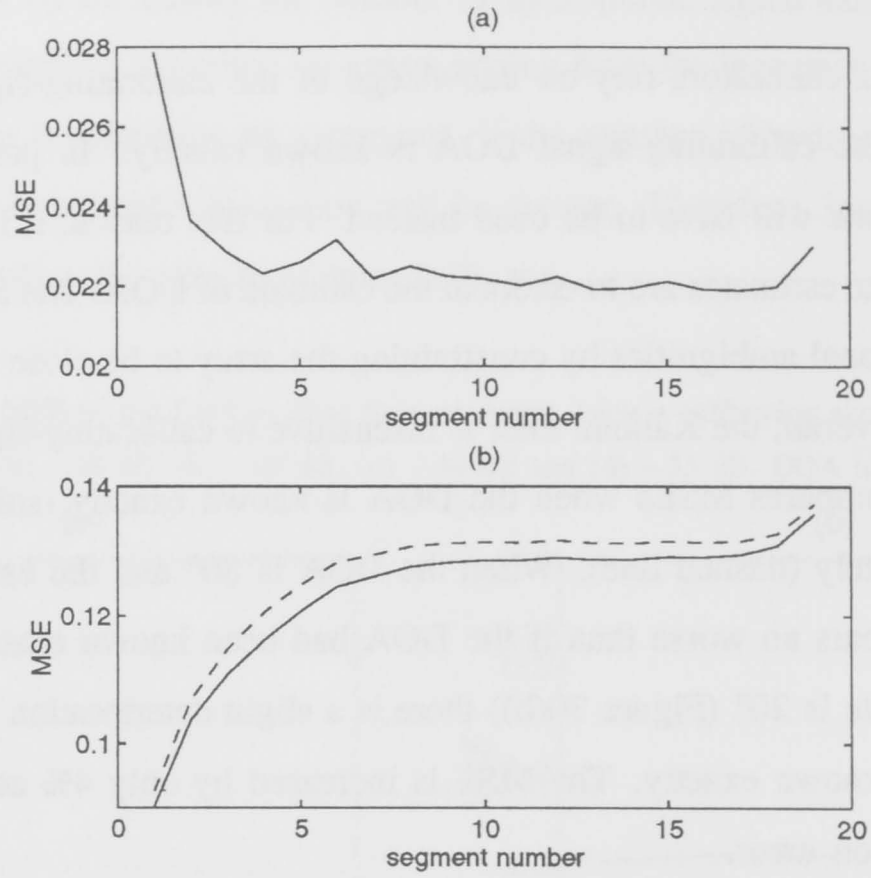

exact number of intervals depends on the relative magnitudes of the measurement errors and the process noise.

4.4.3 Extensions to the state-space system

This section discusses some interesting expansions of the state-space system described in Section 4.4.1. In Section 4.4.3.1 I examine a system in which the state includes the x-positions of the hydrophones. This is a simple extension of the original state-space system and it raises the question of observability. I discuss whether the state of the towed array is observable given heading-sensor and calibrating-signal measurements in Section 4.4.3.2. In Section 4.4.3.3 I discuss the use of displacements as the system state, rather than slopes.

4.4.3.1 Augmenting the state vector

Our model for the discretised array of Figure 25 assumes that the x-positions of the hydrophones are constant and known, however, in some cases, it may be of interest to estimate the x-positions of the hydrophones. To allow this we can model the x-positions as time-varying, unknown quantities by augmenting the state vector. The augmented state vector is given by

$$\mathbf{b} = [x_2 - x_1, \ldots, x_{M+1} - x_M, y_2 - y_1, \ldots, y_{M+1} - y_M]^{\mathrm{T}}. \tag{4.38}$$

The x-direction terms, $\{x_{m+1} - x_m\}$, are assumed to propagate undamped, whilst the usual damping applies to the y-direction terms, $\{y_{m+1} - y_m\}$. In this case the augmented state-transition matrix will be given by

$$\mathbf{F}_a = \begin{bmatrix} \mathbf{L} & \mathbf{0} \\ \mathbf{0} & \alpha\mathbf{L} \end{bmatrix}. \tag{4.39}$$

We assume the process noise-covariance matrix to be diagonal, and given by

$$\mathbf{Q} = \begin{bmatrix} \sigma_{q1}^2\mathbf{I} & \mathbf{0} \\ \mathbf{0} & \sigma_{q2}^2\mathbf{I} \end{bmatrix}, \tag{4.40}$$

where σ_{q1}^2 and σ_{q2}^2 are process noise variances for the x-direction and y-direction terms, respectively. If the driving term is not known it may be modelled as a white-noise sequence with covariance given by

$$\mathbf{U} = \text{diag}\left[\sigma_{u1}^2, 0, \ldots, 0, \sigma_{u2}^2, 0, \ldots, 0\right], \tag{4.41}$$

where σ_{u1}^2 and σ_{u2}^2 are process noise variances for the x-direction and y-direction terms, respectively.The heading-sensor slopes are related to the state by

$$\tan\beta_k = \frac{y_{k+1} - y_k}{x_{k+1} - x_k}, \tag{4.42}$$

which is not linear in x_k. Assume that the $x_{k+1} - x_k$ term in (4.42) can be replaced by the constant, h_x. And so, the heading sensor measurement matrix is defined by

$$\mathbf{H}_h(k,m) = \frac{1}{h_x}\delta_{p_k+M,m}. \tag{4.43}$$

The phases of the calibrating signal are related to the state by (4.29). By inspection it can be seen that the calibrating signal measurement matrix is

$$\mathbf{H}_s = \pi[\cos\phi\mathbf{I}|\sin\phi\mathbf{I}] \tag{4.44}$$

and the measurement vector is

$$\mathbf{z}_s = [\theta_2 - \theta_1, \ldots, \theta_{M+1} - \theta_M]^{\mathrm{T}}. \tag{4.45}$$

4.4.3.2 Observability of the state

From [AM79], the state of a system is unobservable if an eigenvector of the state-transition matrix, $\mathbf{F}$, lies in the null space of the measurement matrix, $\mathbf{H}$. That is, if there exists a $\mathbf{w} \neq \mathbf{0}$ such that

$$\begin{aligned} \mathbf{F}\mathbf{w} &= \lambda\mathbf{w}, \quad \text{and} \\ \mathbf{H}\mathbf{w} &= \mathbf{0}. \end{aligned} \tag{4.46}$$

In [GAB93] it was shown that, the eigenvectors of $\mathbf{F}$ are all of the form $[0, \ldots, 0, w_M]^{\mathrm{T}}$. For $w_M \neq 0$, $\mathbf{H}_h\mathbf{w} = \mathbf{0}$ only if the last column of $\mathbf{H}_h$ is the zero vector. Thus, for the

state to be observable, a heading sensor must exist on the last segment of the array, when the only measurements are from heading sensors. This is because disturbances are modelled as travelling only downstream. Any disturbance generated after the last heading sensor on the array will propagate aft, undetected. And so, unless there is a heading sensor at the end of the array, some states will be unobservable. The last column of $\mathbf{H}_s$ is not the zero vector so the calibrating-signal system is always observable.

Using the augmented matrices of Section 4.4.3.1, the eigenvalues of $\mathbf{F}_a$ are all zero. The first M eigenvectors have the form $[0,\ldots,0,w_M,0,\ldots,0]^{\mathrm{T}}$ and the second M eigenvectors have the form $[0,\ldots,0,w_{2M}]^{\mathrm{T}}$. The first M eigenvectors of $\mathbf{F}_a$ are in the null space of the augmented $\mathbf{H}_h$ matrix so the x-positions of the hydrophones are unobservable using heading sensors. This is not surprising, as the heading sensors do not give any information about the segments' x-positions. The M^{th} and last columns of the augmented $\mathbf{H}_s$ matrix are non-zero and so the augmented state is always observable when using calibrating-signal measurements.

4.4.3.3 Using displacements in the state vector

There may be situations where the displacements of segments of the array are of more interest than the slopes. If the Paidoussis equation is discretised such that the states are displacements, then the state-transition matrix will have the form given in (4.22) [GAB93]. That is, the state-transition matrix will be the same whether the states are slopes or displacements. The measurement matrices will be slightly different. For heading sensors, the measurement vector is given by

$$\mathbf{z}_h = [\tan\beta_1,\ldots,\tan\beta_K]^{\mathrm{T}}. \tag{4.47}$$

The measurement matrix is defined by

$$\mathbf{H}_{km} = \frac{1}{h_x}(\delta_{p_k m+1} - \delta_{p_k m}). \tag{4.48}$$

For a calibrating signal the measurement equations come from (4.28). Each segment of the array is assumed to have one hydrophone at its centre ($h_x = 1$) and the displacements of the segments are measured with respect to the first. The measurement vector is

$$\mathbf{z}_s = [\theta_2 - \theta_1,\ldots,\theta_{M+1} - \theta_1]^{\mathrm{T}} - \pi h_x \cos\phi\,[1,2,\ldots,M]^{\mathrm{T}} \tag{4.49}$$

and the measurement matrix is

$$\mathbf{H}_s = \sin\phi\,\mathbf{I}. \tag{4.50}$$

4.4.4 Reducing computational load when there are more measurements than states

The measurements of a linear system are expressed as a linear combination of the states as in (4.15). In Section 4.4.1.4 I gave a system in which the measurements $\{\theta_m - \theta_{m-1}\}$ are a linear combination of a second, larger set of measurements, $\left\{\hat{\psi}_{jk} + \lambda_{jk}\right\}$. Therefore, the state is a linear combination of the second set of measurements. This makes one wonder whether the two systems using measurements $\{\theta_m - \theta_{m-1}\}$ and $\left\{\hat{\psi}_{jk} + \lambda_{jk}\right\}$ will give the same state estimates. The answer is that they do. In this Section I show how a state-space system with more measurements than states may be replaced by an equivalent system that has the same number of measurements as states. I prove that the systems are equivalent by showing that in each case the Kalman filter will produce the same sequence of error-covariance matrices and state estimates. Then I give an expression that approximates the fractional reduction in computation that the equivalent system gives.

The Kalman filter begins with an initial, *a priori* estimate of the state, $\hat{\mathbf{b}}_{k|k-1}$, and the error-covariance matrix,

$$\mathbf{P}_{k|k-1} = \mathrm{E}\left\{\left(\mathbf{b}_k - \hat{\mathbf{b}}_{k|k-1}\right)\left(\mathbf{b}_k - \hat{\mathbf{b}}_{k|k-1}\right)^{\mathrm{T}}\right\}. \tag{4.51}$$

The Kalman filter equations are shown in Table 5. The state estimate and the error-covariance matrix are propagated from each recursion to the next. Given an initial estimate of the error-covariance matrix and state, I show that the updated estimates of the two systems are the same. Therefore, by induction, the two systems are equivalent.

Table 5 Kalman filter equations

Compute error covariance inverse for updated estimate	$\mathbf{P}_{k\|k}^{-1} = \mathbf{P}_{k\|k-1}^{-1} + \mathbf{H}_k^{\mathrm{T}}\mathbf{V}_k^{-1}\mathbf{H}_k$
Compute Kalman gain	$\mathbf{K}_k = \mathbf{P}_{k\|k}\mathbf{H}_k^{\mathrm{T}}\mathbf{V}_k^{-1}$
Update state estimate	$\hat{\mathbf{b}}_{k\|k} = \hat{\mathbf{b}}_{k\|k-1} + \mathbf{K}_k\left(\mathbf{z}_k - \mathbf{H}_k\hat{\mathbf{b}}_{k\|k-1}\right)$
Project ahead	$\hat{\mathbf{b}}_{k+1\|k} = \mathbf{F}_k\hat{\mathbf{b}}_{k\|k}$ $\mathbf{P}_{k+1\|k} = \mathbf{F}_k\mathbf{P}_{k\|k}\mathbf{F}_k^{\mathrm{T}} + \mathbf{Q}_k$

4.4.4.1 A reduced-measurement system

Suppose we have a system given by $\mathbf{F}$, $\mathbf{Q}$, $\mathbf{z}_1$, $\mathbf{H}_1$ and $\mathbf{V}_1$ in which there are more measurements than states (i.e. $n > m$). Because $\mathbf{V}_1$ is positive definite there exists a non-singular $(n \times n)$ matrix, $\mathbf{S}$, such that

$$\mathbf{V}_1^{-1} = \mathbf{S}\mathbf{S}^{\mathrm{T}}. \tag{4.52}$$

This matrix is known as a **pre-whitening** matrix because it transforms a system into one with uncorrelated noise. From (4.52),

$$\begin{aligned} \mathbf{S}^{-1}\mathbf{V}_1^{-1}\mathbf{S}^{-\mathrm{T}} &= \mathbf{I} \\ &= \mathbf{S}^{\mathrm{T}}\mathbf{V}_1\mathbf{S}, \end{aligned} \tag{4.53}$$

where $\mathbf{I}$ is the identity matrix. Now suppose that $\mathbf{A}$ is the pseudo inverse of $\mathbf{S}^{\mathrm{T}}\mathbf{H}_1$ so that

$$\begin{aligned} \mathbf{A} &= \left(\mathbf{H}_1^{\mathrm{T}}\mathbf{S}\mathbf{S}^{\mathrm{T}}\mathbf{H}_1\right)^{-1}\mathbf{H}_1^{\mathrm{T}}\mathbf{S} \\ &= \left(\mathbf{H}_1^{\mathrm{T}}\mathbf{V}_1^{-1}\mathbf{H}_1\right)^{-1}\mathbf{H}_1^{\mathrm{T}}\mathbf{S}, \end{aligned} \tag{4.54}$$

$\mathbf{A}\mathbf{S}^{\mathrm{T}} = \left(\mathbf{H}_1^{\mathrm{T}}\mathbf{V}_1^{-1}\mathbf{H}_1\right)^{-1}\mathbf{H}_1^{\mathrm{T}}\mathbf{V}_1^{-1}$, and $\mathbf{A}\mathbf{S}^{\mathrm{T}}\mathbf{H}_1 = \mathbf{I}$. Pre-multiplying both sides of (4.15) by $\mathbf{A}\mathbf{S}^{\mathrm{T}}$ and dropping the subscript k gives

$$\begin{aligned} \mathbf{A}\mathbf{S}^{\mathrm{T}}\mathbf{z}_1 &= \mathbf{A}\mathbf{S}^{\mathrm{T}}\mathbf{H}_1\mathbf{b} + \mathbf{A}\mathbf{S}^{\mathrm{T}}\mathbf{v} \\ &= \mathbf{b} + \mathbf{A}\mathbf{S}^{\mathrm{T}}\mathbf{v}. \end{aligned} \tag{4.55}$$

This defines a new measurement system in which the measurement vector is $\mathbf{z}_2 = \mathbf{A}\mathbf{S}^{\mathrm{T}}\mathbf{z}_1$, the measurement matrix is $\mathbf{H}_2 = \mathbf{I}$ and the noise-covariance matrix is

$$\begin{aligned} \mathbf{V}_2 &= \mathbf{A}\mathbf{S}^{\mathrm{T}}\mathbf{V}_1\mathbf{S}\mathbf{A}^{\mathrm{T}} \\ &= \left(\mathbf{H}_1^{\mathrm{T}}\mathbf{R}_1^{-1}\mathbf{H}_1\right)^{-1}. \end{aligned} \tag{4.56}$$

The new measurement vector is length m. The two systems, defined by the measurement equations $\{\mathbf{z}_1, \mathbf{H}_1, \mathbf{V}_1\}$ and $\{\mathbf{z}_2, \mathbf{H}_2, \mathbf{V}_2\}$, are identical. We prove that the systems are identical by showing that the error covariance matrices and updated state estimates for both systems are the same.

4.4.4.2 Error-covariance matrix

From Table 5 the updated error-covariance matrix is

$$\mathbf{P}_{k|k}^{-1}(\mathbf{H}, \mathbf{V}) = \mathbf{P}_{k|k-1}^{-1} + \mathbf{H}^{\mathrm{T}}\mathbf{V}^{-1}\mathbf{H}, \tag{4.57}$$

where the subscript k has been dropped from $\mathbf{H}$ and $\mathbf{V}$. The updated error-covariance matrices for the two systems will be identical if

$$\mathbf{H}_1^{\mathrm{T}}\mathbf{V}_1^{-1}\mathbf{H}_1 = \mathbf{H}_2^{\mathrm{T}}\mathbf{V}_2^{-1}\mathbf{H}_2. \tag{4.58}$$

Expanding the right-hand side of (4.58) and using (4.56) gives

$$\begin{aligned} \mathbf{H}_2^{\mathrm{T}}\mathbf{V}_2^{-1}\mathbf{H}_2 &= \mathbf{V}_2^{-1} \\ &= \mathbf{H}_1^{\mathrm{T}}\mathbf{V}_1^{-1}\mathbf{H}_1. \end{aligned} \tag{4.59}$$

And so the updated covariance matrices for the two systems are identical.

4.4.4.3 State estimate

From the Kalman filter equations in Table 5 the updated state estimate is given by

$$\hat{\mathbf{x}}_{k|k}(\mathbf{H},\mathbf{V},\mathbf{z}) = \hat{\mathbf{x}}_{k|k-1} + \mathbf{K}(\mathbf{H},\mathbf{V})\big(\mathbf{z} - \mathbf{H}\hat{\mathbf{x}}_{k|k-1}\big), \tag{4.60}$$

where the subscript k has been dropped from $\mathbf{H}$, $\mathbf{V}$ and $\mathbf{z}$. The state estimates from the two systems are identical if

$$\mathbf{K}(\mathbf{H}_1,\mathbf{V}_1)\big(\mathbf{z}_1 - \mathbf{H}_1\hat{\mathbf{x}}_{k|k-1}\big) = \mathbf{K}(\mathbf{H}_2,\mathbf{V}_2)\big(\mathbf{z}_2 - \mathbf{H}_2\hat{\mathbf{x}}_{k|k-1}\big). \tag{4.61}$$

The right-hand side of (4.61) is given by

$$\begin{aligned}\mathbf{K}(\mathbf{H}_2,\mathbf{V}_2)\big(\mathbf{z}_2 - \mathbf{H}_2\hat{\mathbf{x}}_{k|k-1}\big) &= \mathbf{P}_{k|k}\mathbf{H}_2^{\mathrm{T}}\mathbf{V}_2^{-1}\big(\mathbf{z}_2 - \mathbf{H}_2\hat{\mathbf{x}}_{k|k-1}\big)\\ &= \mathbf{P}_{k|k}\big(\mathbf{H}_1^{\mathrm{T}}\mathbf{V}_1^{-1}\mathbf{H}_1\big)\mathbf{A}\mathbf{S}^{\mathrm{T}}\big(\mathbf{z}_1 - \mathbf{H}_1\hat{\mathbf{x}}_{k|k-1}\big) \qquad (4.62)\\ &= \mathbf{P}_{k|k}\mathbf{H}_1^{\mathrm{T}}\mathbf{V}_1^{-1}\big(\mathbf{z}_1 - \mathbf{H}_1\hat{\mathbf{x}}_{k|k-1}\big).\end{aligned}$$

And so the updated state estimates for the two systems are identical.

As a result of (4.59) and (4.62) the two state systems, $\{\mathbf{z}_1,\mathbf{H}_1,\mathbf{V}_1\}$ and $\{\mathbf{z}_2,\mathbf{H}_2,\mathbf{V}_2\}$ are identical if

1. there are more measurements than states in the first system,
2. $\mathbf{z}_2 = \mathbf{A}\mathbf{S}^{\mathrm{T}}\mathbf{z}_1$,
3. $\mathbf{H}_2 = \mathbf{I}$, which has the same dimension as the state vector, and
4. $\mathbf{V}_2 = \big(\mathbf{H}_1^{\mathrm{T}}\mathbf{V}_1^{-1}\mathbf{H}_1\big)^{-1}$.

4.4.4.4 Computation savings

The number of computations for one recursion of the Kalman filter is $O\big(2m^2n\big) + O\big(2mn^2\big) + O\big(m^3\big) + O\big(n^3\big)$. If $n = am$ where $a > 1$ then the number of computations can be written $O\big[\big(1 + 2a + 2a^2 + a^3\big)m^3\big]$. Using the equivalent system with $\mathbf{H}_2 = \mathbf{I}$, the number of computations becomes $O\big(3m^3\big)$. And so the number of computations for the system $\{\mathbf{H}_2,\mathbf{V}_2\}$ is $O\big[3/\big(1 + 2a + 2a^2 + a^3\big)\big]$ times the number for the system $\{\mathbf{H}_1,\mathbf{V}_1\}$. If, for example, $a = 2$ then $3/\big(1 + 2a + 2a^2 + a^3\big) = 0.14$ which is a significant computational saving.

4.4.5 Summary of the Kalman-filter-based array calibrator

A towed, flexible cylinder may be represented by a state-space formulation derived from a special solution of the Paidoussis equation known as the water pulley model. Given this representation, the Kalman filter is a powerful method of estimating the shape of the cylinder, or array. It can easily accommodate measurements from different sources, either synchronously or asynchronously. I have shown a way of fusing data from heading sensors and a self calibrator.

The state vector may be augmented to include the segments' x-positions. In this case the measurement equations must include calibrating signal measurements as heading sensors provide no information about the x-positions of the segments. I demonstrated how a general system with more measurements than states may be reduced to a system with a number of measurements equal to the number of states. The reduced system gives identical results to the original and has on the order of 0.14 times the number of computations per recursion of the Kalman filter.

Chapter 5 Comparison of Algorithms

5.1 Introducing the Self Calibrators

In this Chapter I examine and compare a variety of towed-array self calibrators. I give the assumptions, both explicit and implicit, made for each algorithm and, through computer simulations, determine how robust they are to variations in signal-source distribution and SNR. I explain the performance of the methods by relating the simulation results to the assumptions. The results of the simulations are used to investigate the sensitivity of the algorithms to the underlying assumptions.

For the first set of simulations, I arbitrarily chose a test array shaped as shown by the solid line in Figure 33, and explored the response of the methods to changes in signal-source distribution and SNR. In the second set of simulations the array shape and signal-source distribution were smoothly and randomly changing. I show the output from a beamformer using the estimated array-shape. This allows the effectiveness of the methods to be judged without bias due to choice of array shape or signal-source distribution.

The self calibrators investigated in this chapter can be *loosely* grouped into the following categories: a) broadband source [GM95a, Wah93], b) disjoint source [DM80, Dor78, Gor95c, MM88, MM92, RS86, RS87a, RS87b], c) eigenstructure [BMH91, GWR89, LM87], d) nonlinear minimisation [FW88, Lo88, TN88] and e) sharpness [Buc78, FGR92, Fer90a, Fer90b].

Unlike methods using narrowband signals, broadband-source methods assume the availability of a signal source with a spectrum that spans, say, a few hundred hertz. Disjoint-source methods rely on the assumption that the calibrating signal is separate from the other signals in time or frequency, so that estimating the phase delays between hydrophones of the calibrating signal proceeds on the basis that there is no interference from any other signal. This greatly simplifies towed-array self calibration because separating the contributions from multiple signals is one of its biggest problems. Disjoint sources may exist by the good fortune that the signals have different spectral lines.

Eigenstructure methods are narrowband methods which exploit properties of the array-covariance matrix. When all signals are incoherent with each other the eigenvectors of the array-covariance matrix form two orthogonal subspaces — the signal subspace and the noise

subspace. This is also the basis for the Multiple Signal Classification (MUSIC) DOA estimator [Sch79]. The eigenstructure method investigated in this chapter also assumes that signals are disjoint, but this is not necessarily the case for all eigenstructure methods.

Nonlinear minimisation methods typically involve a two-step iteration: first estimate DOA, then the relative sensor phases or sensor locations. Each step seeks to minimise a cost function which is generally nonlinear and therefore is an iterative process in itself. *A priori* estimates of high-SNR signal DOAs and sensor locations are required to initialise these methods, which are non-parametric in the sense that they proceed with no knowledge of geometric constraints such as the inter-hydrophone spacing.

The sharpness method starts by representing the array shape as a harmonic series. The parameters of this harmonic series are adjusted iteratively until a performance indicator known as sharpness is maximised. When sharpness is maximised it is assumed that parameters have been chosen such that the parameterised array shape matches the actual array shape as closely as possible.

In this chapter I assume that all hydrophones and signal sources are coplanar. Some of the methods I investigate were originally developed for the general case where there are no physical restrictions on sensor placement. In comparing methods this is taken into account and, I show that applying them to the more specific case of towed arrays does not affect the assumptions made in developing the algorithms. The array calibrators that will be investigated are:

1. time domain (Section 4.3)
2. phase difference self survey (PDSS) [Wah93]
3. least-squares error (Section 4.2)
4. self-cohering [Dor78, DM80]
5. redundant self-calibration [MM92]
6. eigenvector [GWR89, GR90, FGR92]
7. maximum likelihood [WF88]
8. sharpness [Buc78, Fer90b, HON77]

The chapter is structured as follows. Section 5.2 explains the theory of each and identifies implicit and explicit assumptions; Section 5.2.9 summarises these assumptions. The results of computer simulations are presented in Section 5.3 and are used to compare the performance of the various array calibrators.

5.2 The Calibrators Explained

Each of the methods I investigate is explained briefly. The penultimate goal of almost all array self calibrators is to determine the relative phases or times of arrival of a signal at each hydrophone. The chord approach of Section 2.5 is then used to obtain estimates of the hydrophone positions. The exceptions to this procedure are the maximum likelihood (Section

5.2.7) and the sharpness (Section 5.2.8) methods, which estimate the hydrophone positions directly.

5.2.1 A time-domain method

This method is described in Section 4.3. For the equations of (4.10) to be consistent with each other, the measured $\left\{\hat{T}_{jk}\right\}$ must always relate to one calibrating signal. In the presence of multiple signals, consistency is ensured by assuming that one source has greater power than any of the others so that its peak in the cross correlation is always dominant.

> An implicit assumption made in this method is that the spectrum of the calibrating signal source cannot consist of just a few spectral lines; the signal must be at least partially broadband to avoid ambiguous time-delay estimates.

5.2.2 Phase difference self-survey (PDSS) [Wah93]

This method revolves around frequency-wavenumber pictures which are commonly used to estimate bearing with linear equispaced arrays. A typical frequency-wavenumber diagram is shown in Figure 31(a). Rays beginning at the origin correspond to sources, and the slope of each line corresponds to the signal DOA. When the array is perturbed, phase errors cause the lines to be smeared in the wavenumber direction as in Figure 31(b). The PDSS method is iterative and is as follows:

1. Convert raw data from the hydrophones to the frequency-wavenumber domain using a 2D Fourier transform.
2. Apply a window to the data which is intended to capture the energy from one smeared source. Window position is determined by doing an incoherent average of the frequency-wavenumber data over frequency. The window is centred at the wavenumber bin corresponding to the peak of the incoherent average. The window width is chosen as the lesser of either the -10 dB points or two-thirds of the previous iteration's width.
3. Inverse Fourier transform the windowed data back to the frequency-distance domain. Make a maximum-likelihood estimate of the phase delay, $\theta_{m,m-1}(\omega_r)$, $2 \leq m \leq M$, at a given reference frequency, between every pair of adjacent hydrophones, where ω_r is the reference frequency. This is given as

$$\hat{\theta}_{m,m-1}(\omega_r) = \arg \max_{\theta_{\mathrm{m.m-1}}} \Re e\left\{\sum_{i=1}^{I}\left[g_{(m-1),i}\, g^{*}_{,im} \exp\left(j\theta_{m,m-1}\, u_i\right)\right]\right\} \tag{5.1}$$

where $\{g_m\}$ are the Fourier coefficients of the hydrophone signals, $\{z_m\}$, I is the number of frequency bins available, * represents complex conjugate, and $u_i = 1+\omega_i/\omega_r$. This step is identical to estimating time delay using a circular rather than a linear cross correlation.

Because of the circular cross correlation the estimate will be accurate only if the time delay is small compared to the length of the time series data.

4. The phase error relative to the first sensor is $\hat{\Theta}^i_{m,m-1}(\omega_r) = \hat{\Theta}^{i-1}_{m,m-1}(\omega_r) + \sum_{c=2}^{m} \hat{\theta}^i_{c,c-1}(\omega_r)$, where the superscript i refers to the current iteration and $\hat{\Theta}^0_{m,m-1} = 0$. The signals are delayed at each hydrophone by multiplying with $\exp\left(-j\hat{\Theta}^i_{m,m-1}u_i\right)$. This makes the calibrating source appear to be at broadside to the array while removing any smearing due to a perturbed array.
5. Repeat steps 2 to 4 until the window width reaches a predetermined value. Each time the width is reduced the filter rejects more of the interfering signals and noise while retaining the calibrating signal. Thus the phase- (time-) delay estimates become more accurate without the presence of interfering signals and noise.
6. The final values of $\hat{\Theta}^i_{m,m-1}$ are used to estimate the hydrophone positions. Wahl [Wah93] describes a procedure for estimating the hydrophone positions from the phase-delay estimates which assumes that the calibrating signal source appears on one side of the array only. This is not always realistic and so we use instead the chord approach described above.

Explicit assumptions (apart from those mentioned in Chapter 2) are: a) the sources radiate zero mean Gaussian random processes; b) there is constant inter-hydrophone spacing; c) the first and last hydrophones are on the x-axis; and d) the signal DOA is between 0 and π. Assumptions c) and d) can be dropped if the chord approach is used.

Implicitly, doing an incoherent average over frequency assumes that the calibrating signal-source is close to broadside (or the signal bandwidth is limited).

5.2.3 A least-squares error method [Gor95c]

This method is described in Section 4.2.

An implicit assumption used in this method is that the magnitude of the error in each estimate of phase difference, $\tilde{\theta}_{jk} = \tilde{\theta}_{j,j+1} + \ldots + \tilde{\theta}_{k-1,k}$, where the tilde indicates the estimation error, is less than π. If this error is $> \pi$ the integer multiple, p_{jk}, will be incorrect.

5.2.4 Self-cohering method [Dor78, DM80]

This method was developed and used on an experimental radar antenna array. No physical constraints were assumed, and so the method required at least two (not three because the signal DOAs are assumed to be known) narrowband sources to estimate the sensor locations. Turning on and off each source in turn, the phases of arrival of the narrowband signals are measured with respect to a reference directly at the hydrophones. The signal DOAs must be known in advance as well as *a priori* estimates of sensor position that are accurate to within half a wavelength

Figure 31 Typical frequency wavenumber diagrams for an array with 128 hydrophones and two signal sources; (a) array is linear, and (b) array has sinusoidal shape with an amplitude of 0.50 metres in the direction orthogonal to ship's motion.

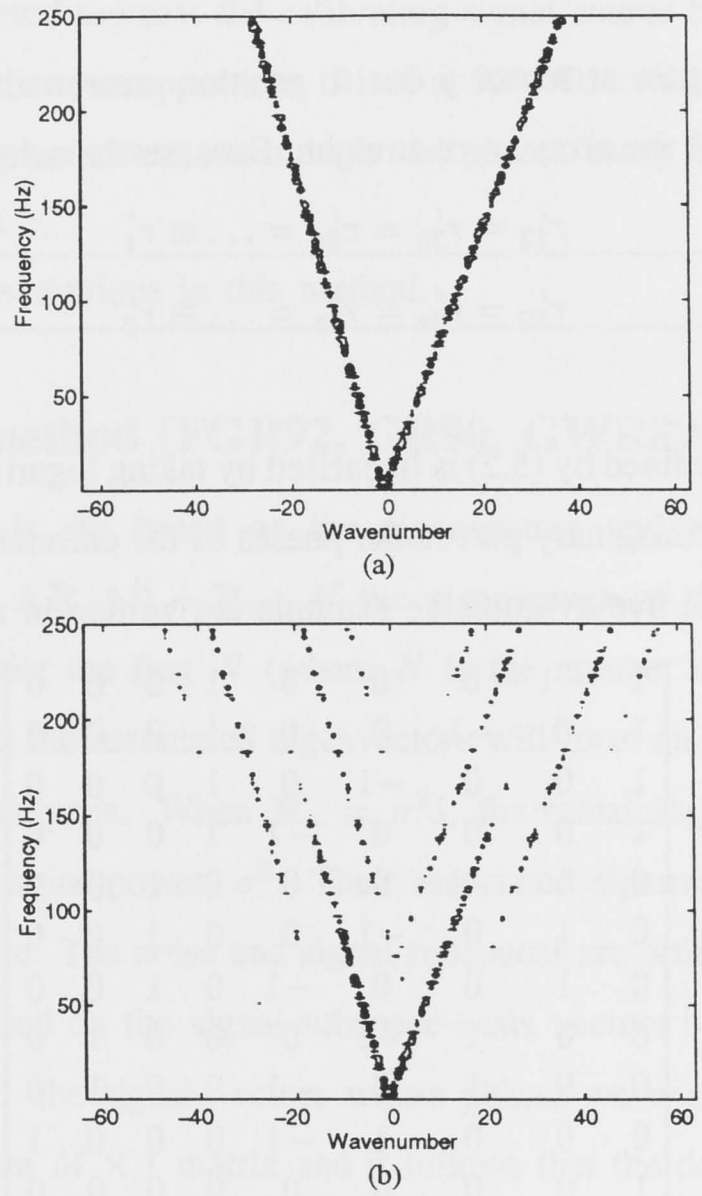

so that there is no phase ambiguity. Each signal DOA and the associated phases of arrival define a line on which the sensor, whose position is to be determined, must lie. Although only two calibrating sources are needed to estimate the sensor position, Dorny and Meagher [Dor78, DM80] use four to determine the LSE estimates of sensor position and a channel-dependent phase error. This method can be applied to towed arrays simply by using one calibrating signal and applying the chord approach.

The signal-to-noise ratio must be high to give reasonably accurate measurements of phases of arrival.

5.2.5 Redundant self-calibration method [MM92]

This method was originally applied to radio astronomy antenna arrays in which a turbulent atmosphere produces phase errors that are analogous to the position errors of towed arrays. The basis of redundant self-calibration is to recognise that a uniform array has many baselines of the same length. If a uniform array is straight then the correlations between every pair of sensors with identical baselines (i.e. sensors that are adjacent, one apart, two apart, etc.) will be equal.

The measured correlation between two sensors, j and k, is modelled as

$$r_{jk} = g_j g_k^* r'_{jk} \tag{5.2}$$

where g_j is the complex gain at sensor j due to position error, and r'_{jk} is the true correlation that would be measured if the array were straight. Because the array is redundant

$$\begin{aligned} r'_{12} = r'_{23} = r'_{34} = \ldots \equiv r'_1 \\ r'_{13} = r'_{24} = r'_{35} = \ldots \equiv r'_2 \\ \vdots \end{aligned} \tag{5.3}$$

The system of equations defined by (5.2) is linearised by taking logarithms and dividing into real and imaginary parts. The imaginary part is the phases of the correlations. The set of equations of the imaginary part for a five-hydrophone example are written in matrix form in (5.4).

$$\begin{bmatrix} \psi_{12} \\ \psi_{13} \\ \psi_{14} \\ \psi_{15} \\ \psi_{23} \\ \psi_{24} \\ \psi_{25} \\ \psi_{34} \\ \psi_{35} \\ \psi_{45} \\ \vartheta_r \\ \vartheta_s \end{bmatrix} = \begin{bmatrix} 1 & -1 & 0 & 0 & 0 & 1 & 0 & 0 & 0 \\ 1 & 0 & -1 & 0 & 0 & 1 & 0 & 0 & 0 \\ 1 & 0 & 0 & -1 & 0 & 1 & 0 & 0 & 0 \\ 1 & 0 & 0 & 0 & -1 & 1 & 0 & 0 & 0 \\ 0 & 1 & -1 & 0 & 0 & 0 & 1 & 0 & 0 \\ 0 & 1 & 0 & -1 & 0 & 0 & 1 & 0 & 0 \\ 0 & 1 & 0 & 0 & -1 & 0 & 1 & 0 & 0 \\ 0 & 0 & 1 & -1 & 0 & 0 & 0 & 1 & 0 \\ 0 & 0 & 1 & 0 & -1 & 0 & 0 & 1 & 0 \\ 0 & 0 & 0 & 1 & -1 & 0 & 0 & 0 & 1 \\ 1 & 0 & 0 & 0 & 0 & 0 & 0 & 0 & 0 \\ 1 & -1 & 0 & 0 & 0 & 0 & 0 & 0 & 0 \end{bmatrix} \times \begin{bmatrix} \theta_1 \\ \theta_2 \\ \theta_3 \\ \theta_4 \\ \theta_5 \\ \psi'_1 \\ \psi'_2 \\ \psi'_3 \\ \psi'_4 \end{bmatrix} \tag{5.4}$$

where ψ_{jk} is the phase of the measured correlation, ψ'_j is the phase of the true correlation and θ_m is the phase of the complex gain at sensor m. In the last two rows of the matrix the phase at hydrophone one is set equal to a reference phase, ϑ_r, and the phase difference between the first and second hydrophones is set equal to ϑ_s. The reference phase is typically set equal to zero, and ϑ_s is derived from a heading sensor placed on the array between the first and second hydrophones, which provides absolute information about the orientation of the array.

As in the LSE method of Section 4.2, the pseudo inverse matrix is used to give a least-squares error estimate of the gain phases, $\hat{\theta}_m$, and the true phases, $\hat{\psi}'_j$. A similar matrix equation may be derived for the real parts of the logarithms of (5.2) which gives estimates of the gain amplitudes. Note that the gain phases are not phases of arrival except for the case where there is only one signal (disjoint case). There is no attempt to estimate a signal DOA; it is assumed that the gain phases represent hydrophone position errors in the y-direction, which is equivalent to assuming that the signal source is at 90°. All the gain phases are assumed to be within $\pm\pi$ of each other. If, for example, an array is 100 m long and the signal wavelength is 6 m, a source need only be a few degrees off broadside before the end hydrophone's gain phase is

no longer $< \pi$, or $> -\pi$. Likewise, if the array is perturbed by more than half a wavelength in the y-direction, phase wrapping will occur. If the signals are disjoint and a DOA is known then the array may be steered towards the calibrating signal source by adjusting the phases of the correlations so that the source appears as if it is at 90°. To avoid the restrictions on source DOA and hydrophone displacements, we unwrap the phases using the same method as in the LSE method of Section 4.2.

There are no implicit assumptions in this method.

5.2.6 Eigenvector method [FGR92, GR90, GWR89]

Eigenstructure methods are based on the eigenvectors and eigenvalues of the array-covariance matrix, $\mathbf{R} = \mathbf{A}\mathbf{R}_s\mathbf{A}^{\mathrm{H}} + \mathbf{R}_n$. If the eigenvalues of this matrix are found and sorted into descending order the first N (where N is the number of signals) will be related to the incident signals and the associated eigenvectors will form an orthogonal basis for what is known as the signal subspace. When $\mathbf{R}_n = \sigma^2\mathbf{I}$, the remaining $M - N$ eigenvalues are equal to the uncorrelated noise power, σ^2. Their associated eigenvectors form an orthogonal basis for the noise subspace. The noise and signal subspaces are orthogonal to each other. The eigenvector method is based on the signal-subspace-basis vectors being a linear combination of the columns of $\mathbf{A}$ (i.e. the signal vectors whose phases we wish to know). For the case of only one signal, $\mathbf{A}$ is an $M \times 1$ matrix and it follows that the desired signal vector, $\mathbf{a}_1$, is simply a multiple of the eigenvector corresponding to the maximum eigenvalue, referred to as the **maximum eigenvector**. Having found this eigenvector, the relative phases can be found and the chord approach used to determine hydrophone positions.

The method is a disjoint one. The $\mathbf{A}$ matrix must have one column only for the signal vector to be a multiple of the maximum eigenvector. But, in practice, the method gives good results despite the presence of multiple signals and so it is worth looking into the method's behaviour. Consider the following. Assuming that there are two signal sources, then the maximum eigenvector of the array-covariance matrix, $\mathbf{e}_1$ is a linear combination of the signal vectors, $\mathbf{e}_1 = c_1\mathbf{a}_1 + c_2\mathbf{a}_2$. Then if λ is the corresponding maximum eigenvalue

$$\mathbf{R}(c_1\mathbf{a}_1 + c_2\mathbf{a}_2) = \lambda(c_1\mathbf{a}_1 + c_2\mathbf{a}_2); \tag{5.5}$$

but from (2.14) $\mathbf{R} = \sigma_1^2\mathbf{a}_1\mathbf{a}_1^{\mathrm{H}} + \sigma_2^2\mathbf{a}_2\mathbf{a}_2^{\mathrm{H}} + \sigma^2\mathbf{I}$, where σ_1^2 and σ_2^2 are the two signals' powers and assuming the signals are incoherent. And so

$$\begin{aligned} &\sigma_1^2 c_1\mathbf{a}_1\mathbf{a}_1^{\mathrm{H}}\mathbf{a}_1 + \sigma_2^2 c_2\mathbf{a}_2\mathbf{a}_2^{\mathrm{H}}\mathbf{a}_2 + \sigma_1^2 c_2\mathbf{a}_1\mathbf{a}_1^{\mathrm{H}}\mathbf{a}_2 + \\ &\sigma_2^2 c_1\mathbf{a}_1\mathbf{a}_2^{\mathrm{H}}\mathbf{a}_2 + \sigma^2 c_1\mathbf{a}_1 + \sigma^2 c_2\mathbf{a}_2 = \lambda(c_1\mathbf{a}_1 + c_2\mathbf{a}_2). \end{aligned} \tag{5.6}$$

If $\mathbf{a}_1$ and $\mathbf{a}_2$ are orthogonal, then $\mathbf{a}_2^{\mathrm{H}}\mathbf{a}_1 = \mathbf{a}_1^{\mathrm{H}}\mathbf{a}_2 = 0$. Also, $\mathbf{a}_1^{\mathrm{H}}\mathbf{a}_1 = \mathbf{a}_2^{\mathrm{H}}\mathbf{a}_2 = M$ and

$$\begin{aligned} \left(\sigma_1^2 M + \sigma^2\right) c_1 \mathbf{a}_1 + \left(\sigma_2^2 M + \sigma^2\right) c_2 \mathbf{a}_2 &= \lambda(c_1 \mathbf{a}_1 + c_2 \mathbf{a}_2) \\ c_1\left(\sigma_1^2 M + \sigma^2 - \lambda\right)\mathbf{a}_1 + c_2\left(\sigma_2^2 M + \sigma^2 - \lambda\right)\mathbf{a}_2 &= 0. \end{aligned} \tag{5.7}$$

There are three solutions to (5.7):

1. $\lambda = \sigma_1^2 M + \sigma^2 = \sigma_2^2 M + \sigma^2$, no constraint on c_1 and c_2. (i.e. the two sources have equal power)
2. $\lambda = \sigma_1^2 + \sigma^2, \quad c_2 = 0$, no constraint on c_1.
3. $\lambda = \sigma_2^2 + \sigma^2, \quad c_1 = 0$, no constraint on c_2.

Thus, if the signal powers are unequal and steering vectors $\mathbf{a}_1$ and $\mathbf{a}_2$ are orthogonal, the maximum eigenvector is a multiple of $\mathbf{a}_1$ or $\mathbf{a}_2$ rather than a linear combination of $\mathbf{a}_1$ and $\mathbf{a}_2$. This can be easily extended to more than two signal sources. If the conditions of orthogonality are not met, the maximum eigenvector will be a linear combination of the columns of $\mathbf{A}$. The array-shape estimates tend to be good nevertheless, because in practice the maximum eigenvector is composed *mostly* of the dominant signal's steering vector.

An implicit assumption of this method is that the signals are disjoint.

5.2.7 A maximum-likelihood approach [WF88]

The maximum-likelihood (ML) approach gives a unique solution if the array is coplanar but *not* collinear. The method seeks to minimise a nonlinear cost function, Q, defined as

$$Q \equiv \sum_{j=1}^{J} \left\| \mathbf{z}(j) - \mathbf{A}\mathbf{s}(j) \right\|^2 \tag{5.8}$$

where, from (2.13), $\mathbf{z}(j) = \mathbf{A}\mathbf{s}(j) + \mathbf{v}(j)$, j has been added to indicate the index of different snapshots and J is the number of snapshots. If an estimate of $\mathbf{A}$ is known and $\mathbf{z}(j)$ is measured at the hydrophone outputs, an estimate of $\mathbf{s}(j)$ can be obtained by linear regression:

$$\hat{\mathbf{s}}(j) = \left(\mathbf{A}^{\mathrm{H}}\mathbf{A}\right)^{-1}\mathbf{A}^{\mathrm{H}}\mathbf{z}(j). \tag{5.9}$$

An initial estimate of $\mathbf{A}$ is derived from *a priori* estimates of the number of signal sources, their directions of arrival and hydrophone positions. The ML approach has two steps, each is an iterative procedure. The two steps are iterated until Q converges to a minimum. (The ML method does not guarantee that this will be a global minimum; it may be a local minimum.) Step one aims to minimise Q with respect to the signal DOAs. The steering vector matrix, $\mathbf{A}$, is updated along with the DOAs. Each signal's DOA is updated separately, reviewing one DOA after another until Q arrives at a minimum given the best current estimates of hydrophone

positions. Step two minimises Q with respect to the hydrophone positions, and updates $\mathbf{A}$ with improvements to hydrophone position estimates. The cost function is minimised separately for each hydrophone using a closed-form solution (5.10) which gives the deviations of the hydrophones, Δx_m and Δy_m from their previous estimates.

$$\begin{bmatrix} \Delta x_m \\ \Delta y_m \end{bmatrix} = \left[\Re e\{\mathbf{B}_m^{\mathrm{H}}\mathbf{B}_m\}\right]^{-1} \Re e\{\mathbf{B}_m^{\mathrm{H}}\tilde{\mathbf{z}}_m\} \tag{5.10}$$

where

$$\begin{aligned} \mathbf{B}_m &= \frac{j\omega_0}{c_s}\begin{bmatrix} \sum_n \hat{\mathbf{A}}_{mn}\hat{s}_n(1)\cos\hat{\phi}_n & \sum_n \hat{\mathbf{A}}_{mn}\hat{s}_n(1)\sin\hat{\phi}_n \\ \vdots & \vdots \\ \sum_n \hat{\mathbf{A}}_{mn}\hat{s}_n(J)\cos\hat{\phi}_n & \sum_n \hat{\mathbf{A}}_{mn}\hat{s}_n(J)\sin\hat{\phi}_n \end{bmatrix} \\ \tilde{z}_m(j) &= z_m(j) - \sum_n \hat{\mathbf{A}}_{mn}\hat{s}_n(j) \\ \tilde{\mathbf{z}}_m &= [\,\tilde{z}_m(1) \quad \tilde{z}_m(2) \quad \cdots \quad \tilde{z}_m(J)\,]^T. \end{aligned} \tag{5.11}$$

The updates of the hydrophone positions are used to recalculate an estimate of the $\mathbf{A}$ matrix. In this manner Q is minimised until it converges for the current estimates of signal DOAs.

An implicit assumption is that there is more than one calibrating signal.

The reason for this assumption is that, without geometric constraints, it is not possible to estimate both x and y positions of a hydrophone with only one signal source. For the inverse in (5.10) to be solvable, $\Re e\{\mathbf{B}_m^{\mathrm{H}}\mathbf{B}_m\}$ must be non-singular. When there is only one signal source, $\Re e\{\mathbf{B}_m^{\mathrm{H}}\mathbf{B}_m\}$ is singular, and so there must be at least two calibrating signals. This method is a convoluted one involving a number of nonlinear minimisations, calculating such intermediates as the signal snapshots, $\hat{s}_n(k)$, and making no use of geometric constraints. Because of this we expect that the method will perform poorly in the presence of noise.

5.2.8 Sharpness method [Buc78, Fer90b, HON77]

This method is based on the assumption that the output from a beamformer will improve in some quantifiable sense as the estimated sensor positions become closer to the actual sensor positions. The output power, P_b, from a beamformer depends upon estimated hydrophone positions, $\{\chi_m\}$, and look direction, ϕ. Sharpness is defined as

$$S(\{\hat{\chi}_m\}) = \int_0^{\pi} P_b(\{\hat{\chi}_m\},\phi)^2 \sin\phi \, d\phi. \tag{5.12}$$

Sharpness is assumed to be a maximum when the estimated hydrophone positions assume their actual values. In [DC92] it is shown that sharpness does not necessarily become a maximum when the estimated array shape is equal to the actual shape. However, when the array shape is modelled as the sum of a harmonic series of sinusoidal shapes, then array-shape estimates from

the sharpness method are quite robust to changes of the signal-source distribution. In [Buc78, Fer90b] the array shape is parametrised in the form of a harmonic series

$$\hat{y} = \sum_{\lambda=1}^{\Lambda} [\alpha_\lambda \sin(\lambda \pi x / C_a) + \beta_\lambda \cos(\lambda \pi x / C_a)] \tag{5.13}$$

where $C_a = L_a + v_a T$, L_a is the length of the array, v_a is the towing vessel's velocity and T is the time over which the beamformer output is integrated. The coefficients, α_λ and β_λ may be found by maximising sharpness using a method explained in [Buc78]. Here, for the shape estimate, we use a single sinusoid with a variable wavelength as well as amplitude[2]. Rather than doing a two-dimensional search over amplitude and wavenumber for the maximum value of sharpness, a series of one-dimensional searches are used. Sharpness is maximised over amplitude, for fixed values of wavenumber from 3/8 to 1 5/8 in 1/32 increments where a wavenumber of one means the array has a shape with one complete sinusoid. Then the wavenumber/amplitude pair with maximum sharpness is chosen.

An implicit assumption of this method is that $S(\{\hat{\chi}_m\})$ is a maximum when $\{\hat{\chi}_m\} = \{\chi_m\}$.

5.2.9 Comparing assumptions

The purpose of this section is to provide a means of comparing the assumptions that are made in developing the array-shape-estimation methods. Assumptions that are common to every array calibrator outlined in this chapter are: a) all signals are zero mean, stationary and incoherent with each other; b) noise is zero mean, spatially uncorrelated and uncorrelated with the signals; c) the array shape changes slowly enough to be assumed unchanging; d) hydrophones are joined by straight-line segments of cable (this assumption is not made for the ML approach of Section 5.2.7); and e) signal sources are far field with planar wavefronts, i.e. non-dispersive propagating medium. A summary of the method-specific explicit and implicit assumptions is shown in Table 6.

5.3 Simulations and Results

In this section I present the results of computer simulations. Simulated data were generated as follows:

1. The array used in the simulations has a quartic shape in the y-direction with respect to x, with a maximum displacement from the x-axis of 0.67.
2. There are 32 hydrophones with a uniform inter-hydrophone spacing of 1.
3. The speed of sound in water is 1500 ms^{-1}.

---

[2] This technique was explained in a personal communication from B. G. Ferguson.

TABLE 6

Comparison of explicit and implicit assumptions.

Method	Explicit Assumptions	Implicit Assumptions
Time Domain	Broadband sources. One signal source is dominant.	Signal source is Gaussian noise process.
Phase Difference Self Survey	Broadband sources. Signal source is Gaussian noise process. Constant inter-hydrophone spacing.	Calibrating source is at or close to broadside.
Least-Squares Error	Narrowband sources. Sources are disjoint. Inter-hydrophone distance is less than half a wavelength.	Magnitude of phase difference errors is less than π.
Self-Cohering	Narrowband sources. Sources are disjoint. Inter-hydrophone distance is less than half a wavelength.	Signal-to-noise ratio is high.
Redundant Self-Calibration	Narrowband Sources. Sources are disjoint. Inter-hydrophone distance is less than half a wavelength.	None
Eigenvector Method	Narrowband sources. Sources are disjoint.	If sources aren't disjoint, one signal is dominant.
Maximum-Likelihood Approach	Narrowband sources. Have *a priori* estimates of sensor positions. Have *a priori* estimates of the number of signal sources and their DOAs.	There are at least two signal sources.
Sharpness	Sharpness is maximized when the estimated sensor positions are correct.	When the parametrized array shape comes closest to the actual array shape the sharpness will be a maximum.

4. Narrowband processing is done at the design frequency which is 250 Hz for the simulated array.
5. Raw data are sampled at a frequency of 10 kHz.
6. The number of time samples from each hydrophone is 1024. Each algorithm uses the same number of data points.
7. Signal sources lie in the same plane as the array.
8. Simulations with multipath signals have one direct, and one reflected, path signal. The reflected signal has azimuth DOA the same as the direct path with elevation 10° above horizontal. The amplitude of the reflected signal is half that of the direct path signal.

TABLE 7

RMS position error (metres) and mean direction error (degrees) for various distributions of signal sources. RMS position errors which are greater than one-tenth of the wavelength at the design frequency are shown in boldface.

Scen-ario	Signal Sources	SNR (dB)	Time Domain	PDSS	Least Squares	Self Cohere	Redund. Self Cal	Eigen-vector	ML	Sharp-ness
1	90°	50	2.9×10^{-3}	4.0×10^{-3}	7.0×10^{-6}	1.3×10^{-3}	1.3×10^{-4}	7.0×10^{-6}	-	0.11
	1		0.17°	2.8e-3°	4.3e-4°	6.3e-2°	-	4.3e-4°	-	-
2	90°	10	2.9×10^{-3}	4.3×10^{-3}	8.0×10^{-4}	**0.28**	1.1×10^{-2}	8.0×10^{-4}	-	0.11
	1		0.22°	2.8e-3°	3.3e-2°	5.1°	-	3.3e-2°	-	-
3	90°	-5	**0.33**	0.15	4.0×10^{-3}	**9**	7.3×10^{-2}	4.0×10^{-3}	-	0.11
	1		1.0°	0.15°	0.24°	33°	-	0.24°	-	-
4	90°	-20	**9**	**14**	0.17	**15**	**0.83**	2.7×10^{-2}	-	0.11
	1		33°	47°	4.3°	60°	-	1.1°	-	-
5	70°	50	2.7×10^{-3}	3.7×10^{-3}	7.3×10^{-6}	1.4×10^{-3}	0.11	7.3×10^{-6}	-	0.11
	1		0.25°	0.11°	2.7e-4°	7.7e-2°	-	2.7e-4°	-	-
6	10°	50	0.12	0.17	5.7×10^{-5}	2.9×10^{-2}	**2.9**	5.7×10^{-5}	-	**2.1**
	1		8.6e-2°	0.36°	1.4e-3°	0.19°	-	1.4e-3°	-	-
7	3°	50	**0.31**	0.20	**0.57**	**0.57**	**3.3**	**0.57**	-	**2.1**
	1		0.65°	0.51°	1.0e-3°	0.32°	-	1.0e-3°	-	-
8	90°,45°	50	2.7×10^{-3}	1.3×10^{-2}	5.3×10^{-3}	0.10	0.11	5.7×10^{-3}	5.0	0.11
	1, 0.2		0.17°	2.8e-3°	0.36°	7.2°	-	0.38°	3.0°	-
9	90°,45°	50	3.0×10^{-3}	4.7×10^{-2}	**0.37**	**0.43**	**0.31**	1.9×10^{-2}	2.2	0.11
	1, 0.5		0.26°	2.8e-3°	13°	20°	-	1.2°	2.2°	-
10	90°,45°	50	3.0×10^{-3}	0.12	**0.37**	**1.1**	**1.5**	0.10	2.1	0.11
	1, 0.8		0.26°	2.8e-3°	13°	36°	-	3.8°	2.2°	-
11	90°,45°	50	**14**	**8.3**	**8.0**	**2.6**	**1.0**	**2.7**	2.3	0.11
	1, 1		13°	2.8e-3°	26°	47°	-	47°	1.8°	-
12	90°,45°	10	**0.40**	0.12	**0.37**	**6.7**	**1.0**	0.10	**1.3**	0.11
	1, 0.8		0.84°	2.8e-3°	13°	39°	-	3.8°	1.6°	-
13	90°,45°,120°	50	7.0×10^{-3}	0.12	**0.37**	**8.7**	**1.6**	0.10	1.2	0.11
	1, 0.8, 0.2		0.35°	2.8e-3°	13°	9.1°	-	3.9°	1.2°	-
14	90°,45°,120°	50	**19**	**27**	**5.7**	**8.3**	**2.1**	**8.7**	1.1	0.11
	1, 0.8, 1		13°	120°	9.3°	35°	-	10°	0.86°	-
15	90°,45°,120, 150°	50	**0.26**	**3.7**	**6.7**	**12**	**3.3**	0.13	1.1	0.11
	1, 0.8, 0.8, 0.5		0.75°	0.58°	9.6°	86°	-	5.7°	1.6°	-
16	90°,45°,120°, 150°	50	**9.0**	**8.7**	**2.4**	**13**	**1.1**	**24**	1.6	0.11
	1, 0.8, 0.8, 1		1.5°	1.8°	7.0°	2.6°	-	150°	3.0°	-
17	45°,140°	50	**10**	2.5×10^{-2}	**6.0**	**15**	**2.1**	**10**	2.8	0.11
	1, 1		6.2°	0.80°	21°	45°	-	42°	3.5°	-
18	90°,90°*	50	4.0×10^{-3}	5.3×10^{-3}	1.2×10^{-3}	1.5×10^{-3}	1.2×10^{-2}	1.2×10^{-3}	1.3	0.11
	1, 0.5		0.26°	2.8e-3°	3.8e-2°	5.0e-2°	-	3.8e-2°	0.14°	-
19	90°,90°*,45°	50	3.7×10^{-3}	3.1×10^{-2}	**6.3**	**1.9**	**0.93**	**0.43**	0.77	0.11
	1, 0.5, 0.8		0.26°	0.30°	20°	0.17°	-	36°	0.29°	-
20	40°,30°	50	8.7×10^{-2}	**0.22**	**0.25**	**0.31**	**0.93**	**0.21**	0.87	0.11
	1, 0.8		2.0°	0.42°	3.7°	4.0°	-	0.94°	2.1°	-
21	10°	-5	**1.5**	**3.0**	7.3×10^{-2}	**21**	**2.8**	6.7×10^{-2}	-	**2.1**
	1		7.5°	24°	0.79°	88°	-	0.79°	-	-

A number of possible scenarios are presented in Table 7 in which the following parameters are adjusted:

source bearings – up to four signal sources placed in the far field in any direction from 0° to 180°.

source amplitudes – the relative signal strengths of each source.

signal-to-noise ratio – measured relative to the strongest signal source. The SNR of the signals is the same for both the narrowband and the broadband simulations. This circumvents the problem of comparing data that have different time-bandwidth products.

For each scenario the methods are run ten times using different noise each time and the results are averaged. Table (7) shows the following results:

direction-estimation error – Incorrectly estimating the DOA of the calibrating signal source results in the estimated array shape's being rotated about the origin by the direction-estimate error. This affects the direction-estimation accuracy of the beamformer. Two of the methods, the redundant self-calibration and sharpness methods, do not estimate the DOA of the calibrating source and so the direction-estimate error is not given for these methods.

RMS position error – normalised, is calculated by first correcting for the direction-estimate error. In other words this is an indication of how well the method will estimate the *shape* and not the orientation of the array.

As a rough guide, an RMS position error of up to 0.2 (or one-tenth of a wavelength at the design frequency) is acceptable in terms of the beamformer output that it gives. A method is deemed to have failed to estimate shape if the RMS position error is greater than this amount, and this is indicated in Table 7 by bold type. Figure 32 shows the mean time taken for each method to estimate the array shape given 1024 samples of raw data. Simulations were performed using Matlab on a SPARC 10 workstation. For the reasons outlined in Section 5.2.7, the ML method is not simulated when only one source is used. The performance of each method is discussed in greater detail below.

Figure 32 Time taken to estimate array shape from 1024 samples of raw data.

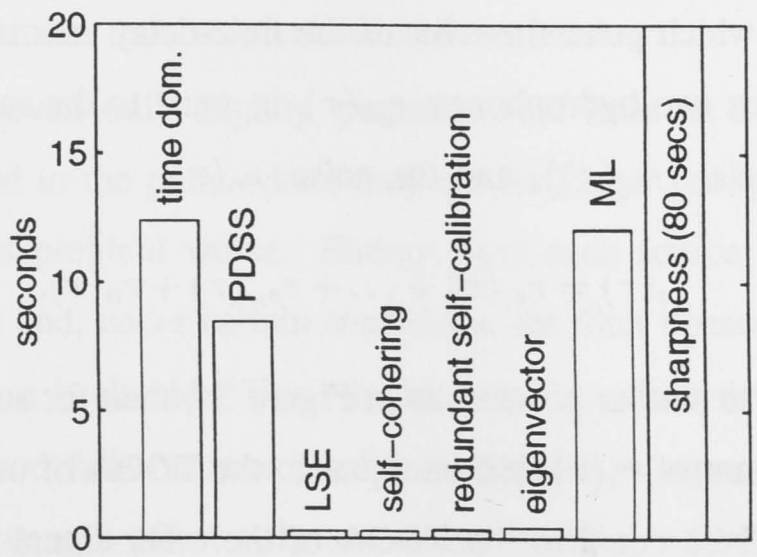

Figure 33 Array calibration results – actual array shape (solid line) estimated array shape (asterisks); (a) time-domain method, scenario 3; (b) PDSS method, scenario 6; (c) self-cohering method, scenario 8; (d) redundant self-calibration method, scenario 6; (e) eigenvector method, scenario 19; (f) maximum-likelihood method, scenario 11; (g) maximum-likelihood method, scenario 12; (h) sharpness method, scenario 1.

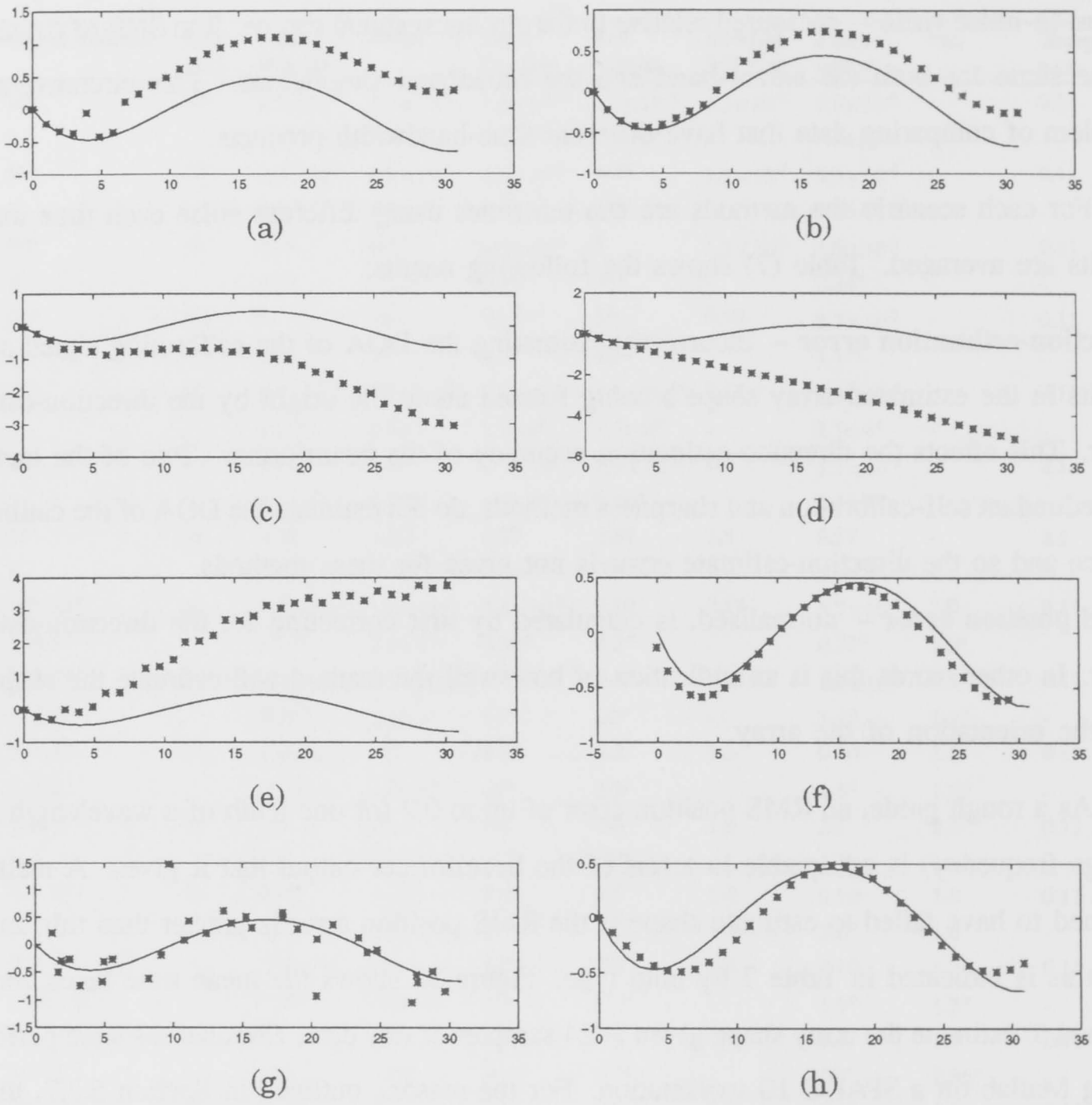

(a) (b) (c) (d) (e) (f) (g) (h)

5.3.1 Time-domain method

The time-domain method relies on cross correlation to estimate time delay. Because a time-delay estimate is obtained from the argument of a maximum value rather than the maximum itself, its accuracy will be good unless either the noise or an interfering signal becomes too strong, at which point the error of the time-delay estimate increases rapidly. The cross correlation between two hydrophones, $r_{jk}(\tau)$, is equal to the sum of the individual cross correlations of the signals, $\{r_{s_n}(\tau)\}$, and the noise, $r_n(\tau)$,

$$r_z(\tau) = r_{s_1}(\tau) + \ldots + r_{s_N}(\tau) + r_n(\tau). \tag{5.14}$$

If two of the signals have similar powers, as in Figure 34, then for some hydrophone pairs the argument of the maximum of $r_z(\tau)$ will be equal to the TDOA of one signal, while for other hydrophone pairs it will be equal to the TDOA of the other signal. When TDOA estimates

that correspond to the same signal for each hydrophone pair cannot be obtained, large RMS hydrophone-position errors will occur.

Figure 34 Detail of a typical cross correlation with two signal sources.

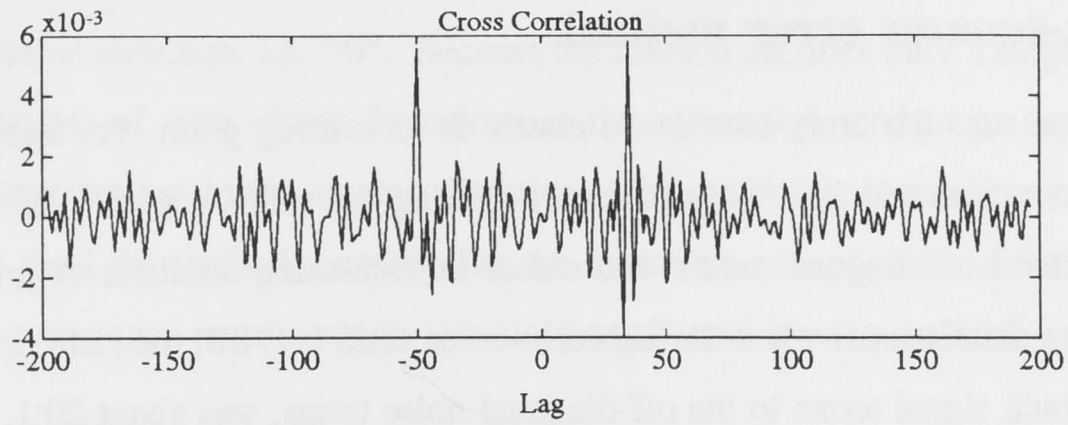

The reliability of the time-delay estimation can be seen in scenarios 1, 2, 5 and 8–10, where the RMS position error is consistently low. In scenarios 3, 4 and 11 the RMS position errors are large due to either high noise or a strong interfering source. The noise is just beginning to affect the position estimates in scenario 3 (as shown in Figure 33(a)). The method works equally well when sources are correlated. (see scenarios 18 and 19) assuming that the reflected-path signals have smaller amplitudes than the direct-path signals. Their peaks will appear in a cross correlation, but the amplitude of the peaks corresponding to the multipath signals will still be smaller than the peak corresponding to the true time delay, because the amplitude of the reflected signal will be smaller than the amplitude of the direct signal.

5.3.2 Phase difference self-survey (PDSS)

This method relies on a spatial filter to capture the calibrating source and separate it from the interfering sources and noise. Because the frequency-wavenumber diagram is incoherently averaged along the frequency axis, the filter is predisposed towards signal sources that are close to broadside. Equation (5.1) is equivalent to the time-delay estimation used in the time-domain method. The PDSS method is shown to fail at very low signal-to-noise ratios such as in scenario 4 where the SNR$=-20$ dB. The performance of the PDSS method is better than the time-domain method because the filter can reduce interference from noise.

When the array is even only slightly perturbed, the lines in a frequency wavenumber diagram become smeared to the point where they are no longer recognisable as lines. Spatial aliasing only makes this problem worse. Energy from each source tends to become spread evenly over the diagram and, under certain conditions, the filter cannot separate the calibrating and interfering sources as it should. Thus, in scenario 11, when there are two equal-power signal sources, the method fails because the filter is unable to separate the two. An error in estimating one time delay will affect only one sensor-position estimate. Therefore, when the

method begins to fail there will typically be two sub-arrays which have their shapes accurately estimated but which are not correctly positioned with respect to each other. See Figure 33(b) which shows a shape estimation for scenario 6.

5.3.3 Least-squares error method

This method uses the array-covariance matrix as its starting point. For uncorrelated noise, the noise-covariance matrix is $\sigma^2\mathbf{I}$. In practice, off-diagonal terms appear. The variance of the magnitude of these off-diagonal terms diminishes as increasing numbers of time samples are taken. For these simulations, when the signal-to-noise ratio is 0 dB, the ratio of the magnitude of the off-diagonal signal terms to the off-diagonal noise terms, was about 20:1, with the result that the least-squares error method is relatively insensitive to noise (as are all methods which use the array-covariance matrix), as the only terms in the array-covariance matrix which affect the array-shape estimates are the off-diagonal terms. The effects of noise don't become significant till the signal-to-noise ratio reaches -20 dB.

Being a disjoint method it was not surprising that it failed when a second signal source was added, although, as can be seen in scenario 8, the method was successful when the second source had only a small amplitude. The phase-difference measurements are taken directly from the elements of the array-covariance matrix and so the method tends to perform gradually worse as noise is added. Compare scenarios 1–4 in which the noise increases, with the time-domain method which uses the *argument* of the maximum of a cross correlation and performs consistently well up to a point at which it suddenly fails.

5.3.4 Self-cohering method

With no procedure for reducing the error on phase measurements, this method suffers badly from noise. At only 10 dB, as in scenario 2, the results show significant hydrophone position errors. Similarly, the method fails as soon as an interfering source is introduced. The estimation results for scenario 8, in which a second signal source with amplitude of 0.2 is introduced, is shown in Figure 33(c).

5.3.5 Redundant self-calibration

This method assumes that there is a calibrating signal source in the direction in which the array is steered. The estimated phases of arrival at the hydrophones are modelled as sensor position deviations in the steered direction which, in these simulations, is broadside. As the calibrating signal source moves away from the steered direction, the hydrophone position errors increase. This is seen in scenarios 5–7, and Figure 33(d) which shows the results of scenario

6. In practice the array can be steered towards the strongest source by using information from the last beamformer output.

Although the method assumes the signals are disjoint it works when a second or even third source is present, such as in scenarios 8–10 and 12–13. In these cases there is still a signal source in the steered direction, i.e. 90°. Because the method ascribes only a single error to each sensor, the estimates of array-shape deviations in the y-direction tend to be insensitive to the signal sources that are not in the steered direction. The method is insensitive to noise for the same reason as the LSE method, namely that the measurements of phase difference are taken from the array-covariance matrix which is mainly unaffected by uncorrelated noise.

5.3.6 Eigenvector method

This method begins with the array-covariance matrix and so, for the same reasons given in Section 5.3.3, the eigenvector method is insensitive to noise. Degradation in performance is not significant till less than -20 dB SNR. The assumption that the maximum eigenvector of the array-covariance matrix is a multiple of the calibrating signal vector, $\mathbf{a}_1$, is true, in general, only for the case of one signal source. When there is more than one source the maximum eigenvector will be a linear combination of all the signal vectors, $\{\mathbf{a}_n\}$. However, the method is fairly robust with respect to the presence of interfering sources. As an example, compare scenarios 10 and 20 which are identical in all respects except for the location of the signal sources. The ratio of signal source strengths hasn't changed, yet moving the sources away from broadside has an adverse effect on the method's performance.

The SNR has an effect on performance that is related to signal source direction. Consider scenarios 6 and 21 where a single source is located at 10°. Scenario 6 with a signal-to-noise ratio of 50 dB has an RMS position error of 5.7×10^{-5} whereas scenario 20, with a signal-to-noise ratio of -5 dB, has an RMS position error of 0.21. Yet when the source is at 90°, as in scenarios 1 and 3, the effect of noise is not nearly so great. Scenario and 19 demonstrates the eigenvector method's inability to cope with correlated signals. When two signals are impinging on an array and one is just a delayed version of the other then the array-covariance matrix will have only one signal subspace eigenvector given by

$$\mathbf{e}_1 = |s_1|\mathbf{a}_1 + |s_2|\mathbf{a}_2 \exp(j\psi) \tag{5.15}$$

where $\exp(j\psi)$ is a delay term. When the direct- and reflected-path signals arrive from different directions, the two vectors $\mathbf{a}_1$ and $\mathbf{a}_2$ will be linearly independent and the maximum eigenvector will give a distorted array-shape estimate. Figure 33(e) shows the results of a shape estimation where a multipath signal appears from 90° with a reflected version coming from 10° above the horizontal plane.

5.3.7 Maximum-likelihood (ML) approach

Some methods require that there be no more than one signal source to be able to estimate phases or times of arrival, whereas some are capable of working whether there is one signal source or many. The ML approach is unusual because it requires *at least* two signal sources. As explained in Section 5.2.7, this stems from the fact that the matrix, $\Re e\{\mathbf{B}_m^{\mathrm{H}}\mathbf{B}_m\}$, in (5.10) is singular when there is only one signal source. Hence no results are given for situations in which there is only one signal source.

The *a priori* estimates of hydrophone positions are obtained by randomly perturbing the actual hydrophone positions in the x- and y-directions. The standard deviation of the perturbations is one fifth of the inter-hydrophone distance in both the x- and y-directions. *A priori* estimates of signal source directions are taken in the above manner using a standard deviation of 4°. The number of sources is correctly known in the simulations; I don't analyse the sensitivity of this method to errors in the estimate of the number of sources. The *a priori* estimates of the signal sources' DOAs and sensor positions need to be fairly accurate. The quadratic error function given in (5.8) is $Q \equiv \sum_{j=1}^{J} \|\mathbf{z}(j) - \mathbf{A}\mathbf{s}(j)\|^2$. Figure (35) shows a plot of Q versus DOA estimate error, ϕ, when the sensor positions are known exactly and there is a single source at 90°. As can be seen, if the *a priori* DOA estimate error is $> \sim 5°$ the method will converge to a local minimum rather than the global minimum. The method consistently has an RMS position error in the range 3 to 7 m. Although this is large, it is due mostly to systematic lateral displacements of the hydrophones, and the array-shape estimate is quite good. The array-shape-estimate results from scenario 11 are shown in Figure 33(f). The ML method does not apply physical constraints and so there is no reason for it to maintain inter-hydrophone distances to their known values. Figure 33(f) shows the estimated array-shape shrinking along the x-direction.

The ML method performs poorly in the presence of noise. Figure 33(g) shows the results of scenario 12 with the same two sources as scenario 10 but with a signal-to-noise ratio of 10 dB. The results from 10 are similar to those in Figure 33(f) yet the addition of some noise in scenario 12 causes the method to fail.

Figure 35 Quadratic error function, Q, versus DOA estimate.
Sensor locations are known exactly and source DOA = 90°.

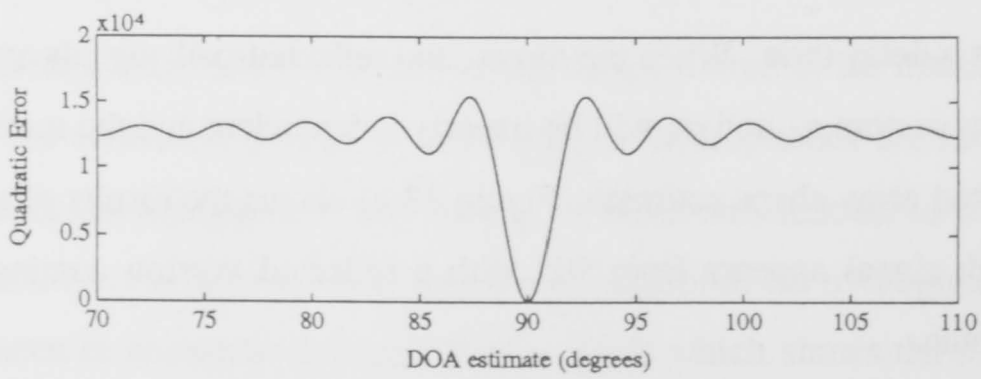

5.3.8 Sharpness method

Obviously when the estimated array-shape can only be a sinusoid and the actual shape is arbitrary, the sharpness method will not produce the accurate results that can be obtained with other methods, hence the relatively high values of hydrophone position errors that are seen in Table 7. Figure 33(h) shows that the estimated array shape approximates the actual shape as far as a sinusoid can. In spite of the large hydrophone position errors, Figure 36 shows that the calibrated beamformer output has easily observable peaks corresponding to the signal sources.

Of the methods examined here the sharpness method is the only one which gives workable results in almost all cases, but it has one serious drawback in that large errors in direction estimation can be observed in the beamformer output. The sharpness method estimates the array shape with no notion of the true orientation of the array. Even if a heading sensor is placed on the cable and the estimated array shape is rotated so that it matches the information obtained from the heading sensor, the orientation of the array will still cause direction estimation errors. This method takes the longest to run. It involves 41 one-dimensional maximisations, each of which calculates beamformer output about 12 times. For an array that requires more parameters in the shape estimate, the number of calls to the beamformer procedure would rise sharply, thereby lengthening the time required for an estimate.

Figure 36 Array calibration results for scenario 1; sharpness method. Continuous and dashed lines represent uncalibrated and calibrated beamformer output respectively.

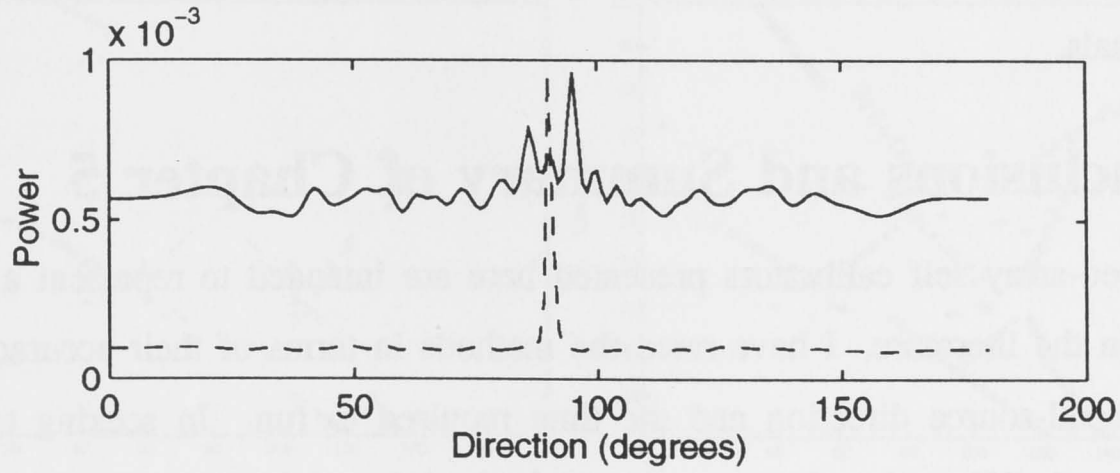

5.3.9 Continuous simulation with beamformer output

Quality of the beamformer output is what we are ultimately trying to achieve. As Figure 33(f) and 36 show, the RMS position error does not give a true indication of how the beamformer will perform. In this section I simulate an array shape that is continually changing, with signal sources that are also changing in amplitude and DOA. In total there are 100 shape estimates and beamformer outputs calculated for each method. These are displayed in Figures 38 and 39 in the form of contour plots, where the contours are lines of equal power. A plot of the ideal beamformer output is shown in Figure 37. The main track, beginning at 35° and finishing at 134°, has a constant amplitude of 1. It is shadowed by a multipath reflected source which

Figure 37 Continuous simulation — ideal beamformer output.

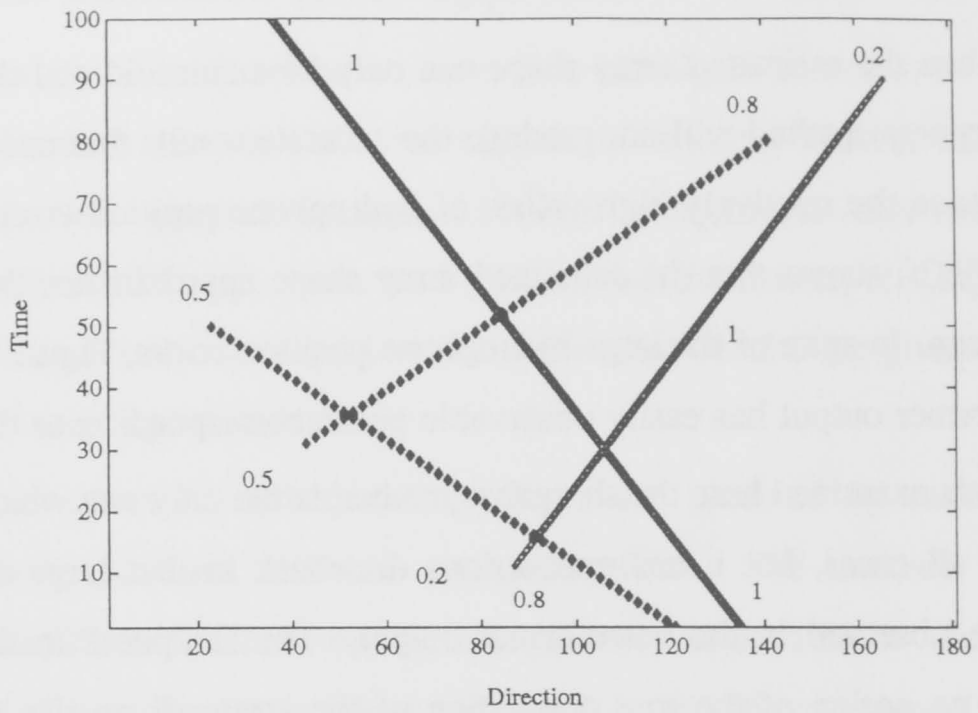

arrives from an angle 10° above the direct path source. The reflected signal has a constant amplitude of 0.5. The other signal sources that can be seen have no multipath components. Their amplitudes, which vary in time from 0.2 to 1, are shown at various points on Figure 37. The SNR is set to 5 dB.

The best methods are the PDSS followed closely by the time domain. The distinguishing factor is that they are broadband methods. The sharpness method produces clean beamformer output but it can be seen that the DOA estimation error is quite large. The eigenvector method has fairly clean beamformer output but its performance is not so good in the presence of multiple signals.

5.4 Conclusions and Summary of Chapter 5

The towed-array self calibrators presented here are intended to represent a cross-section of methods in the literature. I have rated the methods in terms of their accuracy to estimate shape and signal-source direction and the time required to run. In seeking to characterise performance and differentiate between the methods, I have also investigated the robustness of each method to variations in signal-source distribution and noise characteristics. Explicit and implicit assumptions were given, and the sensitivity of the methods to the underlying assumptions was determined through simulations which violated the assumptions. The results of these simulations have been summarised in Table 7.

The time-domain and the PDSS methods perform the best in the presence of coherent signals while the eigenvector and sharpness methods perform the best at low SNRs. The continuous simulations of Section 5.3.9 show that the performance of the other methods was unsatisfactory. The time-domain and PDSS methods are both broadband methods and this seems to be the differentiating factor for overall success or failure with coherent signals.

Figure 38 Continuous simulation, (a) time-domain method, (b) PDSS method, (c) least-squares error method, (d) self-cohering method.

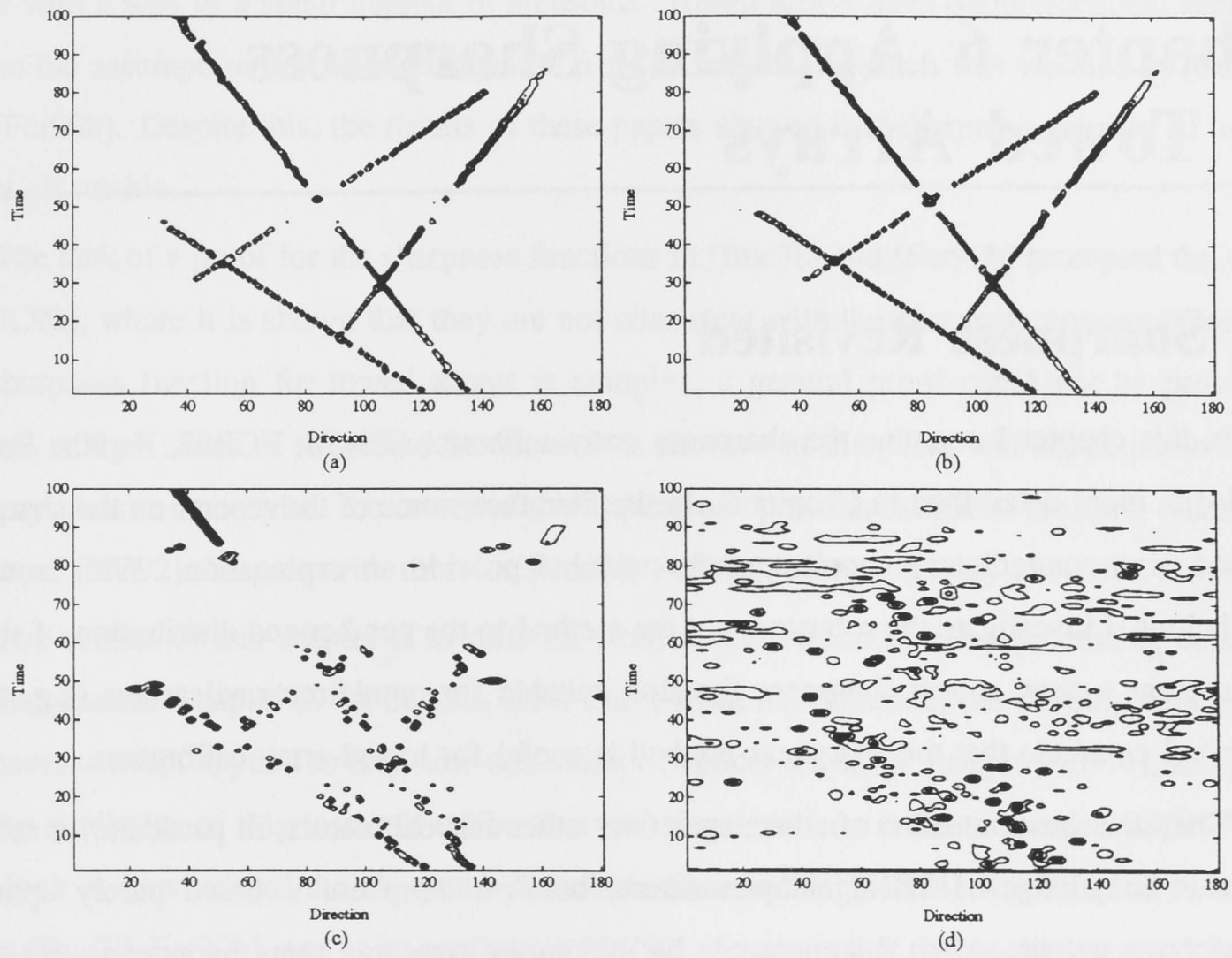

Figure 39 Continuous simulation, (a) redundant self-calibration method, (b) eigenvector method, (c) maximum-likelihood method, (d) sharpness method.

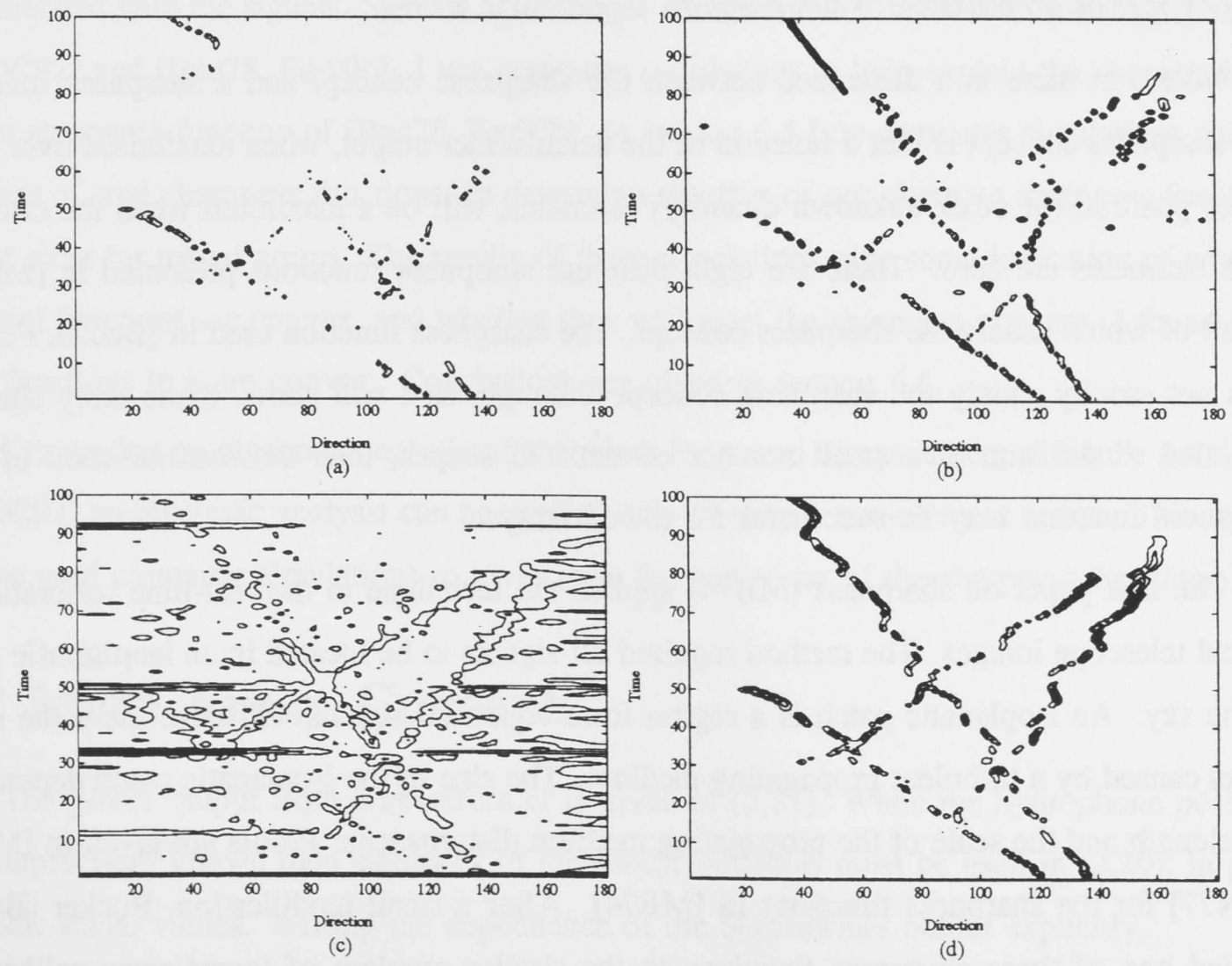

Chapter 6 Applying Sharpness to Towed Arrays

6.1 Sharpness Revisited

In this chapter I examine the sharpness array calibrator [Buc78, FGR92, Fer90a, Fer90b, MB74] in more detail than in Chapter 5. In the literature, some of the reports on the sharpness method give contradictory conclusions for which I provide an explanation. With computer simulations, I investigate the robustness of the method to the number and distribution of signals and present a new, robust sharpness function suitable for omnidirectional arrays (e.g. towed arrays). I conclude that the sharpness method is useful for towed-array calibration.

Sharpness has a number of advantages over other self calibrators; in particular, it requires no prior knowledge of the signal parameters, because sharpness is based purely upon the beamformer output. Also, sharpness can be maximised over any array parameters that affect the beamformer output. For instance, this could be some arbitrary parameterisation of the array-shape, or an estimate of the range to a particular source.

Note that there is a difference between the sharpness concept and a sharpness function. The sharpness concept is that a function of the beamformer output, when maximised over some sensor position (or other unknown quantity) estimates, will be a maximum when the errors of these estimates are zero. There are eight different sharpness functions presented in [MB74], not all of which satisfy the sharpness concept. The sharpness function used in [Buc78, Fer90b] does not strictly satisfy the sharpness concept although, as I will show, if the array shape is modelled as the sum of a small number of sinusoid shapes, then the maximisation of their sharpness function may be successful for towed arrays.

The first paper on sharpness [MB74] applied the technique to the real-time restoration of optical telescope images. The method required all signals to be located in an **isoplanatic** patch of the sky. An isoplanatic patch is a region from which all signals will have the same phase errors caused by a turbulent propagating medium. The size of the isoplanatic patch depends on wavelength and the scale of the propagating medium disturbances. Proofs are given in [MB74, HON77] for the sharpness functions in [MB74]. After a small modification, Bucker [Buc78] applied one of these sharpness functions to the similar problem of towed-array calibration. Ferguson [Fer90b] modified this sharpness function slightly and applied it to towed arrays,

again with similar results. The sharpness algorithm for towed arrays approximates the array's shape with a sum of a small number of sinusoids. Towed arrays have omnidirectional sensors, and so the assumption that all signals come from an isoplanatic patch was violated in [Buc78] and [Fer90b]. Despite this, the results of these papers showed that sharpness, applied to towed arrays, is viable.

The lack of a proof for the sharpness functions in [Buc78] and [Fer90b] prompted the work of [DC92], where it is shown that they are not consistent with the sharpness concept. Because the sharpness function for towed arrays is complex, a general proof could not be provided. Instead, using a series of simplified functions, it is shown that sharpness will not be a maximum in every circumstance when the errors of the hydrophone position estimates are zero. Thus, the results of [DC92] disagree with those of [Buc78, Fer90b]. Here I will try to resolve this.

The outline of this chapter is as follows. Section 6.2 introduces array-processing concepts that supplement Chapter 2. In Section 6.3 I trace, from the literature, the development of the sharpness concept applied to real-time correction of optical-telescope images [MB74], and point out the similarity of this to a self-calibration technique used on radio telescopes [HON77]. I then look at how one of the sharpness functions discussed in [MB74] was adapted to towed arrays [Buc78, Fer90b], and at its analysis in [DC92]. I assume that the towed array and signals exist within a plane, the signals are narrowband and that the noise is spatially uncorrelated and uncorrelated with the signals. Section 6.4 contains a discussion on the results and discrepancies of [DC92] and [Buc78, Fer90b]. I use computer simulations to help explain the characteristics of the sharpness function of [Buc78, Fer90b]. In section 6.5 I do computer simulations using a number of trial sharpness functions, to determine whether or not alternate sharpness functions might exist for towed arrays. The results of these simulations give some indication of whether the trial functions are convex, and whether they will meet the sharpness concept. I found three trial functions that are convex. Conclusions are given in section 6.6.

I stress that an algebraic analysis of sharpness for towed arrays is very difficult. As shown in [DC92] an algebraic analysis can be applied only to simple two-element arrays. This is why I have used computer simulations to investigate the behaviour of the sharpness functions.

6.2 More Array Concepts

The power output from a beamformer is given in (2.21). When the hydrophone positions are imprecisely known then estimates of the sensor positions must be used in (2.20), in place of their actual values. Writing the dependence of the beamformer output explicitly,

$$P_b(\phi, \{\phi_n\}, \{\chi_m\}, \{\hat{\chi}_m\}) = \mathbf{w}^{\mathrm{H}}(\phi, \{\hat{\chi}_m\}) R(\{\phi_n\}, \{\chi_m\}) \mathbf{w}(\phi, \{\hat{\chi}_m\}), \qquad (6.1)$$

where a hat denotes an estimate. When $\{\hat{\chi}_m\} = \{\chi_m\}$, (6.1) is a discrete Fourier transform relation. Correlation is a function in the separation domain and power is a function in the direction-cosine domain. The Fourier transform relationship of power and correlation can be explained more formally by introducing the **pupil function** and the **transfer function**.

The pupil function, $p(\chi)$, of an array or telescope is a function of position and is the complex amplitude of a signal as detected by a sensor at χ (it includes gains of the sensor, amplifiers etc.). It includes the effect of the propagating medium as well as sensor gains. If all sensors have identical gain and the propagating medium is ideal, as assumed earlier, then the pupil function is unity at the locations of the sensors of an array (or within the aperture of a telescope) and zero elsewhere. The transfer function, $T(\chi)$, is the autocorrelation of the pupil function, and is thus a function of separation. The beamformer output, or image, is the Fourier transform of the correlation function, $r(\chi)$, windowed by the transfer function.

Assuming that an infinite number of sensors, each the size of a point, can be packed into an area so that they form a **continuous sensor**, the correlations of (2.15) can be measured at every separation up to the size of the continuous sensor. The beamformer output from the continuous sensor is the continuous Fourier transform of the correlations. This is exactly what is achieved by an optical or radio telescope. The lens or parabolic reflector of a telescope performs a continuous Fourier transform on the correlations in the aperture to produce the equivalent of the beamformer output (in astronomical terms the output is called the image). Some form of sensor, such as an eye (for optical telescopes), is then able to measure the power of the image at each point δ_n. The pupil and transfer functions are ideally as shown in Figure 40. The pupil and transfer functions of an array of point sensors consists only of impulses.

Figure 40 Pupil and transfer functions of a telescope.

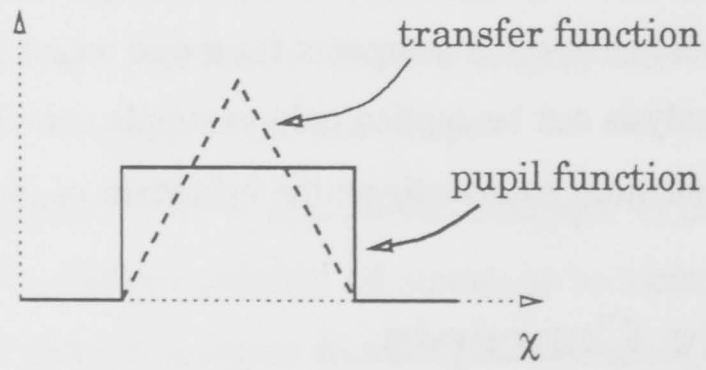

A telescope is typically used to view signal sources that are directly above the aperture plane. Signals that source from outside the main lobe of a telescope's beam pattern are greatly attenuated and their effect on the correlations is assumed negligible. Thus the elevation of all signal sources in view is very close to 90°.

6.3 Development of the Sharpness Concept

This section traces the development of the sharpness concept in the literature, from its use in optical [MB74] and radio telescopes [HON77], to its application to towed arrays [Buc78, Fer90b].

6.3.1 Sharpness applied to optical astronomy

The sharpness concept was developed by Muller and Buffington [MB74], as a means of correcting atmospherically degraded images in real time. We know that for optical telescopes with an aperture greater than 10–30 centimetres, atmospheric turbulence will distort the signals' wavefronts, by changing the phase of light with different paths, so that they will not be planar. This will cause the image to degrade because the telescope relies on receiving plane waves. Muller and Buffington define sharpness in such a way that, under certain conditions, the "value of sharpness for an atmospherically degraded image is always less than that of the true image." Their first trial sharpness function was

$$S_1(P_b) = \int\int P_c^2(\delta_{\phi,\theta})\, d[\delta_{\phi,\theta}]. \tag{6.2}$$

They proposed introducing elements into the light path which could adjust the phase of the light and cancel the atmospheric disturbances in real time. Sharpness, S_1 is maximised with respect to the phases introduced by the adjusting elements. All signals are assumed to exist in an isoplanatic patch of the sky which is centred on a point in the far field, perpendicular to the aperture plane. Their proposed model for atmospherically induced errors is shown in Figure (41). This model supposes that the complex correlations in the aperture plane are distorted by a function which depends solely on the separation of the correlation, and is independent of the signal distribution. The independence of the distortion to the signal distribution is a direct consequence of the isoplanatic signals assumption. That is,

$$r'(\chi) = r(\chi)T(\chi) \tag{6.3}$$

where $'$ indicates a distorted measurement. Therefore, maximising S_1 will depend on the state of the atmosphere and be independent of the signals. Sharpness function, S_1, is defined so that if $T(\chi)$, which includes the effects of correction as well as the atmospheric distortion, is anything other than a simple translation of the image ($p(\chi) = \exp[j(a + b\chi)]$), then sharpness will be less than a maximum.

Figure 41 Muller and Buffington's [1] model for atmospheric phase disturbances. The position of the arrows indicates relative phase. Phase errors are independent of signal direction, assuming that all signals are located in an isoplanatic patch of the sky.

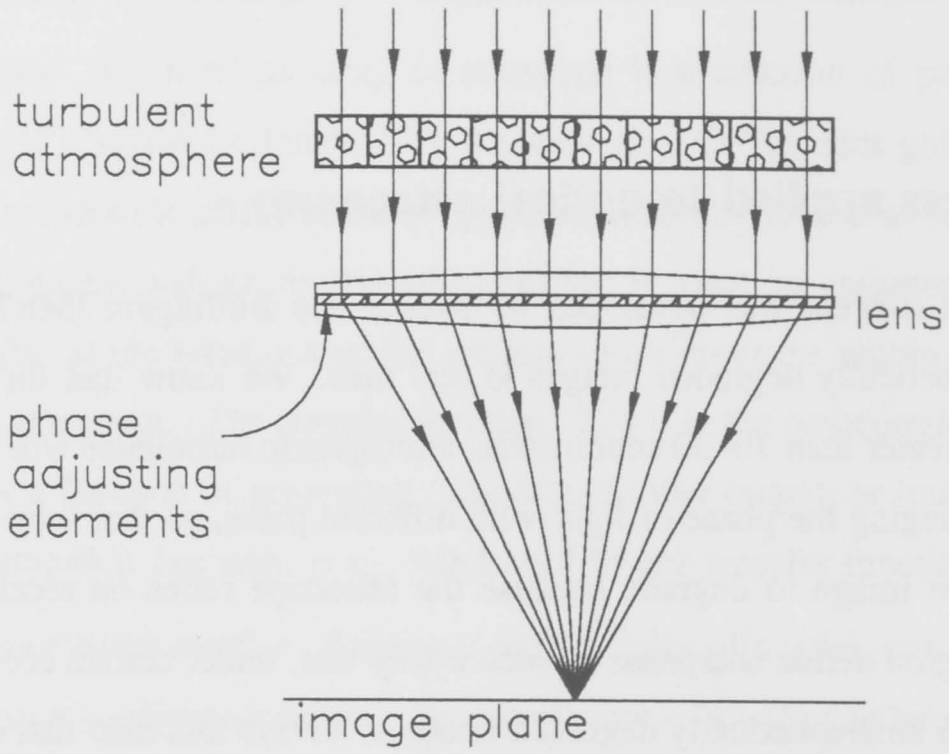

6.3.2 Proof of the sharpness function and comparison with radio astronomical methods of self-calibration

Muller and Buffington's proof that their sharpness functions satisfy the requirements of the sharpness concept is cumbersome. Hamaker et al. [HON77], provide an alternative, more accessible proof for the sharpness function, S_1, that allows them to compare sharpness with a radio astronomy array-calibrating technique known as **redundant self-calibration** (see Section 5.2.5). The image, $P_b(\delta_{\phi,\theta})$, is related to the correlations and transfer function, $T(\chi)$, by the Fourier transform relation and (6.3):

$$\begin{aligned} P_b(\delta_{\phi,\theta}) &\Leftarrow \mathrm{FT} \Rightarrow r'(\chi) \\ P_b(\delta_{\phi,\theta}) &\Leftarrow \mathrm{FT} \Rightarrow r(\chi)T(\chi). \end{aligned} \tag{6.4}$$

According to Parseval's theorem,

$$\begin{aligned} S_1(P_b) &= \int\int P_c^2(\delta_{\phi,\theta})\, d[\delta_{\phi,\theta}] \\ &= \int\int |r(\chi)|^2 |T(\chi)|^2\, d\chi. \end{aligned} \tag{6.5}$$

The correlations, $r(\chi)$ are determined by the source distribution alone, and so maximising S_1 with respect to the phase errors is equivalent to maximising $T(\chi)$ for all χ. The transfer function, $T(\chi)$, is the autocorrelation of the pupil function, $p(\chi)$ and, assuming that the unperturbed pupil function, $p_0(\chi)$, is real and the atmospheric disturbances affect only the phase, then $p(\chi) = p_0(\chi)\, \exp[je(\chi)]$, where $e(\chi)$ is the phase distortion resulting from atmospheric

turbulence at position χ. And so,

$$T(\chi) = \int\int p_0(\omega) p_0^*(\omega + \chi) \exp\left[j(e(\omega) - e(\omega + \chi))\right] d\omega. \tag{6.6}$$

This integral represents a summation of complex vectors, $\{\exp\left[j(e(\omega) - e(\omega + \chi))\right]\}$, which is maximised when the orientations are all the same. Thus,

$$e(\omega) - e(\omega + \chi) = \Psi(\chi) \tag{6.7}$$

is independent of ω and it can be shown that $e(\chi) = a + b\chi$. The constant a is of no consequence and the tilt, b, represents a shift of the image. So, apart from this shift, maximising S_1 leads to a fully restored image.

The self calibrator of Section 5.2.5 relies on the existence of redundant baselines. In a uniform linear array of M elements, for example, there are $M - 1$ baselines of single spacing, $M - 2$ baselines of double spacing, and so on. The correlation measured at baselines of equal length and orientation should be equal, so that any differences in those correlations must be caused by atmospheric disturbances. Indeed, as pointed out in [HON77], the interpretation of (6.7) is that measurements of the same correlation at different locations in the aperture should yield the same answer. The sharpness function, S_1, applies the constraint in (6.7) without the need to measure the correlations, directly.

6.3.3 Sharpness applied to towed arrays

Bucker [Buc78] formulated the sharpness function,

$$S_2(P_b) = \int_0^{\pi} P_c^2(\phi) \sin\phi \, d\phi \tag{6.8}$$

to estimate the shape of towed arrays. The addition of the $\sin\phi$ term in (6.8) compensates for lower resolution, and broader beams, of the beamformer at endfire, so that undue weighting is not given to targets that approach the endfire directions. The estimated array-shape was parameterised in the form of a harmonic series,

$$y_m = f(\{\alpha_\lambda\}, \{\beta_\lambda\}, x_m) = \sum_{\lambda=1}^{\Lambda} \left[\alpha_\lambda \sin\left(\frac{\lambda\pi x_m}{H}\right) + \beta_\lambda \cos\left(\frac{\lambda\pi x_m}{H}\right)\right], \tag{6.9}$$

where $H = L_a + c_v T$, L_a is the length of the array, c_v is the tow vessel's speed, and T is the total integration time of the time average in (2.21).

Figure 42 Flow chart for basic operation in the maximisation of sharpness, S_2. One iteration loop consists of doing the basic flow chart operation for every parameter, $\{\alpha_\lambda\}$ and $\{\beta_\lambda\}$. Sharpness is maximised by repeating the iteration loop a fixed number of times.

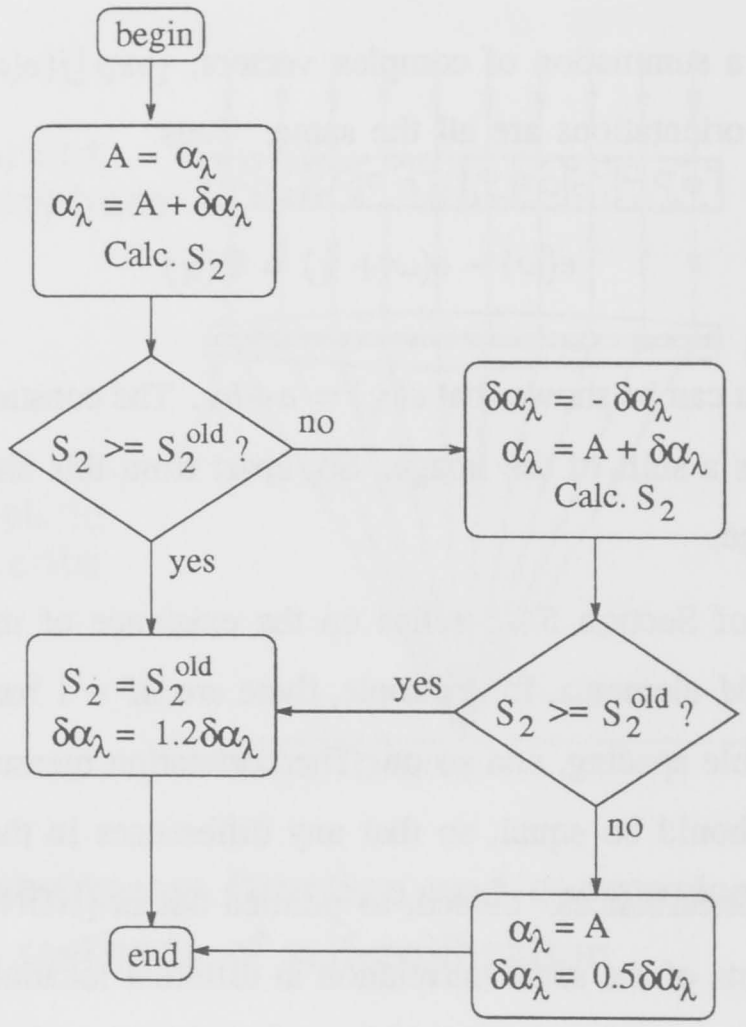

Bucker proposed a method for maximising sharpness where each parameter, α_λ or β_λ, is adjusted in turn. Beginning with an initial array-shape estimate, such as all α_λ and β_λ set to zero, an initial set of step sizes for each parameter, $\delta\alpha_\lambda$ and $\delta\beta_\lambda$, and a value of sharpness for the initial array-shape, the adjustment of each of the parameters and step sizes proceeds according to the flowchart of Figure 42. An iteration consists of repeating the basic operation, as defined in Figure 42, once for each of the parameters, $\{\alpha_\lambda\}$ and $\{\beta_\lambda\}$, in (6.9). The procedure is stopped after a predetermined number of iterations. Bucker claims that although the method is crude, it is reliable. He demonstrated the method with both simulated and real data.

The optimisation procedure of Figure 42 works well and, from my own simulations, I would agree with Bucker when he says it is reliable. For ten iterations and an array modelled by four sinusoids, the procedure requires around 60 calculations of sharpness. Compare this with the procedure of Sections 5.2.8 and 5.3.8 which require around 492 calculations of sharpness for an array modelled by just one sinusoid.

Bucker's work was extended by Ferguson [Fer90b] who used a Capon estimator instead of the conventional beamformer. The sharpness function, S_3, used in [Fer90b], is given by

$$S_3 = \int P_a^2(\phi) \sin\phi \, d\phi, \tag{6.10}$$

where

$$P_a(\phi) = \left[\mathbf{w}^{\mathrm{H}}\mathbf{R}^{-1}\mathbf{w}\right]^{-1} \tag{6.11}$$

is the power output of a Capon estimator, for look direction ϕ. Like the conventional beamformer, the Capon estimator estimates signal power for a given look direction. It has narrower beam widths and lower sidelobe levels, for a given array, than the conventional beamformer. Its resolution is finer because it maintains unity gain in the look direction while reducing interference from signals away from the look direction. The Capon estimator and, hence, S_3, are more sensitive to position estimation errors. Results similar to those in [Buc78] were obtained. Neither [Buc78] nor [Fer90b] presented a proof for their respective sharpness functions.

6.3.4 Mathematical analysis of sharpness

Recognising that there was no formal justification for the sharpness functions, S_2 and S_3, in [Buc78] and [Fer90b], an attempt to study S_2 algebraically was made by Davidson and Cantoni [DC92]. Expressions for the partial derivatives of S_2 with respect to the estimated array parameters, $\{\hat{\alpha}_\lambda\}$ and $\left\{\hat{\beta}_\lambda\right\}$ were derived, and these are shown in appendix C. Because of the complexity of the expressions for $\delta S_2/\delta\hat{\alpha}_\lambda$ and $\delta S_2/\delta\hat{\beta}_\lambda$, Davidson and Cantoni assumed that the sensor position estimates are independent of one another, and that the estimates in orthogonal directions are also independent. Despite this assumption, the partial derivatives for a general M element array are still too complex to analyse, and so simplified models consisting of two-element arrays with unknown separation, were analysed instead. Davidson and Cantoni show that the partial derivatives, $\delta S_2/\delta\hat{\chi}$ and $\delta S_3/\delta\hat{\chi}$, depend on the signal distributions and the white-noise level, and thus will not necessarily be zero when $\hat{\chi} = \chi$. This tells us that S_2 will not necessarily be a maximum when the hydrophone positions are estimated correctly. Sidelobe leakage is identified as the cause of this problem. Because $\delta\hat{\chi}/\delta\hat{\alpha}_\lambda$ and $\delta\hat{\chi}/\delta\hat{\beta}_\lambda$ are independent of both the signal directions and the look direction, S_2 will not necessarily have a maximum if the array shape is parameterised in the form of (6.9), and

$$\begin{aligned} \hat{\alpha}_\lambda &= \alpha_\lambda, \\ \hat{\beta}_\lambda &= \beta_\lambda, \quad \forall\, \lambda, \end{aligned} \tag{6.12}$$

for the same reason. So, on the one hand, the results of [Buc78, Fer90b] suggest that the sharpness method is a reliable means of array calibration while, on the other hand, [DC92] proves that, in general, S_2 does not satisfy the sharpness concept, and therefore that the sharpness method is not worth pursuing as a method of estimating the shape of a towed array.

6.4 Why Sharpness Works

In this section, I present computer simulations of the sharpness function, S_2, that are more comprehensive than those of [Buc78, Fer90b]. The simulations indicate that, despite the proof of [DC92] that S_2 does not meet the sharpness concept, the sharpness method described in [Buc78] will provide sufficiently accurate array-shape estimates for beamforming to maintain its performance under a variety of realistic array shapes and signal-source distributions. Davidson and Cantoni [DC92] explain why S_1 meets the sharpness concept when it is applied to optical astronomy, yet S_2 does not when it is applied to towed arrays;

1. the beamformer of (2.21) bears no relation to optical telescope imaging, and
2. sidelobe power leakage of the beamformer, when there are multiple signals, biases the sensor position estimates.

In fact, as was explained in Section 6.2, optical imaging and beamforming are the same, both being a Fourier transform of the spatial correlations windowed by the transfer function, making point 1 incorrect. The difference between the two systems is that a telescope produces images over portions of the hemisphere that is the sky above the aperture plane, while a towed-array beamformer is generally only used to produce an image over the hemisphere's circumference, which is in the plane of the array. The telescope's look direction is represented by two parameters, azimuth and elevation, while the towed-array beamformer's look direction is represented by a single parameter, azimuth. Considering this, point 2 of the list is also clearly incorrect, because if sidelobe leakage causes a bias in the sensor position estimates of [Buc78, Fer90b], then it would also cause a similar bias in the phase disturbance estimates of [MB74, HON77] and, as it was proven, this is not the case. The real reason that S_2 does not meet the sharpness concept is that all of the signals do not originate from an isoplanatic patch. This isoplanatic signals assumption is equivalent to assuming that the image errors are caused solely by unknown channel- (or position-) related phase errors (see Figure 41). In other words, the phase error, $e(\chi)$, at a particular channel (or at a particular point) is the same for every signal, and so is independent of the signal direction. For towed arrays, if the sensor-position estimation errors are $\{\tilde{\chi}_m\}$, then the error of the correlation estimate, for the n^{th} signal and position χ_m is $\exp(j\pi\tilde{\chi}_m\delta_n)$, which depends on the DOA of the signal. Therefore, the signals do not originate from an isoplanatic patch for towed arrays and each signal will have different phase errors for a given separation.

In spite of this, when the array is parameterised by modelling it as a sum of a small number of sinusoidal shapes, as described in [Buc78], and sharpness is maximised according to the flow chart of Figure 42, good array-shape estimates can be obtained. To demonstrate this I present

Figure 43 Relative values of sharpness versus estimated sensor separation. The system has two sensors with a true separation of one and a single signal at 90°. The value for sharpness is given relative to the sharpness at the correct separation.

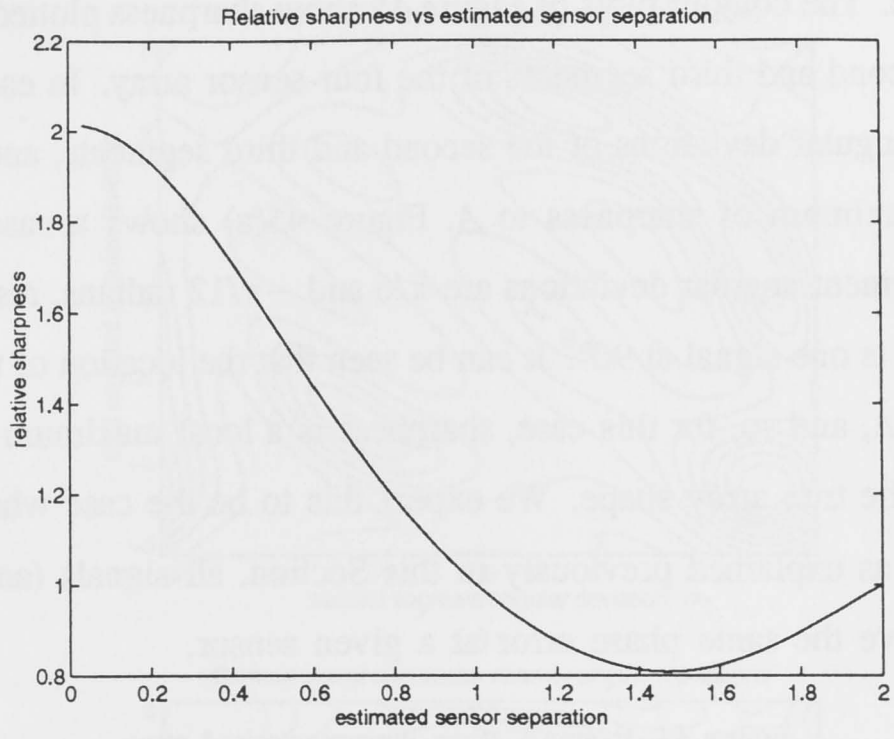

a series of computer simulations that will highlight the difference between sharpness when the estimated array shape is unconstrained and when the estimated array shape is a sum of sinusoids.

In these simulations I use the ideal array-covariance matrix, as given in (2.14). The beamformer power is calculated at 1° intervals from 0° to 180° using (6.1). The integrals in (6.8) and other sharpness functions are calculated by summing the discrete beamformer powers.

It is shown in [DC92] that, for a simplified system involving just two sensors, sharpness will not necessarily be a maximum when the estimated separation between the sensors is equal to the true separation. This is because the resolution of a beamformer is inversely related to the size of the array's aperture which, for the two-element array, is the distance between the sensors. Thus, the smaller the separation of the two sensors, the broader the beam, and S_2 is greater. This can be seen in the plot of sharpness versus estimated separation of Figure 43, in which the maximum value for sharpness occurs when the separation is smallest. It explains a tendency for S_2 to have maxima at points where the estimated array-shape doubles back on itself, producing the smallest aperture. As can be seen in the simulation results of Figure 45, S_2 has a local, and possibly global, maximum at the point where the estimated array shape has the smallest aperture. When the estimated array shape is parameterised, this problem is eliminated, because the sinusoids that model the array do not double back on themselves.

To visualise how the sharpness function behaves with respect to changes in the array shape and signal distribution, I simulate an unconstrained array with four sensors that have an interelement distance equal of one. The form of the unconstrained array shape is shown in Figure 44. It consists of a series of straight-line segments (of constant length ρ) that deviate from one another by angles, $\{\psi_m\}$, which are measured from extensions of the previous segments.

The first segment is fixed to the x-axis, to avoid rotational ambiguities (sharpness can only be maximised to within a shift of the original image which, for beamformers, corresponds to a rotation of the array). The contour plots of Figure 45 show sharpness plotted against the angular deviations of the second and third segments of the four-sensor array. In each case, the point A represents the true angular deviations of the second and third segments, and point B represents the nearest local maximum of sharpness to A. Figure 45(a) shows a case where the array's second and third segment angular deviations are $\pi/6$ and $-\pi/12$ radians, respectively, as shown at point A, and there is one signal at 90°. It can be seen that the location of the maximum, point B, is equal to point A, and so, for this case, sharpness is a local maximum when the estimated array shape equals the true array shape. We expect this to be the case whenever there is only one signal because, as explained previously in this Section, all signals (and in this case there is only one) will have the same phase error at a given sensor.

Figure 44 Example of an unparameterised array.

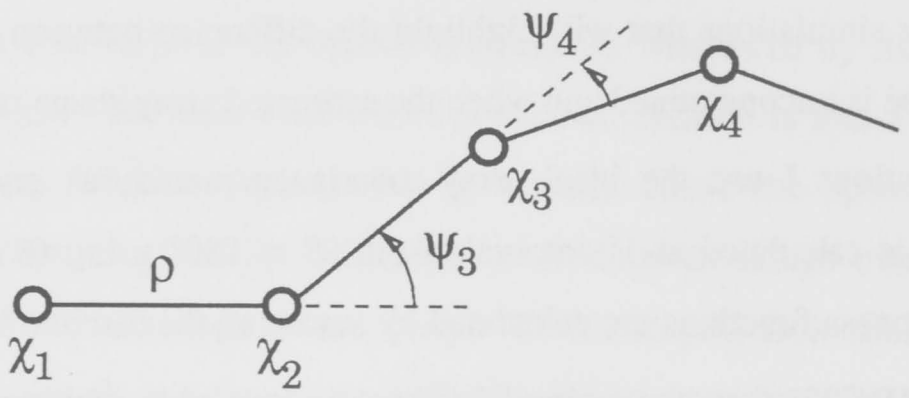

Figure 45(b), represents the case in which there are two signals of equal power, at 90° and 150°, and it can be seen that the true array shape, at point A, and the location of the maximum of sharpness, at point B, do not coincide. If the signals are closer together, such as in the example of Figure 45(c), where the signal directions are 90° and 100°, then the true array shape and the location of the maximum, at points A and B respectively, are nearly coincident. This is because the phase errors of one signal will be approximately equal to the phase errors of another signal, when their directions are approximately equal. In general, S_2 will not have a local maximum at the point equal to the true array shape when there are two or more signals, unless the signals are spaced closely together, because each signal will have a different phase error for a given separation.

The problems of multiple signals with widely different directions of arrival, are overcome by modelling the array as a sum of sinusoids. Figure 46 shows the solutions for array shape that are obtained by maximising sharpness, subject to the array shape's being:

1. unconstrained, where sharpness is maximised over the angular deviations of all segments (Figures 46(a), (c) and (e)); and

Figure 45 Contour plot of sharpness versus the estimated second and third segments' angular deviations. The array has four sensors, with a true array shape defined by the point A. The nearest local maximum to A is point B. The signal DOAs are (a) 90°, (b) 90° and 150°, and (c) 90° and 100°.

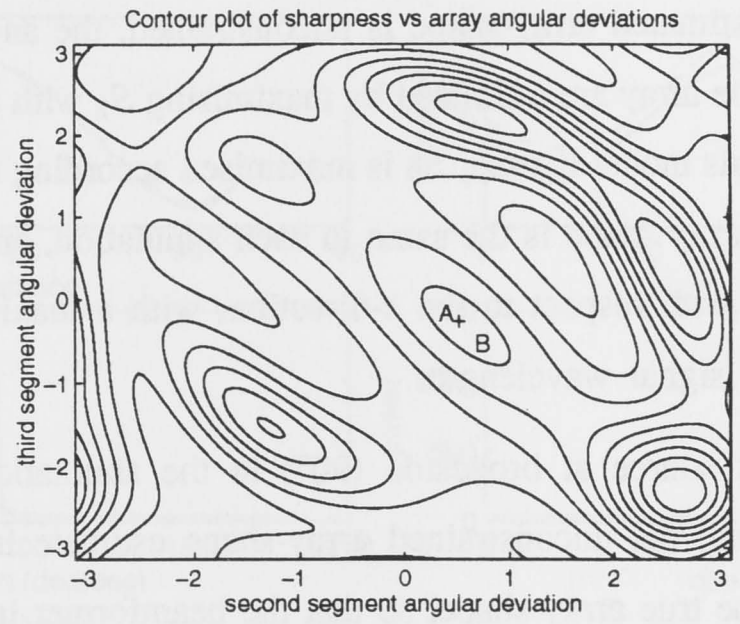

(a)

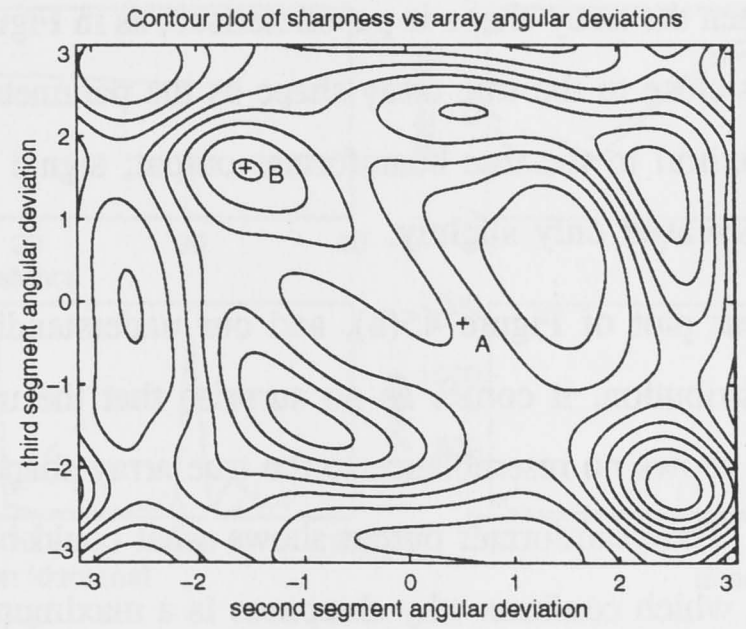

(b)

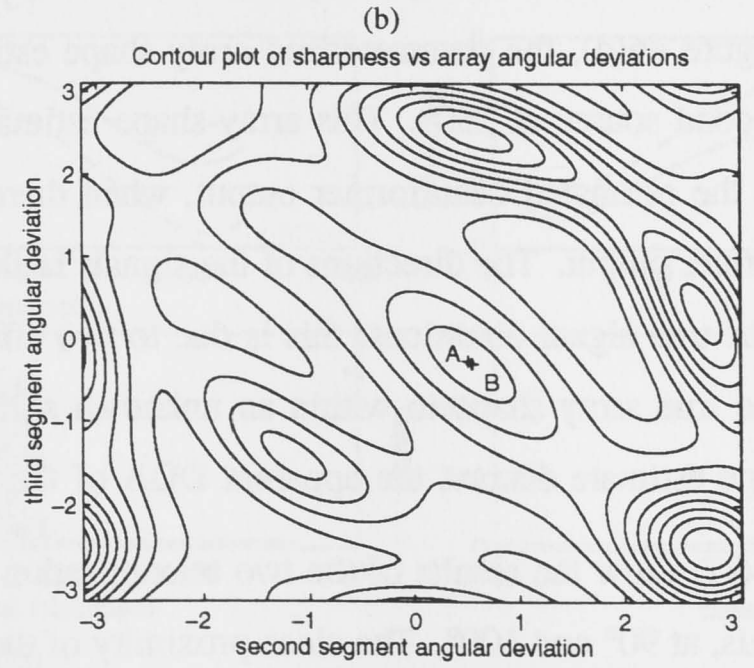

(c)

2. modelled as a sum of three sinusoids, of wavenumber $H/2$, H and $2H$, and one cosinusoid of wavenumber $H/2$ (Figures 46(b), (d) and (f)).

Also shown are the true and estimated beamformer outputs, the estimated one being based on the array-shape estimate. In each case, the true beamformer output or array shape is drawn

with a solid line, and the estimates with dashed lines. The array I simulate has 35 hydrophones that are joined by inflexible segments with a length of one. The signals are narrowband and incoherent. When the estimated array-shape is unconstrained, the angular deviations between successive segments of the array are estimated by maximising S_2 with a simplex search method. When the sum of sinusoids model is used, S_2 is maximised according to the method outlined in Section 6.3.3. The true array shape is the same in each simulation, and is defined by a quartic shape in the y-direction with respect to the x-direction, with a maximum deviation from the x-axis of 0.83 times the signal wavelength.

There is one signal source at broadside (90°) in the simulations of Figure 46(a) and 46(b). It can be seen that the unconstrained array-shape estimate in Figure 46(a) is almost indistinguishable from the true array shape, so that the beamformer image is indistinguishable from the true image. When the array-shape is parameterised, as in Figure 46(b), the array-shape estimate is seen to be as close to the true array shape as the parameterisation will allow. The beamformer output is faithful to the true beamformer output; signal power is underestimated and the sidelobes are increased only slightly.

Based on the contour plot of Figure 45(b), and our understanding of the importance of an isoplanatic signal distribution, it comes as no surprise that the unconstrained array-shape estimate of Figure 46(c) shows no resemblance to the true array shape, due to the inclusion of a second signal at 150°. The beamformer output shows what could be two very broad signals at around 90° and 120°, which confirms why sharpness is a maximum for this, rather than the true, array shape. In Figure 46(d), the parameterised array-shape estimate appears unaffected by the inclusion of a second source at 150°. This array-shape estimate is very similar to that of Figure 46(b), and so the estimated beamformer output, when there are two signals, is also close to the true beamformer output. The directions of the signals in the beamformer output are slightly different from the true signal directions; this is due to two effects: 1) the maximum of sharpness determines the true array shape to within an unknown shift, or rotation, and 2) the parameterised array-shape estimate distorts the apparent DOA of the signals.

Figures 46(e) and 46(f) show the results of the two maximisation methods, when there are two closely spaced signals, at 90° and 100°. The close proximity of the two signals has resulted in a good approximation to the true array shape (Figure 46e) for the unconstrained array, which is because both signals have approximately equal correlation phase errors for a given sensor separation. The beamformer output shows a substantial signal-direction error, because of the invariance of S_2 to rotations of the estimated array-shape. The same rotation is evident in the parameterised array of Figure 46(e), although its *shape* is still close to the true array shape.

Figure 46 Plot of actual (solid lines) and estimated (dashed lines) array shapes and beamformer images using sharpness function S_2. The array is not parameterised in (a), (c) and (e). The array is modelled as the sum of three sinusoids with wavenumbers of $H/2$, H and $2H$ in (b), (d) and (f).

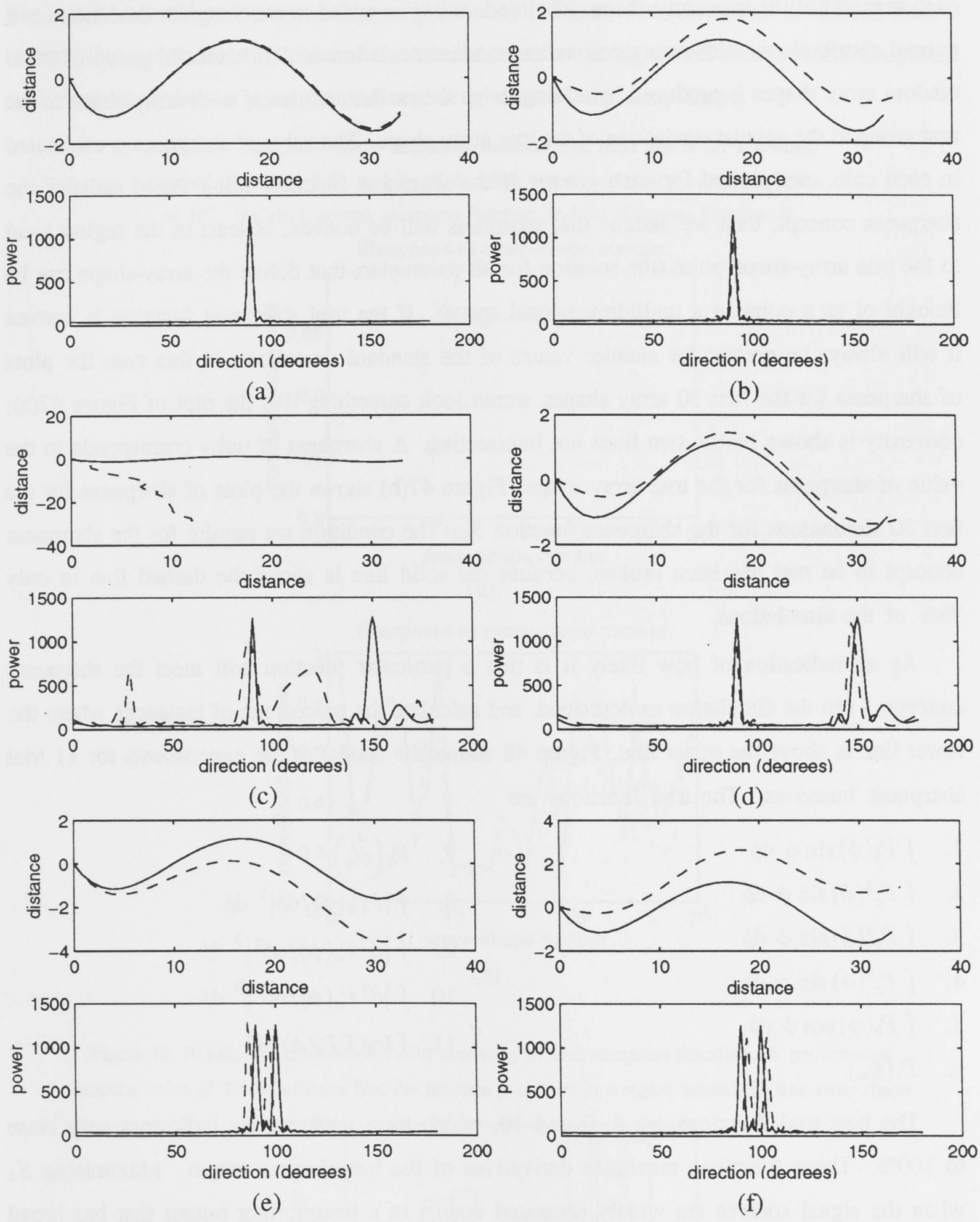

6.5 New Sharpness Functions for Towed-Arrays

In this Section, I test for the possible existence of a sharpness function that will satisfy the sharpness concept, for omnidirectional arrays. The sharpness functions that I investigate are taken from [MB74]. I test the functions by simulating a 35-element array with two signals,

at 90° and 150°. The array has the same shape as the simulations of Figure 46. A group of 2500 random array shapes are produced by adding a random angle to the angular deviation of each segment of the true array-shape. The random angles added to each angular deviation have normal distributions, with zero mean and a standard deviation of 5°. A second group of 2500 random array shapes is produced by adding twice the random angles of each array-shape in the first group to the angular deviations of the true array-shape. The value of sharpness is calculated in each case, and plotted for each group. If the sharpness function being tested satisfies the sharpness concept, then we assume that sharpness will be convex, at least in the region local to the true array-shape point (the solution for all parameters that define the array-shape can be thought of as a point in a multidimensional space). If the trial sharpness function is convex it will always be greater for smaller values of the standard deviation. In this case the plots of sharpness for the first 30 array shapes would look something like the plot of Figure 47(a); convexity is shown by the two lines not intersecting. A sharpness of unity corresponds to the value of sharpness for the true array shape. Figure 47(b) shows the plots of sharpness for the first 30 simulations for the sharpness function S_2. The condition we require for the sharpness concept to be met has been broken, because the solid line is above the dashed line in only 78% of the simulations.

As an indication of how likely it is that a particular function will meet the sharpness concept, I run the simulation as described, and calculate the percentage of instances where the lower line is above the upper line. Figure 48 shows the results of the experiments for 11 trial sharpness functions. The trial functions are

1. $\int P_b(\phi) \sin\phi \; d\phi$
2. $\int P_c^2(\phi) \sin\phi \; d\phi$
3. $\int P_c^3(\phi) \sin\phi \; d\phi$
4. $\int P_c^4(\phi) \sin\phi \; d\phi$
5. $\int P_b(\phi) \cos\phi \; d\phi$
6. $P_b(\phi_n)$
7. $P_b\left(\hat{\phi}_n\right)$
8. $\int \left|dP_b(\phi)/d\phi\right|^2 \; d\phi$
9. $\int \left|d^2P_c(\phi)/d\phi^2\right|^2 \; d\phi$
10. $\int \left|d^3P_c(\phi)/d\phi^3\right|^2 \; d\phi$
11. $\int \log\Gamma P_b(\phi) \; d\phi$

The best trial functions are 8, 9 and 10, which have performance indicators very close to 100%. These functions maximise derivatives of the beamformer output. Maximising S_2 when the signal sources are widely separated results in a beamformer output that has broad peaks. However, only beamformer output that has sharp, narrow peaks will maximise functions 8–10. Figure 49 shows array-shape estimates and beamformer outputs for function 9, using the same true array-shape and signal-source distribution as in Figure 46. Whether the signal sources are widely separated or not, trial function 9 gives accurate array-shape estimates for both parameterised and unparameterised arrays. This function is a good choice of sharpness function

for omnidirectional arrays. However, it is likely that the true array shape is not represented by the global maximum of trial function 9, only by a local maximum. Local maxima are not likely to be a problem for towed arrays. If the array is assumed to have small deviations from a straight line and the starting point of the maximisation is a straight line, then the local maximum will most likely be the point that defines, or is close to, the array shape.

Figure 47 Sharpness versus simulation number. The solid line is for a nominal standard deviation of 5°, and the dashed line is for a nominal standard deviation of 10°. (a) ideal, convex sharpness function, and (b) sharpness function S_2.

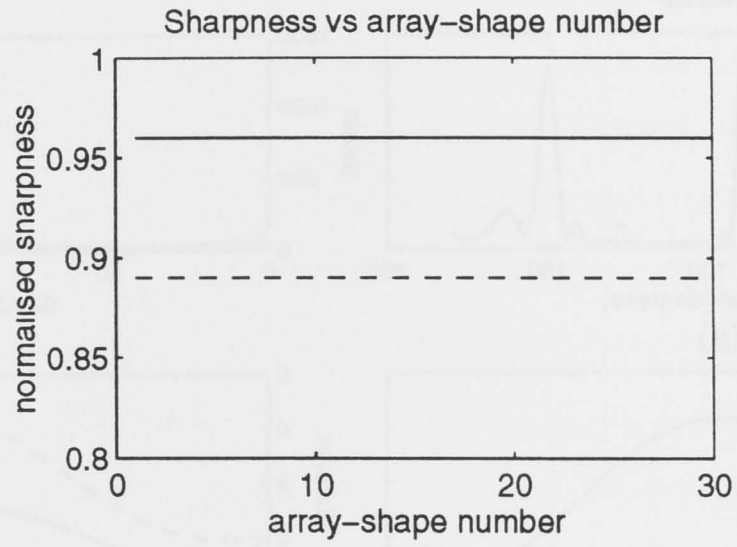

(a)

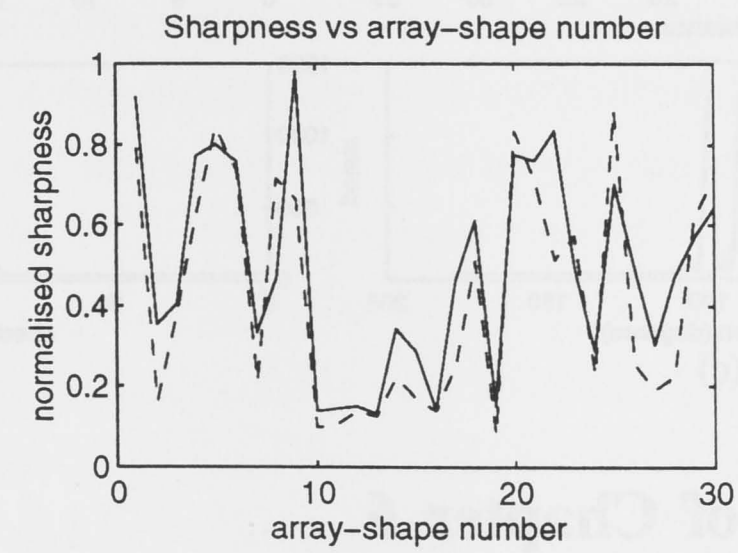

(b)

Figure 48 Results of simulation tests for convexity of trial sharpness functions. A performance indicator value of 100% indicates that the function is convex in a region around the true array shape.

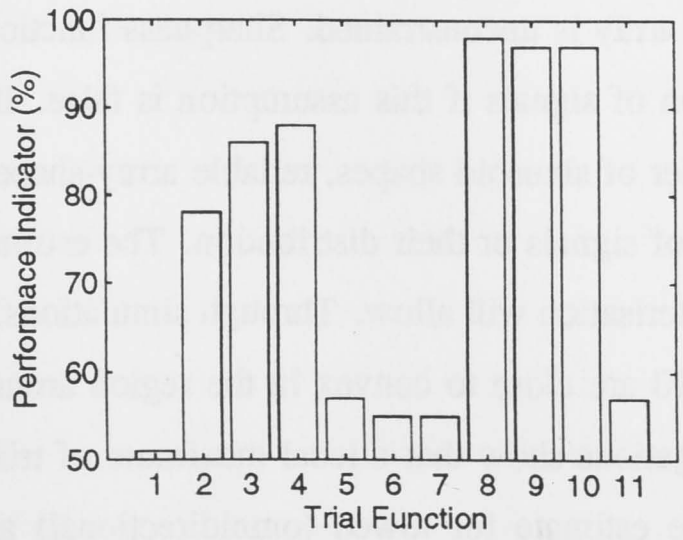

Figure 49 Plot of actual and estimated array shapes and beamformer images (estimates are shown with dashed lines) using trial function 9. The array is unconstrained in (a) and (c). The array is modelled as the sum of three sinusoids with wavenumbers of $H/2$, H and $2H$ in (b) and (d).

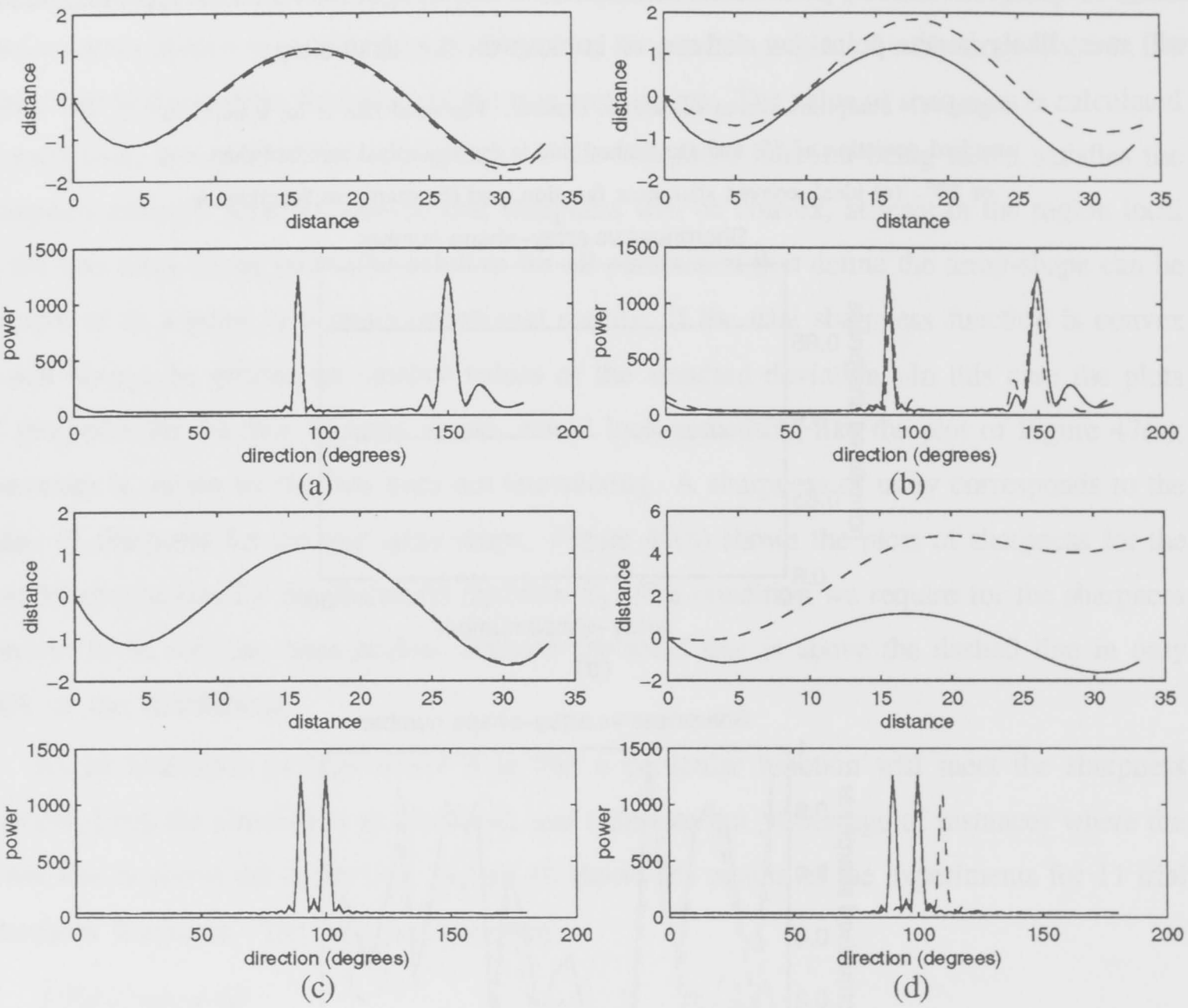

6.6 Summary of Chapter 6

The sharpness method presented in [MB74] was proven to restore atmospherically degraded telescope images to their undistorted state. For omnidirectional arrays such as towed arrays, S_2 [Buc78, Fer90b] is based on the assumption that the signals arrive from only one narrow range of directions, if the array is unconstrained. Sharpness function S_2 has been shown to be sensitive to the distribution of signals if this assumption is false. If the array is parameterised as a sum of a small number of sinusoid shapes, reliable array-shape estimates can be obtained, regardless of the number of signals or their distribution. The estimates are as close to the true array-shape as the parameterisation will allow. Through simulations, I found that trial sharpness functions 8–10 of page 110 are close to convex in the region around the true array shape, for towed arrays. My investigations show that a local maximum of trial sharpness function 9 will provide an accurate shape estimate for towed (omnidirectional) arrays independently of the

number or distribution of signal sources and of whether the array is parameterised or not. In all cases sharpness function requires no *a priori* knowledge of the signals. I conclude that the sharpness algorithm is useful for estimating the shape of towed arrays.

Chapter 7 Conclusion

It is essential for towed array processors to calibrate the array if best performance is needed at all times. The trend is to make towed arrays longer and use more complex array processors so that array calibration will become a necessity. Array calibrators fall into two main categories: signal-based and heading-sensor-based. I have concentrated largely on self (signal-based) calibrators. Self calibrators typically use phase or time-delay information from the impinging signals. The array shape is estimated by applying geometric constraints in a procedure known as the chord approach.

I dealt with the theoretical problem of correlation function invertibility in Chapter 3. This problem has no simple and complete answer. I gave the necessary conditions for the sensor, signal and noise parameters to be observable, in 2D and 3D arrays. Based on a geometric analysis, I found closed form solutions for the sensor and signal parameters given the signal steering vectors. These results are applicable to a generic array. With the additional geometric constraints of towed arrays the parameters are observable, apart from a twin ambiguity, with just one signal. The twin ambiguity is resolved by making the assumption that the array is close to a straight line.

For a generic array, noise parameters are observable if the noise is spatially uncorrelated and uncorrelated with the signals. Given this, the sensor and signal parameters are observable if the signals are incoherent, there are more sensors than signals and there are at least three signals for a 2D array or six signals for a 3D array. The parameters will be unobservable when:

1. noise is spatially correlated, or
2. the signals are coherent and there are less signal sources than given in Section 3.2.4.

When the signals are coherent and the number of signal sources satisfies the requirements in Section 3.2.4 it is not known whether the parameters are observable.

Chapter 4 gave three new towed-array calibrators. The first two calibrators are based on a simple least-squares error optimisation; one uses phase-delay information from narrowband signals and the other uses time-delay information from broadband signals. The first algorithm requires that there be no interfering signals. The second algorithm is insensitive to interfering and coherent signals because of the properties of time-delay estimation. I demonstrated the algorithms' accuracy using computer simulations. However, the exact signal-to-noise ratio of

real underwater acoustic signals is an unknown factor, and is likely to determine whether the algorithms work in a real situation. The third algorithm gives an easy way to fuse measurements from different sources. It uses a state-space model of the towed array. The state-space model is derived from the Paidoussis equation which describes the dynamics of towed flexible cylinders. It provides a convenient framework for array-calibration using the Kalman filter. The Kalman filter has the useful property that it uses the entire measurement history, rather than only the most recent measurements. The mean-square error of the Kalman filter is lower than an equivalent calibrator that uses only the latest measurements.

In Chapter 5 I compared, in theory and using computer simulation, a representative set of towed-array calibrators from the literature. The sensitivities of the calibrators to their underlying assumptions were investigated. I looked at robustness of the calibrators to the following factors: signal-to-noise ratio, presence of interfering signals, presence of coherent signals, and direction-of-arrival of the calibrating signal. I found that the broadband calibrators perform best when there are coherent signals. When there are no coherent signals, the eigenvector [GWR89] and sharpness [Buc78, Fer90b] calibrators are most robust in the presence of interfering signals and low SNR.

The sharpness calibrator is interesting because it tries to make the beamformer image "correct" by maximising a sharpness function. It was originally applied to real-time, optical-telescope image correction. There have been conflicting reports on the sharpness calibrator when applied to towed arrays. I resolved these discrepancies in Chapter 6. I showed that the sharpness calibrator relies on the assumption that all signals arrive from approximately the same direction. However, if the array-shape is parameterised, then the sharpness-calibrator is insensitive to an incorrect assumption of this type. Using the criterion that a sharpness function must be convex, at least in a region local to the maximum, I found a sharpness function that is a better choice than the sharpness function given in [Buc78, Fer90b].

7.1 Further Research

The work in this thesis suggests a number of possible avenues of further research.

7.1.1 Data modelling

In this thesis I have assumed, in keeping with the literature, that the array-covariance matrix is estimated using signals with infinitesimal bandwidth. This model of the data is an ideal one. As was explained in Section 2.14, the correlation estimates will be attenuated if the signals have finite bandwidth. The effect of finite signal bandwidth on self calibrators and array processing algorithms could be investigated.

7.1.2 Three-dimensional array calibration

This thesis is largely restricted to 2D arrays. It would be interesting to investigate the feasibility of estimating the array shape in 3D. I expect that this would involve independent shape estimates in the horizontal and vertical planes. Vertical position information could possibly be provided by noise generated on the ocean's surface, such as by waves breaking.

7.1.3 Issues on array-calibration accuracy

To measure the performance of an array calibrator objectively I have used the RMS position error of the hydrophone estimates. To measure performance subjectively we look at the beamformer output and decide whether the signal directions-of-arrival can be identified and whether sidelobes are within reasonable limits. As shown by the widespread use of the first method, it is generally accepted that the two methods agree with each other. However, as was shown in Chapter 5, there is no simple correlation between the two performance indicators. The results for the sharpness simulations show that even for RMS position errors of the order of a wavelength the beamformer output can still be good subjectively. Although the RMS position error is high, the sine-wave shape estimated by the sharpness calibrator is a good approximation to the array's true polynomial shape. This suggests that the RMS position error criterion may not lead to optimal array calibration when the results are viewed subjectively. Constraining array-shape estimates to be within a subset (e.g. sine-waves) of all possible array shapes may result in better subjective performance of the calibrator. It would be interesting to discover what the optimal subset of array shapes might be.

One possibility comes from the fact that tow-point induced motion of an array implies there is a smooth transition from one shape to the next. Assume that the tow-vessel is travelling in a straight line and the array lies on the same line. Then a series of array shapes, as the tow vessel turns, might look something like those shown in Figure 50. This indicates that a calibrator could operate like a state machine where each state is one particular array shape. The first state, for instance, could be a straight line. The calibrator could either remain in that state, or go to a state like that of Figure 50(b) for a left-hand turn or go to a state which is a reflection of Figure 50(b) for a right-hand turn. To decide whether to remain in the current state or proceed to the next a self calibrator could be used.

7.1.4 Processing by subarrays

An interesting alternative to array-calibration is to process by subarrays. Fuchs [Fuc93] gave a procedure for testing the straightness of an array. He proposed that during a tow-vessel turn the array's shape will have two linear sections with a bend between them. Although the

Figure 50 Example of how a towed array's shape may vary during a tow-vessel maneuver.

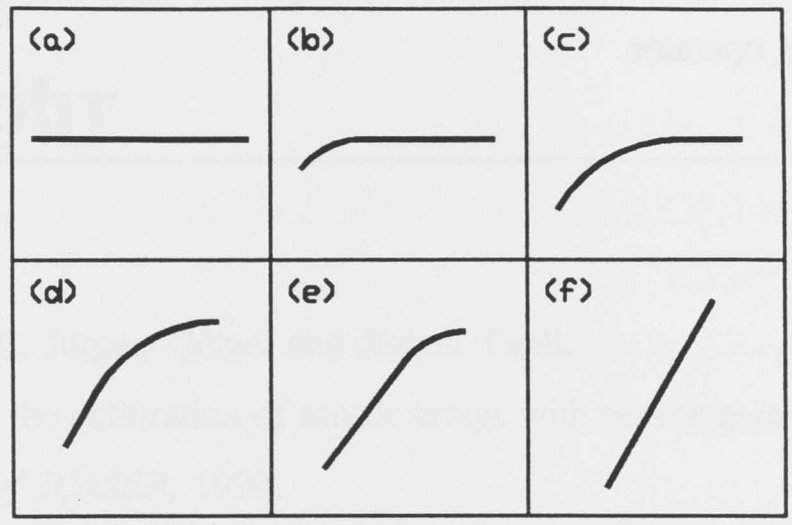

entire array can not be processed on the assumption of linearity, the two straight subarrays can be processed separately. The straightness-testing procedure is used to discover maximum-length straight subarrays. The two subarray can be processed as one and have comparable direction-finding resolution to the full array [SW94]. In this case, the orientation of the straight line subarrays relative to each other would have to be estimated.

7.1.5 Development of real-time calibrators

There are now plenty of towed-array self calibrators in the literature. Attention needs to be given to the development of real-time self calibrators. As a first step, real data from a towed array should be used to compare algorithms from the literature. Chapter 5 has identified the sensitivities of a number of algorithms, and so, from trials with real data it should be possible to decide if the sensitivities are critical. From the algorithms that perform well, the following work needs to be done to develop a working array calibrator:

1. Before starting to develop signal-based array-calibrators the cost of development should be estimated. I have not considered costs in this thesis. But a decision needs to be made as to whether self calibrators will be cheaper than heading-sensor-based calibrators. If they are significantly cheaper, or their performance is significantly better for the same cost, development can proceed.
2. For narrowband self calibrators, discover a way of choosing a frequency band that has a high SNR. Also, for algorithms that require only one signal to be present in the band, a method of ensuring that that condition is met is needed. Such a method can be based upon the fact that if there is only one signal, and assuming the noise power at every hydrophone is equal, then the power of each hydrophone's signal will be equal
3. A method of on-line performance evaluation may be an essential feature of towed-array calibrators. To gain operator acceptance it may be necessary for the system to estimate a performance figure such as hydrophone RMS position error. If the changing performance

figure agrees with the operator's opinion of the performance the system is more likely to be accepted by the operator.

Bibliography

[AGP93] Markus Ali, Jürgen Götze, and Rainer Pauli.

An algorithm for the calibration of sensor arrays with sensor gain and phase uncertainties.

In *Proceedings of ICASSP*, 1993.

[AM79] Brian D. O. Anderson and John B. Moore.

Optimal Filtering.

Prentice-Hall, 1979.

[AS84] E. Ashok and P. M. Schultheiss.

The effect of an auxiliary source on the performance of a randomly perturbed array.

Proc. IEEE ICASSP, 3:40.1.1–40.1.4, 1984.

[BA84] R. R. Bitmead and B. D. O. Anderson.

Kalman filtering approaches for position estimation of towed arrays operating in damped water pulley mode.

Technical report, Dept. Sys. Eng., Australian Nat. Uni., apr 1984.

[Bel84] Maurice Bellanger.

Digital Processing of Signals.

John Wiley and Sons, 1984.

[BH83] Robert Grover Brown and Patric Y. C. Hwang.

Introduction to Random Signals and Applied Kalman Filtering.

John Wiley and Sons, Inc., 1983.

[BMH91] G. C. Brown, J. H. McClellan, and E. J. Holder.

Eigenstructure approach for array processing and calibration with general phase and gain perturbations.

In *Proceedings of ICASSP*, pages 3037–3040, 1991.

[Bou87] M. Bouvet.

Beamforming of a distorted line array in the prescence of uncertainties on the sensor positions.

J. Acoust. Soc. Am., 81:1833–1840, June 1987.

[Buc78] Homer P. Bucker.

Beamforming a towed line array of unknown shape.

J. Acoust. Soc. Am., 63(5):1451–1454, May 1978.

[Car79] G. C. Carter.

Passive ranging errors due to receiving hydrophone position uncertainty.

U.S. Navy J. Underwater Acoust., 29:79–89, 1979.

[Car93] G. Clifford Carter, editor.

Coherence and Time Delay Estimation, chapter Tutorial Overview of Coherence and Time-Delay Estimation.

IEEE Press, 1993.

[Coa90] Rodney F. W. Coates.

Underwater Acoustic Systems.

Macmillan Education Ltd, 1990.

[DC92] T. N. Davidson and A. Cantoni.

Towed array shape estimation using the sharpness concept.

Technical report, Adaptive Signal Processing Laboratory, Dept. Electrical and Electronic Engineering, University of Western Australia, Nedlands 6009, February 1992.

Prepared under a research contract with DSTO Australia.

[DM80] C. Nelson Dorny and Bernard S. Meagher.

Cohering of an experimental nonrigid array by self-survey.

IEEE Trans. Antennas Propagat., AP-28(6):902–904, November 1980.

[Dor78] C. Nelson Dorny.

A self-survey technique for self-cohering antenna systems.

IEEE Trans. Antennas Propagat., AP-26(6):877–881, November 1978.

[Dow88a] A. P. Dowling.

The dynamics of towed flexible cylinders — part 1. neutrally buoyant elements.

J. Fluid Mech., 187:507–532, 1988.

[Dow88b] A. P. Dowling.

The dynamics of towed flexible cylinders — part 2. negatively buoyant elements.

J. Fluid Mech., 187:533–571, 1988.

[Fer89] Brian G. Ferguson.

Improved time-delay estimates of underwater acoustic signals using beamforming and prefiltering techniques.

IEEE J. Oceanic Eng., OE-14(3):238–244, July 1989.

[Fer90a] Brian G. Ferguson.

Enhanced spatial processing of acoustic data from a towed flexible line array when the

spatial distribution of the sensors is unknown.
In *Proceedings of ISSPA*, pages 335–339, 1990.

[Fer90b] Brian G. Ferguson.
Sharpness applied to the adaptive beamforming of acoustic data from a towed array of unknown shape.
J. Acoust. Soc. Am., 88(6):2695–2701, December 1990.

[FGR92] B. G. Ferguson, D. A. Gray, and J. L. Riley.
Comparison of sharpness and eigenvector methods for towed array shape estimation.
J. Acoust. Soc. Am, 91:1565–1570, March 1992.

[Fuc93] Jean-Jacques Fuchs.
Shape calibration for a nominally linear equispaced array.
In *Proceedings of ICASSP*, volume 4, pages 300–303, 1993.

[FW88] Benjamin Friedlander and Anthony J. Weiss.
Eigenstructure methods for direction finding with sensor gain and phase uncertainties.
In *Proceedings of ICASSP*, pages 2681–2684, 1988.

[GAB88] D. A. Gray, B. D. O. Anderson, and R. R. Bitmead.
Models for the application of Kalman filtering to the estimation of the shape of a towed array.
In *Proceeding of the NATO Advanced Study Institute on Underwater Acoustic Data Processing*, 1988.

[GAB93] D. A. Gray, B. D. O. Anderson, and R. R. Bitmead.
Towed array shape estimation using Kalman filters — theoretical models.
IEEE J. Oceanic Eng., 18(4):543–556, oct 1993.

[GG95] Doug A. Gray and Malcolm J. Goris.
A kalman filter based data fusion approach for estimating the shape of a towed sonar array.
In *Proceedings of International Conference on Neural Networks and Signal Processing*, 1995.

[GGM95] Malcolm J. Goris, Douglas A. Gray, and Iven M. Y. Mareels.
Reducing the computational load of a kalman filter when there are more measurements than states.
submitted to Int. J. of Control, 1995.

[GM95a] Malcolm J. Goris and Donald J. McLean.
Calibrating a towed array using redundant information from an impinging broadband

signal.

In *Proceedings of ICSPAT*, 1995.

[GM95b] Malcolm J. Goris and Donald J. McLean.

Towed array-shape estimation — a comparison of methods.

Technical report, CSIRO Division of Radiophysics, EPPING NSW 2121, AUSTRALIA, 1995.

[Gor95a] Malcolm J. Goris.

Array shape estimation using signal information.

submitted to IEEE Trans. Information Theory, 1995.

[Gor95b] Malcolm J. Goris.

Sharpness as a method of towed array-shape estimation.

submitted to IEEE Trans. Signal Processing, 1995.

[Gor95c] Malcolm J. Goris.

Towed array shape estimation — least-squares error method.

submitted to IEEE J. Oceanic Eng., 1995.

[GR90] D. A. Gray and J. L. Riley.

Estimating the shape of a towed array.

Technical report, Defence Science and Technology Organisation, Salisbury, South Australia, 1990.

[Gra86] D. A. Gray.

Models for the application of Kalman filters to the estimation of the shape of a towed array.

Technical report, Australian Dept. of Defence, May 1986.

[GWR89] D. A. Gray, W. O. Wolfe, and J. L. Riley.

An eigenvector method for estimating the positions of the elements of an array of receivers.

In *Proceedings of ASSPA*, pages 391–393, 1989.

[Has84] J. C. Hassab.

The effect of uncertainty in the heading or placement of a sub-array on passive ranging accuracy.

J. Acoust. Soc. Am., 75(2):479–485, 1984.

[Hay85] S. Haykin, editor.

Array Signal Processing.

Prentice-Hall, 1985.

[Hin77] M. J. Hinich.

Bearing estimation using a perturbed linear array.

J. Acoust. Soc. Am., 61:1540–1549, 1977.

[Hin79] M. J. Hinich.

Passive range estimation using subarray parallax.

J. Acoust. Soc. Am., 65:1229–1230, 1979.

[Hod83] W. S. Hodgkiss.

The effects of array shape perturbation on beamforming and passive ranging.

IEEE J. Oceanic Eng., OE-8:120–130, July 1983.

[HON77] J. P. Hamaker, J. D. O'Sullivan, and J. E. Noordam.

Image sharpness, Fourier optics, and redundant-spacing interferometry.

J. Opt. Soc. Am., 67(8):1122–1123, August 1977.

[HRG90] D. A. Holdsworth, J. L. Riley, and D. A. Gray.

The applicatoin of Kalman filtering techniques to the estimation of the shape of a towed array.

Technical report, Weapons System Research Laboratory, DSTO, AUSTRALIA, 1990.

[JD82] D. H. Johnson and S. DeGraaf.

Improving the resolution in bearing in passive sonar arrays by eigenvalue analysis.

IEEE Trans. Acoustics Speech Signal Process., ASSP-30:638–647, 1982.

[Ken81] R. M. Kennedy.

Crosstrack dynamics of a long cable towed in the ocean.

Oceans,, pages 966–970, 1981.

[KS81] R. M. Kennedy and E. S. Strahan.

A linear theory of transverse cable dynamics at low frequencies.

Technical report, Naval Underwater Systems Center, 1981.

[KW93] S. M. Kay and H. C. Woodsum.

Trends and Perspectives in Signal Processing, chapter Sonar Technology, pages 1–7. sep 1993.

[LM87] James Ting-Ho Lo and Stanley Lawrence Marple.

Eigenstructure methods for array sensor localization.

In *Proceedings of ICASSP*, pages 2260–2263, 1987.

[Lo88] James Ting-Ho Lo.

New maximum likelihood approach to multiple signal estimation.

In *Proceedings ICASSP*, pages 2889–2892, 1988.

[Lo90] James Ting-Ho Lo.

Array sensor localization and calibration by cyclic regression.

In *Proceedings ICASSP*, pages 2939–2942, 1990.

[Lo92] James Ting-Ho Lo.

Observability conditions for multiple signal direction finding and array sensor localization.

IEEE Trans. Signal Process., SP-40(11):2641–2650, nov 1992.

[MB74] R. A. Muller and A. Buffington.

Real-time correction of atmospherically degraded telescope images through image sharpening.

J. Opt. Soc. Am., 64(9):1200–1210, September 1974.

[MM80] R. A. Monzingo and T. W. Miller.

Introduction to Adaptive Arrays.

Wiley, New York, 1980.

[MM88] Sylvie Marcos and Odile Macchi.

Adaptive estimation of a time-varying array shape using the tracking properties of the lms algorithm.

In *Proceedings of ICASSP*, pages 1538–1541, 1988.

[MM92] R. G. Marson and D. J. McLean.

Self calibration of towed arrays.

In *Proceedings of ISSPA*, pages 416–420, 1992.

[Nie91] Richard O. Nielsen.

Sonar Signal Processing.

Artech House, 1991.

[OI69] C. R. Ortloff and J. Ives.

On the dynamic motion of a thin flexible cylinder in a viscous stream.

J. Fluid Mechanics, 38:713–720, 1969.

[Ows81] N. L. Owsley.

Shape estimation for a flexible underwater cable.

In *Proceedings of EASCON*, pages 20–23, 1981.

[Ows84a] N. L. Owsley.

Joint source and sensor location estimation.

In *Proceedings of ICASSP*, pages 40.2/1–4, 1984.

[Ows84b] N. L. Owsley.

Sonar Array Processing, chapter 3.

Prentice-Hall Inc., Englewood Cliffs, NJ, 1984.

[Pai66a] M. P. Paidoussis.

Dynamics of flexible slender cylinder in axial flow; part 1 theory.

J. Fluid Mech., 26:717–736, 1966.

[Pai66b] M. P. Paidoussis.

Dynamics of flexible slender cylinder in axial flow; part 2 experiment.

J. Fluid Mech., 26:737–751, 1966.

[Pai73a] M. P. Paidoussis.

Dynamics of cylindrical structures subjected to axial flow.

J. Sound Vib., 29:365–385, 1973.

[Pai73b] M. P. Paidoussis.

Stability of towed, totally submerged flexible cylinders.

J. Fluid Mech., 34:273–297, 1973.

[PFTV87] W. H. Press, B. P. Flannery, S. A. Teulolsky, and W. T. Vetterling.

Numerical Recipes — The Art of Scientific Computing.

Press Syndicate of the University of Cambridge, 1987.

[Pil89] S. Unnikrishna Pillai.

Array Signal Processing.

Springer-Verlag, 1989.

[RG] J. L. Riley and D. A. Gray.

Towed array shape estimation using Kalman filters — experimental investigations.

Technical report, Defence Science and Technology Organisation, Salisbury, South Australia.

[RGF93] J. L. Riley, D. A. Gray, and B. G. Ferguson.

Estimating the shape of a towed array of hydrophones using both acoustic and non-acoustic sensor techniques.

In *Proc. NATO Advanced Study Institute on Acoustic Signal Processing for Ocean Exploration*, 1993.

[RGH90] J. L. Riley, D. A. Gray, and D. A. Holdsworth.

Estimating the positions of an array of receivers using Kalman filtering techniques.

In *Proceedings of ISSPA 90*, pages 364–367, 1990.

[Ric88] C. Richardson.

Towed array-shape prediction.

Technical report, Admiralty Research Establishment, Portland, Dorset DT5 2JS, UK, 1988.

[RS86] Yosef Rockah and Peter M. Schultheiss.

Source localization with two dimensional array subject to uncertainty in sensor location. In *Proceedings of ICASSP*, pages 1885–1888, 1986.

[RS87a] Yosef Rockah and Peter M. Schultheiss.

Array shape calibration using sources in unknown locations — part 1: Far-field sources. *IEEE Trans Acoustics Speech Signal Process.*, ASSP-35(3):286–299, March 1987.

[RS87b] Yosef Rockah and Peter M. Schultheiss.

Array shape calibration using sources in unknown locations — part 2: Near-field sources and estimator implementation.

IEEE Trans Acoustics Speech Signal Process., ASSP-35(6):724–735, June 1987.

[Sch79] R.O. Schmidt.

Multiple emitter location and signal parameter estimation.

In *Proceedings of RADC Spectral Est. Workshop*, pages 243–258, October 1979.

[Sch81] R. O. Schmidt.

A Signal Subspace Approach To Multiple Source Location And Spectral Estimation.

PhD thesis, Stanford University, Stanford, CA, May 1981.

[SI80] P. M. Schultheiss and J. P. Ianniello.

Optimum range and bearing estimation with randomly perturbed arrays.

J. Acoust. Soc. Am., 68:167–173, July 1980.

[SW94] Jacob Sheinvald and Mati Wax.

Detection and localization of multiple signals using subarrays data.

Technical report, RAFAEL 83, POB 2250, Haifa, ISRAEL 31021, feb 1994.

[Tho89] A. Richard Thompson.

Synthesis Imaging in Radio Astronomy, chapter The Interferometer in Practice.

Astronomical Society of the Pacific, 1989.

[TN88] Tore Tollefsen and Arye Nehorai.

Adaptive calibration of randomly perturbed sensor arrays.

In *Proceedings of ICASSP*, pages 2646–2649, 1988.

[Wah93] Daniel E. Wahl.

A new method for array shape correction in towed linear arrays.

Digit. Signal Process., 3(1):46–53, March 1993.

[WF88] Anthony J. Weiss and Benjamin Friedlander.

Array shape calibration using sources in unknown locations — a maximum likelihood

approach.

In *Proceedings of ICASSP*, pages 2670–2673, 1988.

[WRM94] Marilynn P. Wylie, Sumit Roy, and Hagit Messer.

Joint doa estimation and phase calibration of linear equispaced arrays.

IEEE Trans. Sig. Proc., 42(12):3449–3459, dec 1994.

Appendix A In factorising $\mathbf{R} = \mathbf{A}\mathbf{R}_s\mathbf{A}^{\mathrm{H}} + \mathbf{J}$, all possible solutions for A must have the same rank and exist in the same subspace of $\mathbb{C}^M$.

Let the rank of $\mathbf{A}\mathbf{R}_s\mathbf{A}^{\mathrm{H}}$ be N, and $\nu_1, \nu_2, \ldots, \nu_N$ be the eigenvalues. Then the M eigenvalues of $\mathbf{R}$ are given by,

$$\lambda_m = \begin{cases} \nu_m + \sigma^2, & 1 \leq m \leq N \\ \sigma^2, & N < m \leq M \end{cases} \tag{A.1}$$

where σ^2 is the noise power. And so the number of eigenvalues not equal to the lowest value, σ^2, is the rank, N, of $\mathbf{A}\mathbf{R}_s\mathbf{A}^{\mathrm{H}}$. If $\mathbf{V} = [\mathbf{v}_1, \mathbf{v}_2, \ldots, \mathbf{v}_M]$, where $\mathbf{v}_m$ are the eigenvectors, and $\Lambda = \mathrm{diag}\,[\lambda_1, \ldots \lambda_M]$, then $\mathbf{R} = \mathbf{V}\Lambda\mathbf{V}^{\mathrm{H}}$, and the last $M - N$ eigenvectors, corresponding to the σ^2 eigenvalues, span what is known as the noise subspace. We have,

$$\begin{aligned} \mathbf{R}\mathbf{v}_m &= \sigma^2\mathbf{v}_m \\ &= \left(\mathbf{A}\mathbf{R}_s\mathbf{A}^{\mathrm{H}} + \sigma^2\mathbf{I}\right)\mathbf{v}_m \\ &= \mathbf{A}\mathbf{R}_s\mathbf{A}^{\mathrm{H}}\mathbf{v}_m + \sigma^2\mathbf{v}_m, \quad \forall\, N < m \leq M \end{aligned} \tag{A.2}$$

hence $\mathbf{A}\mathbf{R}_s\mathbf{A}^{\mathrm{H}}\mathbf{v}_m = \mathbf{0}$, and because $\mathbf{A}$ and $\mathbf{R}_s$ are full rank,

$$\begin{aligned} &\mathbf{A}^{\mathrm{H}}\mathbf{v}_m = \mathbf{0}, \text{ or} \\ &\mathbf{a}_n^{\mathrm{H}}\mathbf{v}_m = 0, \quad \forall\, n,\ N < m \leq M. \end{aligned} \tag{A.3}$$

This result tells us that the noise subspace of rank $M - N$ is orthogonal to the rank N subspace defined by the column vectors of $\mathbf{A}$. Thus, all solutions for $\mathbf{A}$, when factorising the array-covariance matrix, must have the same rank and span the same subspace.

Appendix B Simultaneous solution of sensor positions from the steering-vector matrix for three sensors and three signals.

The positions of the first, second and third sensors in a three-sensor, three-signal system can be determined by the simultaneous solution of the equations in (3.12), which are reproduced in (B.1) for clarity.

$$\begin{aligned} x_2^2\left(d_{31}-x_3\frac{d_{21}}{x_2}\right)^2 &= y_3^2(x_2^2-d_{21}^2),\\ x_2^2\left(d_{32}-x_3\frac{d_{22}}{x_2}\right)^2 &= y_3^2(x_2^2-d_{22}^2),\\ x_2^2\left(d_{33}-x_3\frac{d_{23}}{x_2}\right)^2 &= y_3^2(x_2^2-d_{23}^2). \end{aligned} \tag{B.1}$$

The first sensor is assumed to be at the origin and the second sensor is on the x-axis, which removes any translational or rotational ambiguities. The solutions for x_2, x_3 and y_3 are given as follows:

$$x_2 = 2\sqrt{\frac{-\left(d_{21}d_{31}\left(d_{23}^2-d_{22}^2\right)+d_{22}d_{32}\left(d_{21}^2-d_{23}^2\right)+d_{23}d_{33}\left(d_{22}-d_{21}^2\right)\right)\times}{\begin{array}{c}(d_{21}d_{32}-d_{22}d_{31})(d_{21}d_{33}-d_{23}d_{31})(d_{22}d_{33}-d_{23}d_{32})\\ \hline (d_{21}(d_{32}+d_{33})-d_{22}(d_{31}+d_{33})-d_{23}(d_{31}-d_{32}))\times\\ (d_{21}(d_{32}+d_{33})-d_{22}(d_{31}-d_{33})-d_{23}(d_{31}+d_{32}))\times\\ (d_{21}(d_{32}-d_{33})-d_{22}(d_{31}+d_{33})+d_{23}(d_{31}+d_{32}))\times\\ (d_{21}(d_{32}-d_{33})-d_{22}(d_{31}-d_{33})+d_{23}(d_{31}-d_{32}))\end{array}}} \tag{B.2}$$

$$x_3 = \frac{x_2}{2}\times\frac{d_{21}^2\left(d_{32}^2-d_{33}^2\right)+d_{22}^2\left(d_{33}^2-d_{31}^2\right)+d_{23}^2\left(d_{31}^2-d_{32}^2\right)}{d_{21}d_{31}\left(d_{23}^2-d_{22}^2\right)+d_{22}d_{32}\left(d_{21}^2-d_{23}^2\right)+d_{23}d_{33}\left(d_{22}^2-d_{21}^2\right)} \tag{B.3}$$

$$y_3 = \sqrt{\frac{(d_{21}d_{32}-d_{22}d_{31})(d_{21}d_{33}-d_{23}d_{31})(d_{22}d_{33}-d_{23}d_{32})}{d_{21}d_{31}(d_{23}2-d_{22}2)+d_{22}d_{32}(d_{21}2-d_{23}2)+d_{23}d_{33}(d_{22}2-d_{21}2)}} \tag{B.4}$$

For the solutions to x_2, x_3 and y_3 to be real the expressions within the square-root operators must be positive, which constrains the variables $\{d_{mn}\}_{m=2,n=1}^{m=3,n=3}$. These constraints are

$$\frac{(d_{21}d_{32}-d_{22}d_{31})(d_{21}d_{33}-d_{23}d_{31})(d_{22}d_{33}-d_{23}d_{32})}{(d_{21}d_{31}(d_{23}2-d_{22}2)+d_{22}d_{32}(d_{21}2-d_{23}2)+d_{23}d_{33}(d_{22}2-d_{21}2))} \geq 0 \tag{B.5}$$

and

$$\begin{array}{c}(d_{21}(d_{32}+d_{33})-d_{22}(d_{31}+d_{33})-d_{23}(d_{31}-d_{32}))\times\\ (d_{21}(d_{32}+d_{33})-d_{22}(d_{31}-d_{33})-d_{23}(d_{31}+d_{32}))\times\\ (d_{21}(d_{32}-d_{33})-d_{22}(d_{31}+d_{33})+d_{23}(d_{31}+d_{32}))\times\\ (d_{21}(d_{32}-d_{33})-d_{22}(d_{31}-d_{33})+d_{23}(d_{31}-d_{32}))<0.\end{array} \tag{B.6}$$

Appendix C The derivatives of sharpness function S_2 with respect to array-shape parameters $\{\alpha_\lambda\}$ and $\{\beta_\lambda\}$.

$$\frac{\delta S_2}{\delta \hat{\alpha}_\lambda} = 2\int_0^\pi P_c(\phi)\left[\frac{\delta P_c(\phi)}{\delta \hat{\chi}}\frac{\delta \hat{\chi}}{\delta \hat{\alpha}_\lambda}\right]\sin\phi\, d\phi,$$
$$\frac{\delta S_2}{\delta \hat{\beta}_\lambda} = 2\int_0^\pi P_c(\phi)\left[\frac{\delta P_c(\phi)}{\delta \hat{\chi}}\frac{\delta \hat{\chi}}{\delta \hat{\beta}_\lambda}\right]\sin\phi\, d\phi, \tag{C.1}$$

where $\frac{\delta P_c}{\delta \hat{\chi}_m}$ is given by

$$\frac{\delta P_c}{\delta \hat{\chi}_m} = j\pi\delta_\phi\left[w^H R^{\mathrm{col}\,j} w_m - w_m^* R^{\mathrm{row}\,j} w\right], \tag{C.2}$$

and

$$\frac{\delta \hat{\chi}_m}{\delta \hat{\alpha}_\lambda} = \left[\frac{\delta \hat{x}_m}{\delta \hat{\alpha}_\lambda}, \frac{\delta \hat{y}_m}{\delta \hat{\alpha}_\lambda}\right],$$
$$\frac{\delta \hat{\chi}_m}{\delta \hat{\beta}_\lambda} = \left[\frac{\delta \hat{x}_m}{\delta \hat{\beta}_\lambda}, \frac{\delta \hat{y}_m}{\delta \hat{\beta}_\lambda}\right], \tag{C.3}$$

where

$$\frac{\delta \hat{y}_m}{\delta \hat{\alpha}_\lambda} = \cos(\lambda \hat{x}_m) - \lambda\hat{\alpha}_\lambda \sin(\lambda \hat{x}_m)\frac{\delta \hat{x}_m}{\delta \hat{\alpha}_\lambda},$$
$$\frac{\delta \hat{y}_m}{\delta \hat{\beta}_\lambda} = \sin(\lambda \hat{x}_m) - \lambda\hat{\beta}_\lambda \cos(\lambda \hat{x}_m)\frac{\delta \hat{x}_m}{\delta \hat{\beta}_\lambda}. \tag{C.4}$$

$\hat{x}_m$ can be calculated using the distance along a curve:

$$(m-1)\rho = \int_0^{\hat{x}_m} \sqrt{1 + \left[f'\left(\hat{\alpha}_\lambda, \hat{\beta}_\lambda, t\right)\right]^2}\, dt, \tag{C.5}$$

where $f'(\alpha_\lambda, \beta_\lambda, t) = \frac{\delta}{\delta t} f(\alpha_\lambda, \beta_\lambda, t)$ and $f(\alpha_\lambda, \beta_\lambda, t)$ is defined in (6.9), and

$$\frac{\delta \hat{x}_m}{\delta \hat{\alpha}_\lambda} = \frac{-\lambda}{\sqrt{1 + [f'(\alpha_\lambda, \beta_\lambda, t)]^2}} \int_0^{\hat{x}_m} \frac{f'(\alpha_\lambda, \beta_\lambda, t)\cos(\lambda t)}{\sqrt{1 + [f'(\alpha_\lambda, \beta_\lambda, t)]^2}}\, dt,$$
$$\frac{\delta \hat{x}_m}{\delta \hat{\beta}_\lambda} = \frac{\lambda}{\sqrt{1 + [f'(\alpha_\lambda, \beta_\lambda, t)]^2}} \int_0^{\hat{x}_m} \frac{f'(\alpha_\lambda, \beta_\lambda, t)\sin(\lambda t)}{\sqrt{1 + [f'(\alpha_\lambda, \beta_\lambda, t)]^2}}\, dt. \tag{C.6}$$

$R^{\mathrm{col}\,j}$ and $R^{\mathrm{row}\,j}$ are the j^{th} column and the j^{th} row of R, respectively.

Errata for Towed-Array Calibration

January 2nd, 1997

On page 10 substitute the following for equation 2.4

$$X(f) = X_R(f) + jX_I(f)$$

and substitute the following for equation 2.5

$$X_I(f) = \begin{cases} -jX_R(f) & f \geq 0 \\ jX_R(f) & f < 0 \end{cases}$$

On page 24, theorem 2, substitute the words "and no linear" for "and a linear" and substitute the word "equals" for "does not give".

On page 26, last paragraph, substitute the word "coordinates" for "directions".

On page 35, Section 3.2.3, insert the sentence "Throughout this section I assume that the signals are perfectly correlated." between the second and third sentences of the first paragraph.

On page 50 insert the words "and SNR is 0dB" between "Hz" and the period in the caption of Table 2 and between "90°" and the period in the caption of Table 3.

On page 65, second-last paragraph, insert the words "and the MSE will increase monotonically (Figure 27(d))" between "estimate a straight array shape" and the period.

On page 66 insert the following sentences at the end of the first paragraph. "In Figures 28(c) and 28(d) the SNR is so low that the signal gives little information about the array shape. The MSE asymptotically approaches a limit defined by the SNR, σ_q^2 and the damping factor."

On page 81, equation 5.6, substitute "$\sigma_2^2 c_1 \mathbf{a}_2 \mathbf{a}_2^{\mathrm{H}} \mathbf{a}_1$" for the first term in the second line.